Operando Raman Spectroscopy of Transition Metal Oxide Catalysts in Regard to the Oxygen Evolution Reaction

Operando Raman-Spektroskopie von Übergangsmetalloxid-Katalysatoren für die Sauerstoffentwicklungsreaktion

Master-Thesis
Vorgelegt von **Hannes Radinger**
Matrikelnummer: **2748467**

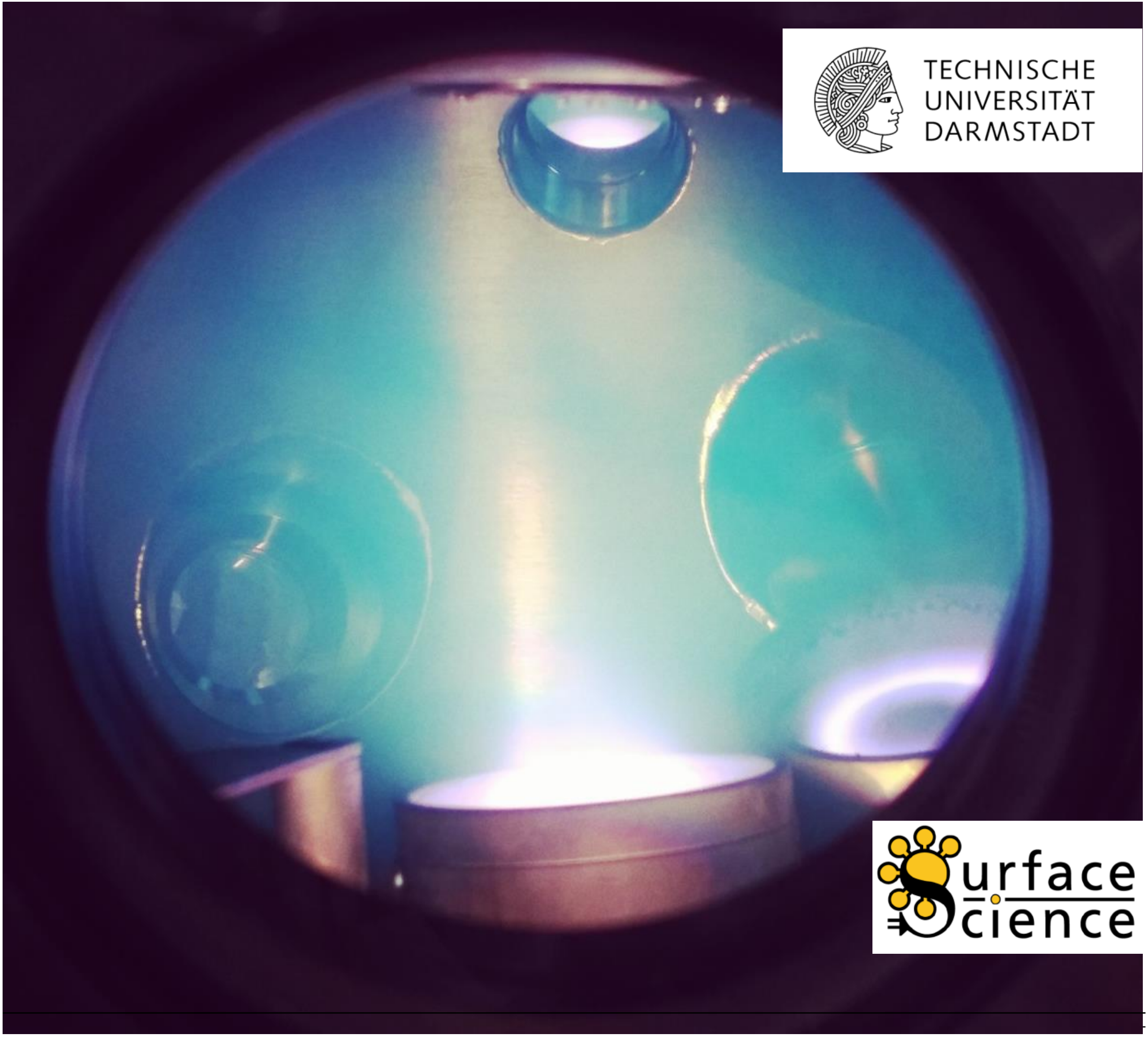

TECHNISCHE
UNIVERSITÄT
DARMSTADT

Surface
Science

Operando Raman Spectroscopy of Transition Metal Oxide Catalysts in Regard to the Oxygen Evolution Reaction

Operando Raman-Spektroskopie von Übergangsmetalloxid-Katalysatoren für die Sauerstoffentwicklungsreaktion

Vorgelegte Master-Thesis von Hannes Radinger, geboren in Friedberg (BY)

1. Gutachten: Prof. Dr. Wolfram Jaegermann/PD Dr. Bernhard Kaiser

2. Gutachten: Prof. Dr. Robert Stark

Erklärung zur Abschlussarbeit gemäß § 22 Abs. 7 und § 23 Abs. 7 APB TU Darmstadt

Hiermit versichere ich, Hannes Radinger, die vorliegende Master-Thesis gemäß § 22 Abs. 7 APB der TU Darmstadt ohne Hilfe Dritter und nur mit den angegebenen Quellen und Hilfsmitteln angefertigt zu haben. Alle Stellen, die Quellen entnommen wurden, sind als solche kenntlich gemacht worden. Diese Arbeit hat in gleicher oder ähnlicher Form noch keiner Prüfungsbehörde vorgelegen.

Mir ist bekannt, dass im Falle eines Plagiats (§38 Abs.2 APB) ein Täuschungsversuch vorliegt, der dazu führt, dass die Arbeit mit 5,0 bewertet und damit ein Prüfungsversuch verbraucht wird. Abschlussarbeiten dürfen nur einmal wiederholt werden.

Bei der abgegebenen Thesis stimmen die schriftliche und die zur Archivierung eingereichte elektronische Fassung gemäß § 23 Abs. 7 APB überein.

Datum / Date: Unterschrift/Signature:

Jede Reise hat ein Ende, jeder Hafen hat ’ne Bar

— Panik Panzer

Danke!

Das Zustandekommen dieser Arbeit ist keinesfalls nur mein eigener Verdienst und an dieser Stelle muss und möchte ich alle Personen würdigen, die innerhalb der letzten sechs Monate hilfreich dazu beigetragen haben.

Zuallererst gilt mein Dank Prof. Dr. Wolfram Jaegermann und PD Dr. Bernhard Kaiser, da sie mir die Möglichkeit geboten haben, an so einem schillernden Thema wie der dynamischen Charakterisierung von Katalysatoren zu arbeiten und mich dabei kreativ und frei entfalten zu können. Wichtige Hilfestellungen und Richtungsweisungen wurden mir dafür im wissenschaftlichen Austausch geboten. Außerdem danke ich Prof. Dr. Robert Stark für die Übernahme der Zweitkorrektur und wertvolle Hinweise zur Raman-Spektroskopie, sowie die Bereitstellung seiner Infrastruktur.

Weiterhin danke ich Paula Connor für die Einarbeitung am DAISY-Fun, hilfreiche Diskussionen auf dem Weg und die Korrektur am Ende meiner Arbeit. Danke an Sven Tengeler, der mir die Bearbeitung des Themas vorgeschlagen und mich dabei unterstützt hat.

Außerdem vielen Dank an Alena Bell und Nan Chai für die Einführung in die Raman-Spektroskopie, an Lukas Stühn für die Bedienung des Rasterkraftmikroskops und an Andreas Hubmann für die Aufnahme der UV-vis-Spektren.

Dankeschön, für die außergewöhnlich herzliche und fachlich kompetente Atmosphäre unter den Wasserspaltern, von denen ich freundlich empfangen wurde und immer jemanden hatte, der sich mit mir auf Diskussionen einließ und mit Rat und Tat zur Seite stand.

Zu guter Letzt gilt mein wichtigster Dank meiner Familie, meinen Freunden und ganz besonders meinen Felsen in der Brandung, meiner zauberhaften Freundin Aliena und David Bowie.

Abstract

Transition metal oxides (NiO_x, MnO_x) have been synthesized by reactive magnetron sputtering and analysed regarding their chemical composition with XPS to develop active catalysts for the oxygen evolution reaction in alkaline media. NiO_x was investigated towards its temperature dependent deficient structure and the enhancement of the catalytic activity through these defects. The catalytic activity was evaluated with the help of *operando* Raman spectroscopy to monitor the active surface intermediates of NiO_x and investigate a temperature dependent Ni^{III}/Ni^{IV} redox transition. The defect structure was concluded to greatly improve catalytic activity, capacitive charge storage, and redox processes.

MnO_x was deposited in three different oxidation states (Mn^{II}, Mn^{III}, and Mn^{IV}) as concluded with XPS and investigated towards its suitability as OER catalyst. With Raman spectroscopy, all MnO_x revealed δ-MnO_2 structure when in contact with the alkaline electrolyte. Their catalytic activity was detected to differ based on their degree of charging with an applied potential, *i.e.* the coexistence of Mn^{III} and Mn^{IV} species, and an increased distance between layers of MnO_6 octahedra. With a combination of reduction and activation processes, the activity of Mn^{II} was altered greatly, to receive a by more than 100 mV reduced overpotential at $5\,mA\,cm^{-2}$, and a low Tafel slope of $44\,mV\,dec^{-1}$.

Contents

1 Introduction

There is plenty motivation to work in the field of water splitting, catalysis, in situ characterization, and thin film technology. This short introduction is meant to provide an overview of why a master thesis is a good possibility to gain insight into a fruitful combination of all these research categories.

Energy from renewable energy carriers such as wind, water, and solar power plays an important role regarding climate change. Global energy utilization mostly depends on fossil fuels, but energy supplies are expected to run out over the next 150 years [1]. Further, energy consumption is expected to grow significantly, catering growing interest in investigation of renewable energy technologies [2]. One of the most important tasks nowadays is the development of efficient storage systems, *e.g.* direct storage devices such as lithium ion batteries or conversion into storable energy carriers like hydrogen (H_2). Some of the energy produced by renewable sources can not be consumed right away, so to reduce environmental damage as well as costs for fossil fuels, storage of this particular free energy is desirable. For instance, the unused wind power in China 2016 was calculated to 497×10^5 MWh [3].

Hydrogen is the most abundant element in the universe and is usually bound in water (H_2O) molecules. It is known to have 2 to 3 times the specific energy density of gasoline and is carbon free as a plus [4, 5]. Additionally, H_2 production from aqueous solutions *via* electrolysis is by-product free, *i.e.* no separation systems (besides separation of H_2 and O_2) for contaminated gas have to be supplied compared to the combustion of fossil fuels.

The development of active, cheap, and durable catalyst materials is seen as a key challenge of electrochemistry application research. Best known performing catalysts contain noble metals such as platinum (Pt) as most active catalyst for the hydrogen evolution reaction (HER) or ruthenium(IV) oxide (RuO_2) and iridium(IV) oxide (IrO_2) for the oxygen evolution reaction (OER). RuO_2 and IrO_2 show the lowest known overpotential towards the OER but hold poor chemical stability in alkaline media [6]. Over the last decades, a lot of research has been done to investigate transition metal oxides (TMO) to replace noble metals in water splitting catalysis. These non-noble transition metals posses relevant advantages due to their earth-abundance, low cost, and durability [7].

Catalysis

A catalyst is a substance that increases the rate of a chemical reaction without undergoing a chemical change itself during the process. Most reactions in the human body, the atmosphere, and the sea are catalysed, resulting in a variety of research regarding new, effective and cost efficient catalysts in chemical industries [8]. This work focuses on heterogeneous catalysis, where the catalyst possess a phase different from the reaction molecule, resulting in complex kinetics on solid-liquid interfaces. The surface atoms on catalysts are able to adsorb reaction molecules due to an unsatisfying amount of bonding partners or dangling bonds.

Solid catalysts often consist of metals or metal oxides, catalysing chemical reactions on their surface which is why there are many methods of enhancing the accesible surface of such catalysts, for instance with nanoparticles (NP) or nanocubes for CO_2 reduction [9], or Ni foams for H_2O electrolysis [10]. Both techniques can be combined, integrating $MoNi_4$ NPs in Ni foam for efficient HER [11] or CoO_x NPs in carbon foam as OER catalysts [12].

Studying heterogeneous catalysts *in situ*

There is a rising interest in the work of developing analytical tools to investigate the chemical processes taking place on an active catalyst under working conditions by the use of *in situ* (latin: on site) characterization techniques [13]. Alternatively, the terms *in vivo* (latin: within the living), *on line* or *operando* (latin: working) are used and widely spread in literature to describe the same discipline [13, 14]. According to a literature review in ref [15], *in situ* is used to describe the recording of spectra at the same location where the sample is treated, *e.g.* a spectroscopic cell, while *operando* means simultaneous use of an additional analysis technique to determine a chemical change under working conditions. For an *operando* cell, the possibility of obtaining kinetically relevant data, is a key requirement. Since in this work the kinetic processes on the surface of OER catalysts under working conditions are studied by Raman spectroscopy during the application of electrochemistry measurement techniques, the term *operando* is used further.

The difficulty is to apply *in situ* techniques that address not only the bulk material, but allow monitoring of surface changes, intermediates, or adsorption processes. Also, conventional spectroscopy is applicable to catalysts either freshly prepared or used, mostly under room temperature [16]. Nowadays, *in situ* spectroscopy of catalysts is used by a variety of spectroscopic techniques such as infrared (IR), Raman, X-ray absorption (XAS), nuclear magnetic resonance (NMR), UV-vis, and Mössbauer spectroscopy, to name a few [16].

Raman spectroscopy in particular is convenient for *operando* spectroscopy, since it uses visible light, allowing observation of catalysts due to irradiation through transparent cells. It is also applicable at higher temperatures, enabling monitoring of thermal decomposition or experiments at elevated pressures [17, 15]. Especially Raman spectroscopy gives strong signals for typical catalytic active sites, such as molecular $M{=}O$, $M{-}O{-}M$, $M{-}O$, and $M{-}O{-}O$ vibrations. IR spectroscopy for instance, which signal is strongly adsorbed by aqueous phases, gives rise to strong signals of surface chemistry probes, such as CO or CH_3OH, and M–OH surface hydroxyls [18].

Wachs and Roberts [18] reviewed catalysis literature from *ca.* 1970 to 2010, reporting that Raman catalyst studies have seriously started to rise after 1995 due to the employment of *in situ* techniques for active site determination. In fact, *ca.* 25 % of available Raman literature nowadays focuses on *in situ* spectroscopy, accounting to the dynamic Raman signal response regarding environmental factors such as concentration, temperature, or pressure.

This work

In this thesis, NiO_x and MnO_x are investigated towards their suitability as catalyst electrodes regarding the oxygen evolution reaction in alkaline media. A special focus will rely on structure-activity correlations to examine the influence of defects in NiO_x and its substrate dependence. Different manganese oxidation states are discussed regarding their influence on the catalytic activity.

Thin films of the materials are sputtered mainly on gold, analysed with XPS, investigated in electrochemistry and monitored under working condition with Raman spectroscopy. Since this is the first thesis in this group to engage in this field, a minor part will deal with the general process of surface enhancement and *in situ* spectroscopy of metal oxides.

2 Theoretical Background

This chapter provides an overview of the theoretical background needed to understand the experimental part. The basics of electrochemistry for water splitting are discussed and the overall kinetic processes on the surface of electrodes, especially for the oxygen evolution reaction, including the electrochemical double layer in solid/electrolyte interfaces and the Butler-Volmer equation are explained. The effective method of sputter deposition for sample synthesis is explicated, followed by the main analysis methods, Photoelectron and Raman spectroscopy.

2.1 Water Splitting

Electrochemistry (EC) is a discipline of physical chemistry, studying the relations between electrical energy and chemical processes with a focus on using electrons (e^-) to induce a chemical change and vice versa, specified by two different examples for an electrochemical reaction:

(a) a chemical reaction driven by externally supplied electric current, as in the water splitting reaction, known as electrolysis;

(b) production of an electric current through an exothermal chemical reaction, as in the discharging process of a battery.

An electrochemical reaction involves e^- transfer from one molecule or ion to another, changing its oxidation state. This happens for condition (a) as well as for condition (b). Based on the change in oxidation state, a molecule/ion is either oxidized in an anodic or reduced in a cathodic process, forming a reduction-oxidation (redox) couple [19]:

$$\mathrm{Ox} + \mathrm{n}e^- \longleftrightarrow \mathrm{Red} \tag{2.1}$$

The possible half cell reactions towards successful electrolysis are oxygen evolution reaction (OER) and hydrogen evolution reaction (HER). Their corresponding counter reactions, as they occur in a fuel cell, are called oxygen reduction reaction (ORR) and hydrogen oxidation reaction (HOR). The OER can be seen as the bottleneck of water splitting due to its slow kinetics and the high overpotential (η) that has to be supplied to drive the reaction to produce later energetically useful H_2 [20].

Since the half cell potential E of an electrode can not be measured directly, potentials for different redox couples are standardized versus the H^+/H_2 potential in a standard hydrogen electrode (SHE), which is $E^0 = 0\,\mathrm{V}$ by definition. The standard potentials E^0 at 1 bar and 25 °C are tabulated in the galvanic series. Redox reactions are highly pH dependent and differ in reaction mechanisms as well. In neutral and acidic conditions two water molecules (H_2O) are oxidized into four protons (H^+) and one oxygen (O_2) molecule, defining an anodic half cell potential of $E^0_a = 1.23\,\mathrm{V}$. In alkaline environment, an anodic half cell potential of $E^0_a = 0.40\,\mathrm{V}$ ($E^0_c = -0.83\,\mathrm{V}$) is needed to oxidize four hydroxyl groups (OH^-) and transform them in two H_2O and one oxygen molecules.

Acidic solution:

$$2\,H_2O(l) \longleftrightarrow 4\,H^+ + O_2(g) + 4\,e^- \tag{2.2}$$

Alkaline solution:

$$4\,OH^- \longleftrightarrow 2\,H_2O(l) + O_2(g) + 4\,e^- \tag{2.3}$$

The theoretical value of both half cell reactions is $E = 1.23\,\mathrm{V}$, the minimum bias potential for water splitting to take place, independent of the pH value. Both half cell potentials shift based on the pH value, keeping 1.23 V constant. The pH dependence for each half cell potential is calculated using the Nernst equation.

$$E = E^0 + \frac{RT}{nF} ln(\frac{a_{Ox}}{a_{Red}}) \tag{2.4}$$

with the ideal gas constant R (8.31 J mol^{-1} K^{-1}), temperature T, the number of e$^-$ transferred n, the Faraday constant F (96485.33 C mol^{-1}) and the activity ratio of the redox couple $a_{\mathrm{Ox}}/a_{\mathrm{Red}}$. Using standard condition values of $T = 298.15\,\mathrm{K}$ at $p = 1\,\mathrm{bar}$, the Nernst equation is simplified to

$$E \simeq E^0 + \frac{0.059\,\mathrm{V}}{n}\mathrm{pH} \tag{2.5}$$

Consequently, to avoid pH dependence and further correction according to the Nernst equation for measurements, a reversible hydrogen electrode (RHE) is used. While stability at all pH values is desired, research is often done in alkaline environment due to the elevated stability of metal oxides in higher pH region.

Kinetics of the OER

The production of molecular O_2 requires the transport of four e$^-$, occurring in a multi step reaction with single e$^-$ transfer. Each step results in an accumulation of energy and consequently in complex kinetics for the OER, creating need for catalysts with high activity as well as sufficient stability. In alkaline solutions, the catalytically active site adsorbs hydroxide anions (OH$^-$) initially. The adsorbed hydroxide (OH_{ads}) reacts with a free OH$^-$ to build an adsorbed oxide (O_{ads}) as an intermediate while recombining a new H_2O molecule [21]:

$$OH^- \longrightarrow OH_{ads} + e^- \tag{2.6}$$

$$OH_{ads} + OH^- \longrightarrow O_{ads} + H_2O + e^- \tag{2.7}$$

The O_{ads} again reacts with a free OH$^-$ to build OOH_{ads} as an intermediate, which in a final step reacts with OH$^-$ to build molecular O_2 and a H_2O molecule:

$$O_{ads} + OH^- \longrightarrow OOH_{ads} + e^- \tag{2.8}$$

$$OOH_{ads} + OH^- \longrightarrow O_2 + H_2O + e^- \tag{2.9}$$

Figure 2.1 displays the energy diagram of an ideal OER catalyst, if the previously discussed mechanism is occurring. Per definition, the ideal catalyst needs four charge transfer steps with identical reaction energies ΔG of 1.23 eV each, resulting in 4.92 eV in total [22]. One major focus in catalysis research is tuning the binding energy of the intermediates on the surface to overcome the energy difference of the OH_{ads} and the OOH_{ads} intermediate, 2.46 eV on an ideal catalyst. However, the binding of these intermediates was estimated by a constant of *ca.* 3.2 eV for metals and oxide surfaces, implying a universal scaling ratio between OH_{ads} and OOH_{ads} [23].

These kinetic processes discussed in above equations are the reason for the OER not to take place at the theoretical potential of 1.23 V. The various hindrance aspects are summed up as the so called overpotential η which is defined as the difference between the experimentally measured potential E_M and the standard equilibrium potential E_0.

$$\eta = \eta_{\mathrm{CT}} + \eta_{\mathrm{diff}} + \eta_{\mathrm{R}} + IR_{\mathrm{el}} = E_{\mathrm{M}} - E_0 \tag{2.10}$$

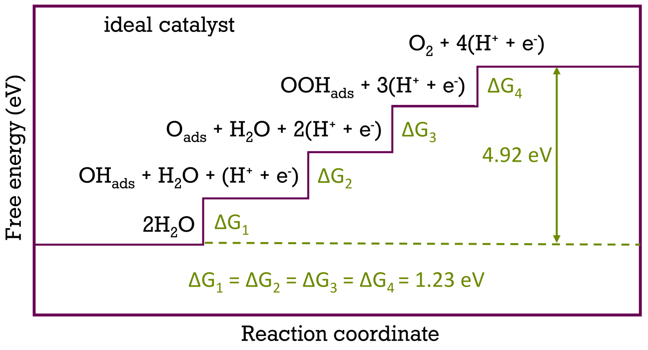

Figure 2.1: Free energy diagram for the oxygen evolution reaction on the perfect catalyst at zero potential ($E = 0$). In four charge transfer steps with identical free energies, it takes 4.92 eV towards O_2 evolution. Reproduced from ref [22].

The charge transfer (CT) overpotential η_{CT} exists due to charge passing through the phase boundary, the diffusion overpotential η_{diff} describes the hindrance of reactants in the electrolyte, while the reaction overpotential η_{R} is a consequence of subprocesses such as ad- and desorption or side reactions. In the electrolyte an ohmic voltage drop IR_{el} can be measured and subtracted after the experiment to approach the real η. Experimental conditions should be adjusted to minimize the influence on η_{diff} and the reaction components, whereas the CT depends on the catalytic properties of the used electrode.

The scaling relationship between OH_{ads} and OOH_{ads} is one of the major components of the reaction overpotential [22]. Further, it has been reported that either the oxidation process of OH_{ads} to O_{ads} or the water dissociation process from O_{ads} towards OOH_{ads} is rate-determining [24].

Electrical double layer

A standard description of electrochemical CT processes is given with the *Helmholtz* layer, describing a plate capacitor like rigid double layer at the solid/electrolyte interface. This model was further elaborated as the Gouy-Chapman model, considering the thermal motion of ions, expressed as a diffuse double layer with an exponential potential profile.

A combination of both models is given by the Stern model, assuming a superposition of the rigid and the diffusive double layer. This model is illustrated in figure 2.2, indicating the different planes and layers as well as the development of the potential, starting from a solid metal electrode (Φ_{M}), dropping at the electrode/electrolyte interface, and reaching a steady potential at a distance beyond the diffuse double layer regime in the electrolyte (Φ_{el}). Applying a voltage will charge the anode positively, leading to a dipole orientation of the molecules in the liquid electrolyte towards the electrode's surface. For a H_2O molecule, the negatively charged oxygen adsorbs to the surface—creating the rigid inner Helmholtz plane (IHP)—while the positively charged hydrogen atoms attract nearby OH^-, giving rise to the diffusive outer Helmholtz plane (OHP). To adsorb to the electrode surface, the OH^- have to overcome a potential difference which is equal to the stated η_{CT}.

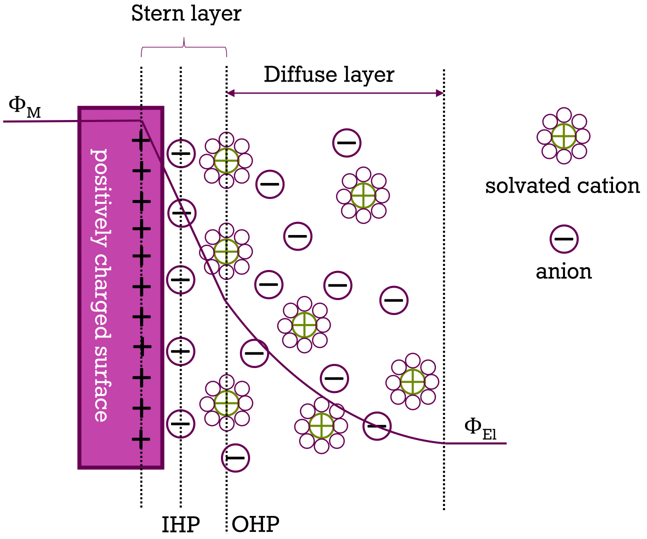

Figure 2.2: Electrical double layer model by Stern for a solid electrode immersed in a liquid electrolyte, showing the inner Helmholtz plane (IHP) and outer Helmholtz plane (OHP). The IHP refers to the distance of specifically adsorbed ions, and OHP refers to that of non-specifically adsorbed ions. The potential gradient is indicated, starting at the potential of the metal electrode Φ_{M}, dropping linearly in the rigid double layer regime and reaching a steady potential of the electrolyte Φ_{El} beyond the diffuse double layer. Reproduced from ref [25].

For the OER, the η in literature is often defined as potential difference between E at a current density $j = 10\,\mathrm{mA\,cm^{-2}}$ and 1.23 V. An excellent catalyst for the OER shows overpotential values in a range of 300 to 400 mV. [19] Metal oxide catalysts like RuO_2 and IrO_2 are known for their low η below 330 mV, but due to their high prizes research in non-noble transition metals is done.

Kinetics of an electrode reaction

Since one of the four e⁻ transfer steps of the OER is rate determining—assuming the current density j of an electrode surface is a function of η—a kinetically description of j can be given by the Butler-Volmer equation [26]:

$$j = j_0[exp(\frac{\alpha nF\eta}{RT}) - exp(\frac{(\alpha-1)nF\eta}{RT})] \qquad (2.11)$$

The theory of the Butler-Volmer equation is valid for an ideal single e⁻ transfer process, considering cathodic and anodic reaction at the same electrode. The exchange current density j_0 is the current density at which anodic and cathodic currents are equalized. The CT coefficient α is a dimensionless factor defined as the fraction of the electrostatic potential energy affecting the reduction rate in an electrode reaction. Regarding the anodic reaction it is calculated with [27]:

$$\alpha_a = \frac{2.3RT}{nF}(\frac{d\log j_a}{\mathrm{d}E}). \qquad (2.12)$$

In this equation, $\frac{d\log j_a}{\mathrm{d}E}$ is the inverse of the so called Tafel slope (in $\mathrm{dec\,V^{-1}}$) that is determined from cyclic or linear sweep voltammetry data at low scan rates. The number of transferred e⁻ (n) changes based on the OER reaction mechanism [28]. For an alkaline reaction path at $\eta > 300$ mV, a factor of $\frac{RT}{F}$ is suggested [29]. Plotting the logarithmic current density $\log(j)$ *vs.* the overpotential η, the Tafel slope is determined in the linear region of the curve (see figure 2.3). Further, through the intercept with the $\log(j)$ axis, the j_0 from the Butler-Volmer equation is determined.

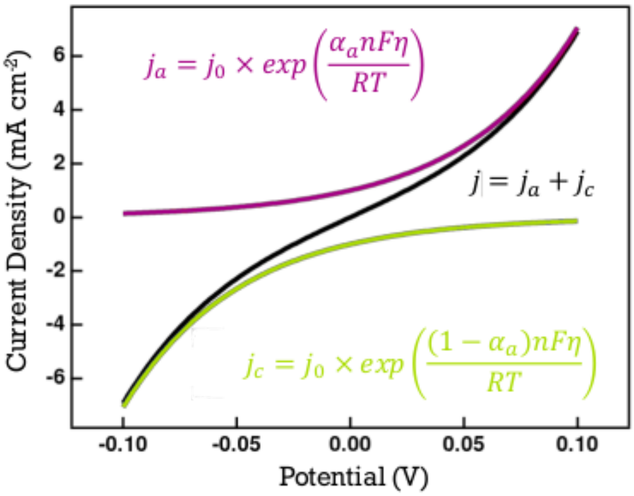

Figure 2.3: The cathodic and anodic branch as well as the sum of both current densities based on Butler-Volmer. This depiction is valid for $j_0 = 1\,\mathrm{mA\,cm^{-2}}$ and $\alpha = 0.5$.

2.2 Sputter Deposition

Sputter deposition is a physical vapor deposition (PVD) method to generate thin films on a substrate by sputtering—a process, where noble gas atoms, often Argon, are ionized in a plasma and accelerated towards a target by an electric field. The positive gas ions (Ar^+) bombard the target to eject its atoms by momentum transfer; those atoms are then deposited on the substrates surface. In addition, other particles such as secondary e⁻, desorbed gas, negative ions, and radiation (X-rays, photons) are emitted from the target.

Sputtered atoms show a wide range of energies up to tens of eV. Not only the ejected particles, but also the ionized gas species are able to interact with the sample, leading to an electrical charged substrate and removal of deposited layers. To prevent this effect and achieve higher deposition rates, a magnetic field above the target keeps Ar^+ from reaching the sample, giving rise to magnetron sputtering [30].

The ionized, conducting state of the otherwise insulating gas atoms (plasma) is achieved by the Townsend discharge. An electric field accelerates free e⁻ which collide with a neutral gas atom A, converting it into a positively charged ion A^+ under release of another e⁻.

$$e^- + A \longrightarrow 2\,e^- + A^+ \tag{2.13}$$

The liberated e⁻ is accelerated as well and contributes to the e⁻ avalanche. The breakdown voltage V_B depends highly on the system pressure p inside the sputter chamber and the distance d between the electrodes. To reach the electric breakdown, a minimum d is required to gain sufficient energy in the electric field and to maintain ionization. Also, d needs to be wide enough to prevent escape of charged particles through sideways diffusion. The system pressure is inversely proportional to the mean free path λ which must be high enough for a particle to reach the ionization potential. In general, the breakdown voltage can be described through

$$V_B = \frac{Apd}{ln(pd)+B} \tag{2.14}$$

with A and B being constants. At low values of pd there are not enough collisions, for high values of pd too many collisions keep e⁻ from gaining sufficient energy for ionization. The discharge is self-sustained in between several 100 V to 1 kV, meaning as a current flows the gas keeps a population of ions and free e⁻ to continue current flow.

Other gases than Ar can be used additionally while sputtering. The additional gas works as an educt for the deposited species *via* interaction with the ejected target material. Typical gases for this reactive sputter process are N_2 and O_2 to deposit well defined nitrides and oxides. These reactions take place on the target, in the gas phase, and on the substrate [31]. Adding a reactive gas component changes the composition, the deposition rate and the necessary electric field to keep up the plasma.

2.3 X-Ray Photoelectron Spectroscopy

X-Ray Photoelectron Spectroscopy (XPS) is a well-established, surface sensitive method of Photoelectron Spectroscopy (PES) to measure the chemical composition of thin-layered solid materials. A surface of a sample is irradiated with photons ($h\nu$), directly interacting with the atoms' core level e⁻.

Basic Principle

The basic principle is the photoelectric effect, where light of sufficient energy causes the emission of free electrons from a sample. In XPS, a monochromatic X-ray source emits light with defined energy

$$E_\lambda = h\nu = \frac{hc}{\lambda} \tag{2.15}$$

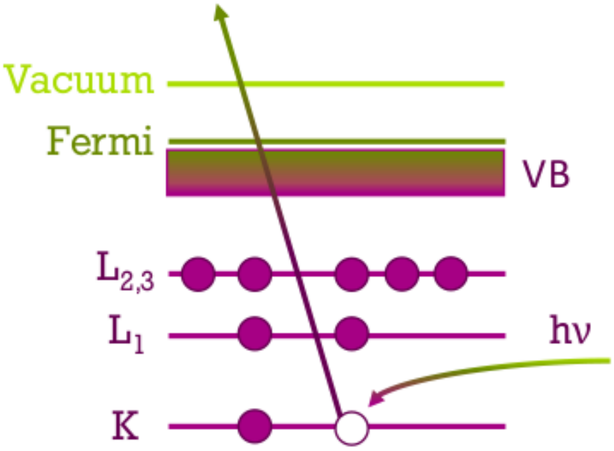

Figure 2.4: Photoemission process for XPS surface analysis. The filled circles represent electrons, the horizontal lines the corresponding energy levels. The empty circle is an electron ejected by incident light with the energy $h\nu$.

XPS delivers information of only the upper atomic layers: incident photons may deeply penetrate the bulk, but due to inelastic scattering of e⁻ inside the material and limited λ_i, mostly upper layer e⁻ are ejected from the sample. The escape depth/inelastic mean free path (IMFP) of an elements core e⁻ is based on its kinetic energy E_{kin} and is highest between 50 to 100 eV, as given by the *universal curve* in figure 2.5. For an e$^-$ of an intensity I_0 emitted at a depth d below the surface, the intensity is attenuated according to the Lambert-Beer law. As a result, the intensity of the same e$^-$ reaching the surface I_s is described as

$$I_s = I_0 \exp(\frac{-d}{\lambda_i}) \qquad (2.16)$$

with λ_i being the IMFP. Measuring E_{kin} of the ejected e$^-$, a spectrum of binding energy E_{BE} is obtained. The relation of these energies is given by

$$E_{\text{BE}} = h\nu - E_{\text{kin}} - \Phi \qquad (2.17)$$

with Φ being the work function of the surface, where E_{kin} is measured, in this case the spectrometer's analyser. Since the sample's Fermi level aligns with the analysers' in contact (the default setting for XPS), the known analysers' work function Φ_S is used for calculation.

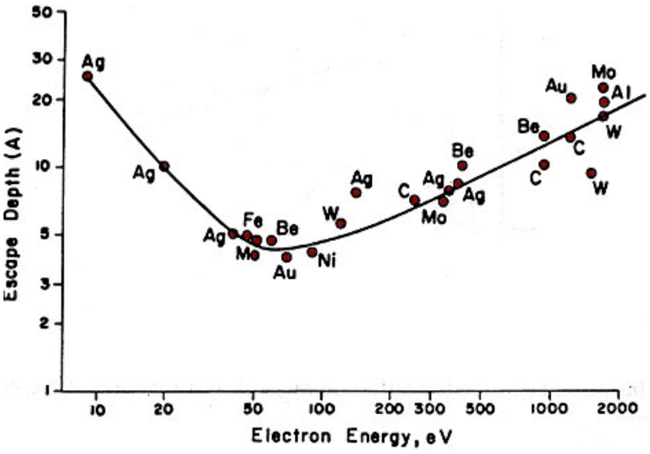

Figure 2.5: Escape depth/inelastic mean free path (IMFP) of some elements core level electrons in dependency of the electrons kinetic energy. The black line represents the values calculated in theory while the black dots are measured values for the elements [32].

E_{BE} is different for each atom, so XPS can be used to identify almost all elements. Chemical shifts of an element can be correlated to its oxidation state, since a change in E_{BE} is observed when the oxidation state changes. E_{BE} of an e$^-$ depends on several factors, of which some important are the element as well as the orbital from which the e$^-$ is ejected from and the chemical environment of the atom. Since E_{BE} depends on the chemical environment of the atom, existing ligands can be determined.

The basic pressure in an electron spectrometer must be adjusted to avoid scattering on gas molecules in the electrons path from sample to analyzer, and to minimize surface contamination to prevent distortion of the spectra [33]. The monolayer formation time of adsorbed atmospheric atoms depends on their sticking coefficient, describing the specific reactivity of gas and surface. To guarantee accurate and reliable results, the pressure in most equipments is $p \leq 5 \times 10^{-10}$ mbar [33, 34].

All elements with an azimuthal quantum number l higher than 0 show a split peak in a XP spectra because of the e$^-$ and orbital angular momentum interaction. The e$^-$ spin angular momentum (described by the spin quantum number s) is either 1/2 or −1/2 while l is defined for the corresponding main quantum number n, taking integer values from 0 to $n-1$. The numerical value of l is mostly replaced by corresponding letters, *e.g.* s ($l = 0$), p ($l = 1$), d ($l = 2$), f ($l = 3$). The movement of the e$^-$ around its associated nucleus is described by the total angular momentum quantum number j. Peaks in XP spectra are characterized by the atom's spectroscopic state with nl_j. All important values following from these assumptions are listed in table 2.1 [34].

Splitting of peaks also occurs as multiplet splitting, for instance in the manganese core level peak Mn 3s. Multiplet splitting is a final state effect, when two unpaired e$^-$ couple in an atom, resulting in an ion with several possible final state configurations. The several possible energies lead to asymmetrical split lines in the spectrum. Another final state effect are shake-up and shake-off satellites, resulting from

Table 2.1: Quantum Numbers (main quantum number n, azimuthal quantum number l, and total angular momentum quantum number j) and their corresponding spectroscopic state.

Quantum numbers n	l	$j = \lvert l + s \rvert$	Spectroscopic state
1	0	1/2	1s
2	0	1/2	2s
2	1	1/2	$2p_{1/2}$
2	1	3/2	$2p_{3/2}$
3	0	1/2	3s
3	1	1/2	$3p_{1/2}$
3	1	3/2	$3p_{3/2}$
3	2	3/2	$3d_{3/2}$
3	2	5/2	$3d_{5/2}$

made available energy in the relaxation of the final state configuration of an atom. The shake-up and shake-off features occur due to relaxation energy used to excite e^- in valence levels to bound states and unbound states, respectively.

Instrumentation

As X-ray source in XPS usually Mg or Al anodes are used which show characteristic radiation at 1253.6 eV for Mg K_α and 1486.6 eV for Al K_α. Typical operation power ranges from 500 W to 1 kW at 5 to 15 keV anode voltage, so efficient water cooling is essential. To achieve higher energy resolution and remove the Bremsstrahlung background, a monochromator is used, which selects a narrower bandwidth from the natural emission to improve the resolution. This reduces the FWHM of the K_α to a line width of less than 0.4 eV; as a consequence reduced photon flux reaches investigated surface.

A concentric hemispherical-analyser collects the photoelectrons leaving the sample by an electrostatic lens system, which focuses the e^- onto the analyzer. The analyzer can be biased, that only e^- with the desired kinetic energy, the pass energy E_{pas}, reach the detector. The basic instrumentation is illustrated in figure 2.6.

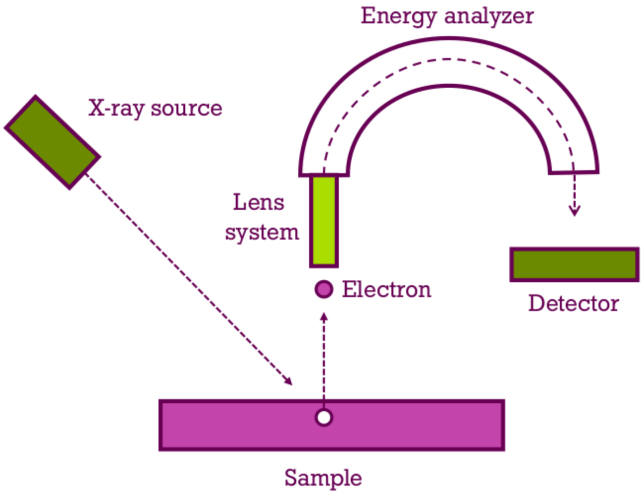

Figure 2.6: Illustration of the working principle of an XPS measurement. X-rays from a X-ray source eject e^- from the surface of a sample which then are collected by electron optics and guided through an hemispherical energy analyzer onto the detector.

Quantitative analysis

XPS is used for quantitative analysis to investigate the relative concentration of different elements in the sample, based on the intensity of an observed peak in the spectrum. The peak intensity I for a homogeneous surface is described mathematically as

$$I = N \times \sigma \times D \times J \times L \times \lambda_\text{i} \times A \times T \tag{2.18}$$

where N is the atomic concentration of an element in the surface in atoms cm^{-3}, σ the photoelectric cross-section (also known as the Scofield factor) in cm^2, D the detector efficiency, J the X-ray photon flux in photons $\text{cm}^{-2}\,\text{s}^{-1}$, L the orbital symmetry factor, λ_i the inelastic mean free path in cm, A the analysis area in cm^{-2}, and T the analyzer transmission efficiency. All variables but N on the right hand side of equation 2.18 are summarized as the elemental sensitivity factor S to simplify towards

$$N_\text{x} = \frac{I_\text{x}}{S_\text{x}} \tag{2.19}$$

with x describing the investigated element. The intensity I_x is taken from the spectrum after suitable background correction, and S_x has to be evaluated with respect to the unique elemental values in the variable. Errors are expected to occur, since σ is a calculated value with unknown magnitude and λ reveals an estimated error of ±50 %.

2.4 Raman Spectroscopy

Raman spectroscopy is a powerful characterization method that involves the interaction of molecules with electromagnetic radiation, measuring the vibrational, rotational, and other low-frequency modes of molecules. It is a non-destructive, high selective technique that can be used for qualitative and quantitative analysis [35].

Principle of the Raman Effect

When a sample is exposed to monochromatic light in visible region, the sample absorbs light and a major portion of the light is transmitted. A minor part of the light is scattered by the sample in all directions, which can be observed at the right angle to the incident beam. The incident light has a particular frequency ν_i. If the scattered light has a frequency ν_s same as the incident light, then the scattering is called Rayleigh scattering [36].

It has been observed that about 1% of the total scattered light occurs at frequencies different from the incident one, which is called Raman scattering [37]. The atoms have different vibrational levels that are defined by specific energy differences. When incident monochromatic light interacts with an e^- in the sample, it absorbs energy from the incident photon and rises to a virtual state (*virtual* in this case is describing a state of energy which is not stationary in quantum mechanics—neither the next excited state, nor a vibrational level is reached) of energy E which is given by the formula

$$E = h\nu_i \tag{2.20}$$

The e^- then falls back to an energy level by losing energy. Three different kind of reflections are possible which are displayed in figure 2.7. If the energy lost equals the energy of the incident photon $h\nu_i$, the e^- falls back to its initial level and—in this process—emits another photon. Since the energy lost is equal to the energy of $h\nu_i$, the released photon has same frequency ν_i as the $h\nu_i$ and Rayleigh scattering occurs [38, 36].

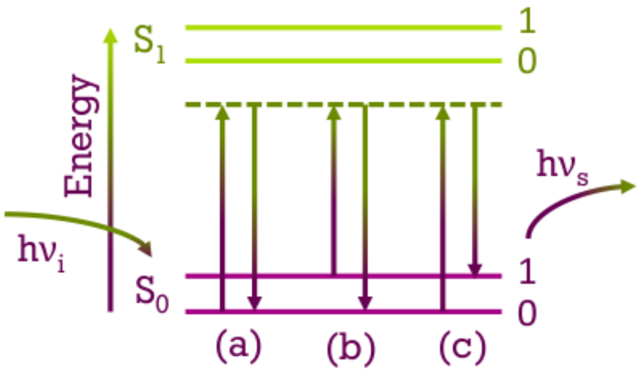

Figure 2.7: Different reflection types for an incident photon ($h\nu_i$) exciting an electron from the ground state S_0 to a virtual state below the first excited state S_1: Rayleigh scattering (a), Stokes-Raman scattering (b), and anti-Stokes-Raman scattering (c).

Sometimes e^-, when losing energy from the virtual state, fall back to a different vibrational level. In this case, the energy lost by the e^- is different from the absorbed energy. Depending upon the final energy of the e^-—the final vibrational level of the e^-, respectively—Raman scattering is separated into Stokes lines and anti-Stokes lines. If the frequency of the scattered photon $h\nu_s$ is less than the incident photon ($\nu_s < \nu_i$), Stokes lines are observed in the Raman spectra. Similarly, when the frequency of $h\nu_s$ is greater than the incident photon ($\nu_s > \nu_i$), Anti-Stokes lines are observed which means the e^- emits energy.

The Raman spectrum gives the molecular fingerprint and is varying for different molecules. Similarly, the intensity of particular Raman lines help to determine the concentration of a molecule in a sample, allowing quantitative analysis [39].

Instrumentation

For Raman spectroscopy, the energy shift of a scattered photon is measured in cm^{-1} against the frequency of occurrence with only one in 10^7 photons being relevant for the Raman effect. Nowadays, Raman spectroscopy is usually implemented in other optical instruments, *e.g.* confocal microscopy. A exemplified setup for a confocal Raman microscope is given in figure 2.8.

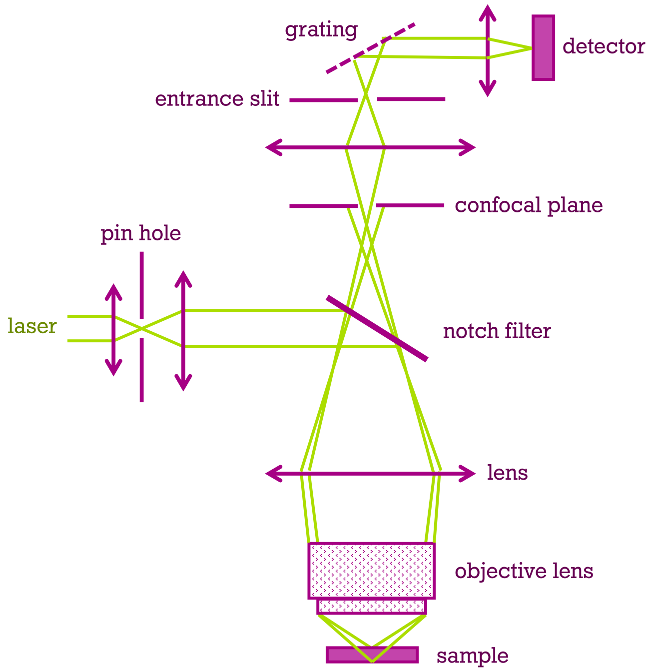

Figure 2.8: Schematic of a confocal Raman microscope with all relevant components (violet) and the way of the laser light (chartreuse).

In confocal microscopy, a laser is focused onto a sample trough a microscope objective that also collects the scattered light, directing it onto a confocal plane, leaving only the central part of the beam pass to reach the detector [40]. Since only light from the focal plane is collected by the aperture, the image contrast is strongly enhanced and surface processes can be monitored more easily. A detailed description on all components of a Raman microscope and the discussion of their settings can be found in section 4.7.

Surface Enhanced Raman Spectroscopy

The concept of surface enhanced Raman spectroscopy (SERS) was first introduced by Fleischmann *et al.* [41] in 1974, measuring the adsorption of pyridine on roughened silver electrodes. Coupled with resonance Raman spectroscopy (RRS), much higher intensities of up to ten orders of magnitude are reported [42].

Operando Raman Spectroscopy

A powerful step into understanding catalysis is studying electrodes under genuine reaction conditions. This is provided by *operando* spectroscopy, which allows characterization of a material and catalytic activity/selectivity simultaneously [43, 14].

In opposition to *in situ* measurements, *operando* spectroscopy provides information about the dynamics of catalytic active sites [16]. The reaction intermediates on a surface are studied and conclusions regarding the active structure can be made.

3 Research on Transition Metal (Ni, Mn) Oxides as Catalyst Electrode Material for Electrochemical Water Splitting

To get an overview about the current research on the transition metals nickel and manganese and their corresponding oxides, the general structure and redox chemistry of NiO_x and MnO_x is edited along with their employment as electrocatalyst towards the OER in this chapter. A special focus lies on their behaviour under irradiation of light in Raman spectroscopy.

3.1 Nickel (Hydr)oxide as Catalyst Electrode Material

Nickel monoxide (NiO) is part of the 3d transition metal oxides (TMO). It has a face centred cubic (fcc) structure with a lattice constant of $a = 0.4168\,nm$ [44]. In its ground state, Ni is in an Ni^{II} oxidation state with a rock salt structure [45]. The single-crystal has a density of $6.67\,g\,cm^{-3}$ [46]..

Nickel hydroxide ($Ni(OH)_2$) has a hexagonal structure with lattice constants $a = 0.312\,nm$, $b = 0.312\,nm$, and $c = 0.460\,nm$, and angles of $\alpha = 90°$, $\beta = 90°$, and $\gamma = 120°$ [47], and occurs in two different pseudo-polymorphs:

(a) α-$Ni(OH)_2$ consists of random $Ni(OH)_2$ layers with intercalated anions or H_2O [48];

(b) β-$Ni(OH)_2$ has a hexagonal close packed structure (hcp) and consists of Ni^{2+} and OH^- ions [49]. Naturally it occurs as the mineral theophrastite [50]. Its structure is isomorph with $Mg(OH)_2$ [51].

The main difference of the two nickel hydroxides is the layer distance which is *ca.* 0.76 nm for α-$Ni(OH)_2$, and 0.46 nm for β-$Ni(OH)_2$ [52]. Both $Ni(OH)_2$ can further be oxidized to their corresponding nickel oxyhydroxides γ-NiOOH and β-NiOOH.

Redox chemistry of $Ni(OH)_2$ in alkaline media

The redox system of $Ni(OH)_2$/NiOOH is well-studied, based on Ni being an extensively used element for all kinds of electrochemical applications such as electrolysers, fuel cells, and alkaline batteries [53].

In 1966, Bode *et al.* [54] proposed a basic scheme regarding the redox processes of $Ni(OH)_2$. Their scheme involves the formation of β-$Ni(OH)_2$ by ageing α-$Ni(OH)_2$, and a reversible redox reaction towards nickel oxyhydroxide (γ-NiOOH and β-NiOOH) and vice versa. The scheme later got more nuanced and the dotted arrows (the dotted arrows are understood as partial reactions) were added [55, 49].

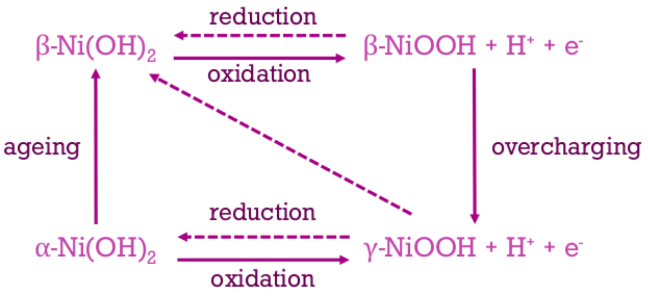

Figure 3.1: General scheme of the electrochemical processes at $Ni(OH)_2$ electrodes, involving ageing, charging, discharging, and overcharging processes. Figure created based on refs [54, 55].

This scheme was proposed without respect to the material texture (recalling that Bode *et al.* [54] published their scheme for electrodeposited $Ni(OH)_2$), electrolyte concentration, and charge and discharge rates [49]. The model might change for $Ni(OH)_2$ prepared by other techniques [53].

The redox processes are designated to the redox peak visible during cyclic voltammetry of $Ni(OH)_2$ in alkaline solution. The basic conversions of the scheme can not be considered stoichiometric, but should be understood as the limited divalent/trivalent material forms [53]. In an oxidation process of $Ni(OH)_2$, the basic chemical equation can be formed as follows:

$$Ni(OH)_2 + OH^- \longrightarrow NiOOH + H_2O + e^- \quad (3.1)$$

Regarding the oxidation state of Ni, this is considered the Ni^{II}/Ni^{III} redox transformation. For both α-$Ni(OH)_2$ and β-$Ni(OH)_2$, the oxidation state of Ni is in the range of 2.0 to 2.2. In oxidized β-NiOOH, Ni shows an oxidation state of 3.0, while for the overcharged γ-NiOOH, it further oxidizes towards a range of 3.5 to 3.7 [53].

Activity of different Ni containing electrocatalysts

Lots of research has been done towards NiO_x as catalyst material for the OER due to the high prize of noble metals Ru and Ir and their limited stability in alkaline media [56]. In fact, hydrous NiO_x layers showed no change in the charge enhancement factor in alkaline media for 14 days [57].

The long time benchmark electrodes Ru and Ir, and their oxide compounds RuO_2 and IrO_2, are reported to have low η towards the OER [58]. Ni-based catalyst have long been considered for OER in alkaline solution due to their low price, high catalytic activity as well as stability [59]. Stern *et al.* [60] investigated NiO_x and $Ni(OH)_2$ NPs towards the OER in alkaline solution and reported η of 300 and 330 mV at $j = 10\,\mathrm{mA\,cm^{-2}}$ for $Ni(OH)_2$ and NiO_x.

Ni is often the material of choice when it comes to forming compounds for water splitting. Moghaddam *et al.* enhanced the catalytic activity of IrO_x with enrichment of Ni. They synthesized Ir-Ni NPs by stirring $IrCl_3$ and $NiCl_2$ in aqueous alkaline solution to achieve η of 280 mV at $j = 10\,\mathrm{mA\,cm^{-2}}$ [61].

Especially Ni-Fe based catalysts are some of the most active and well-investigated electrocatalysts regarding the OER. Zhang *et al.* [62] electrodeposited Ni supported FeOOH on reduced graphene oxide to lower the energy barrier during OER and achieved an η of 260 mV at $j = 10\,\mathrm{mA\,cm^{-2}}$.

Also Fe doping on NiO_x delivers solid performances. The investigation of different Fe content in porous Fe-Ni-O catalysts delivered η of 328 mV at $j = 10\,\mathrm{mA\,cm^{-2}}$ for an Fe content of 15 % [20]. Further explained by Li *et al.* [63], Fe^{III} promotes the formation of catalytically most active Ni^{IV} due to the role of Fe^{III} as a Lewis acid in host NiO_x [63].

Ni can also improve OER catalysts as a substrate material, such as porous Ni foam. Lei *et al.* electrodeposited RuO_2 on Ni foam and obtained η of 288 mV at $j = 20\,\mathrm{mA\,cm^{-2}}$. Further, they improved the performance of the foam by electrodepositing NiFeOH to achieve $\eta = 264$ mV at the same current density [64].

Based on the observations in literature, it is important to state the difficulty of comparing overpotential values as bare numbers, since one has to respect the surface involved in the OER. A significant comparison is therefore only given for similar surface areas, which is why flat electrodes are used in this work.

Operando Raman spectroscopy $NiO_x/Ni(OH)_2$ electrodes

The oxidation of $Ni(OH)_2$ to NiOOH has been discussed before. Measurements of NiOOH have to be performed *operando* (or at least *in situ*) since the oxidation is reversible and the Ni^{II}/Ni^{III} system transforms back to the $Ni(OH)_2$ state when reduced or discharged.

The Ni^{II} phases α/β-$Ni(OH)_2$ have been studied as thin films, for instance by Hall *et al.*, who performed Raman spectroscopy on dry films with 1 mW of 457 nm laser light and a 100× objective [65].

They observed a weak feature at *ca.* 1556 cm^{-1}, corresponding to a two-magnon transition from the antiferromagnetism of NiO_x at RT, that vanishes in $Ni(OH)_2$ under formation of an O–H stretching mode at *ca.* 3575 cm^{-1}.

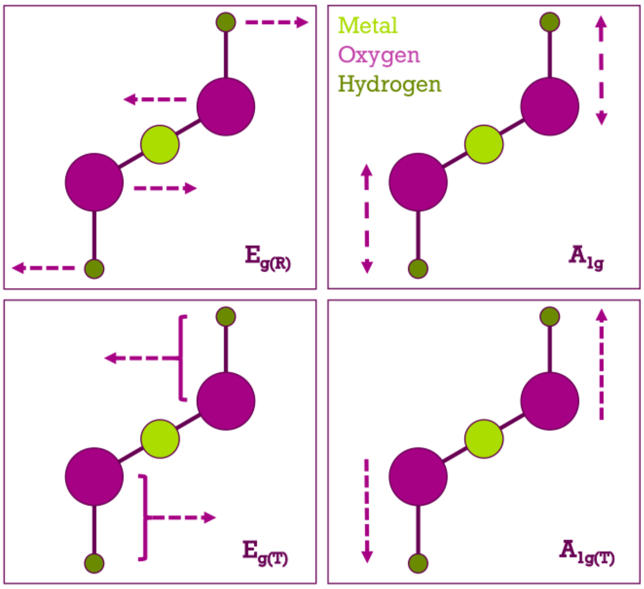

Figure 3.2: Molecular Raman modes in a $M(OH)_2$ molecule. Dotted arrows indicate the direction of vibration for each atom/bond [51].

For β-$Ni(OH)_2$, four Raman-active transitions are predicted by group theory, two with E_g and two with A_{1g} symmetry [66]. A schematic overview of these modes is given in figure 3.2. Three of these modes are located at 310 to 315 cm^{-1}, 445 to 453 cm^{-1}, and 3581 cm^{-1} while the fourth transition has not been determined clearly [65, 51]. Since β-$Ni(OH)_2$ and $Mg(OH)_2$ are isomorph, the same Raman bands occur. These vibrational bands are well studied and summarized from different sources in table 3.1.

Yeo *et al.* [73] used *operando* Raman techniques to study the oxide layer formation on NiO_x films on Au and Pd during OER in 0.1 M KOH. They observed the Ni^{II}/Ni^{III} redox transition of α-$Ni(OH)_2$ towards γ-NiOOH as well as from β-$Ni(OH)_2$ (formed during ageing of α-$Ni(OH)_2$) to the more active β-NiOOH. However, they noted NiOOH might not be the active species during O_2 evolution. Furthermore, they attributed an interaction of Ni with highly electronegative Au to increase the activity of thin layers of NiO_x.

An important reference for this thesis is the work by Diaz-Morales *et al.* [72], who not only studied the Ni^{II}/Ni^{III} redox mechanism by *operando* Raman spectroscopy, but also suggested a deprotonation step of Ni^{III} in NiOOH towards Ni^{IV}. For electrodeposited $Ni(OH)_2$, they discovered a double peak above 1.35 V *vs.* RHE that is attributed to a O−O vibration in $NiOO^-$, where Ni^{IV} is present, resulting in the outstanding performance of Ni as non-noble anodic electrocatalyst material.

3.2 Manganese Oxide as Catalyst Electrode Material

MnO_x compounds gained severe interest for water splitting being known as the only system in nature to catalyze water oxidation [74]. The oxygen evolving complex (OEC) of Photosystem II (PSII) is a Mn_4O_5Ca cluster. PSII is part of the photosynthesis system of plants, algae, and cyanobacteria, inhibiting Mn in oxidation states from II to IV [75, 76]. The oxygen atoms serve as oxo-bridges linking five metal atoms and four H_2O molecules bound to the cluster[77].

Additionally to being the OEC in nature, attention to Mn as water oxidation catalyst compound has been given due to its low cost and its non-toxicity [74, 78]. To address fundamental research regarding Mn compounds with respect to its oxidation state in PSII, this work focuses on basic manganese oxides (MnO_x) as in MnO (Mn^{II}), Mn_2O_3 (Mn^{III}), and MnO_2 (Mn^{IV}) which shall be further elaborated:

- MnO ($Mn^{II}O$) has a rock salt structure with Mn^{2+} cations and O_2^- anions being octahedrally coordinated [79];
- Mn_2O_3 ($Mn^{III}O$) does not occur in nature as γ-Mn_2O_3 and crystallizes tetragonally, changing into α-Mn_2O_3 above 500 °C [80], revealing a cubic bixbyte structure [81].

Table 3.1: Raman bands (cm^{-1}) observed in literature for $Mg(OH)_2$ and β-$Ni(OH)_2$.

Oxide	Raman shift (cm^{-1})																Ref.
NiO							570	730			906	1090	1490				[67]
$Mg(OH)_2$	282		445						803							3654	[66]
β-Ni(OH)2		310	445		510									3570	3600	3680	[68, 69, 51, 70]
		315	450		517					880				3580	3600		[71]
		313	447		508									3581	3601		[51]
			457		504												[72]
γ-NiOOH				479		558											[73]
β-NiOOH				486		561											[73]
				482		562											[72]

- MnO_2 ($Mn^{IV}O$) crystallizes in the rutile structure as β-MnO_2 with three-coordinate oxide and octahedral metal centres [82]. At least six modifications of MnO_2 have been characterized (α, β (pyrolusite/Braunstein), γ (spinel), δ (birnessite), ε, and ramsdellite) which differ in their degree of crystallinaty. [79, 83].

MnO_x features a variety of different possible oxidation states which is why knowledge about redox reactions is of great importance. Heating MnO_x in air results in phase transitions. MnO_2 is converted to Mn_2O_3 between 500 to 600 °C and further reduced to Mn_3O_4 above 890 °C in air [84]. Concluded by DSC studies, heating under Ar atmosphere results in thermal decomposition of MnO_2 to Mn_2O_3 at 590 °C under O_2 evolution [85].

Raman Spectroscopy of MnO_x

A variety of studies have been carried out to determine the Raman scattering (RS) frequencies of manganese oxides. Buciuman *et al.* [86] used violet (457.9 nm), green (514.5 nm), and red (647.1 nm) laser light to examine bulk MnO_x in different oxidation states. They obtained β-MnO_2 and prepared Mn_3O_4 and α-Mn_2O_3 by heat treatments. Julien *et al.* [83] investigated a variety of MnO_x by pelletizing powders, using 514.5 nm laser light with an excitation power of 10 mW. The phase-transformation in α-Mn_2O_3 (synthesized by thermal decomposition of $MnCO_3$ powder) nanocrystals was studied during catalytic combustion, assigning three prominent features to α-Mn_2O_3 at 686, 637, and 307 cm^{-1}. Gao *et al.* [87] used 99.9 % pure powders to elaborate the RS differences between α- and β-MnO_2, finding one characteristic Raman band at *ca.* 665 cm^{-1} for β-MnO_2 (rutile), and two bands at 574 and 634 for α-MnO_2 (hollandite), based on their crystal structure.

Table 3.2: Raman bands (cm^{-1}) observed in literature for MnO_x.

Sample	Raman shift (cm^{-1})									Ref.
MnO	250				531	591	654			[83]
					544		648			[88]
					521	595	645			[86]
Mn_3O_4		319	374				659			[89]
		315	365				651			[86]
		310	357	485		579	653			[83]
α-Mn_2O_3		307					637	686		[90]
				509		581	650			[86]
		311					653	697		[88]
α-MnO_2		328	389		517	580	632		751	[91]
β-MnO_2		319	377	486	538		665		750	[83]
γ-MnO_2	246	337	379	491	520	572	630	670	738	[83]

Available literature on RS data for MnO_x is plenty and therefore difficult, especially if the structure of amorphous thin films is unknown. Table 3.2 gives an overview of the typical wavenumbers of MnO_x Raman bands. The characteristic frequencies have to be applied supported by XPS results for better knowledge of the sputtered species.

Potential dependent behavior of MnO_x

The use of *in situ/operando* techniques to study the electrochemical behavior of MnO_x is of great help to overcome most of the speculative processes ocurring in literature. Messaoudi *et al.* [92] used *in situ* Raman spectroscopy to investigate the Mn oxidation states on metallic Mn at various applied potentials in alkaline media. The ocurring species were attributed with ref [93]. Below 0.5 V *vs.* RHE, Mn_3O_4 (Haussmanite) was observed, oxidizing towards Mn_2O_3 (Bixbyite) at 0.9 V *vs.* RHE, followed by a partly transformation to MnO_2 (Ramsdellite) above 1.4 V *vs.* RHE. At high potentials above 1.7 V *vs.* RHE, a color change of the electrolyte was associated with the formation of MnO_4^-.

Bernard *et al.* [93], studied non-stoichiometric MnO_x samples—deposited by various methods—at applied potentials with Raman spectroscopy in 0.1 M $Na_2B_4O_7$. They found electrochemical deposited MnO_x to reveal Mn_2O_3 character when in contact with electrolyte, further oxidizing to MnO_2 during cycling, attributed due to a vanishing peak at 580 cm^{-1} and an emerging peak at 650 cm^{-1}. Thermally deposited (evaporation of metallic manganese in an Ar/O_2 atmosphere) Mn_3O_4 showed the appearance of Mn_2O_3 during a potential of 0.1 to 0.7 V *vs.* RHE unrecoverable.

Recently, An *et al.* [94] studied the performance of MnO_x. They electrodeposited birnessite (δ-MnO_2), bixbyite (α-Mn_2O_3), and a mixture of birnessite-bixbyite on ITO substrates and investigated the O_2 evolution behaviour in 0.1 M KOH. They attributed a OER activity of below 0.1 mA cm^{-2} well above 1.8 V *vs.* RHE for α-Mn_2O_3, but stated higher performance for the mixed phase above 1.83 V *vs.* RHE, also compared to pure δ-MnO_2. By *operando* Raman studies, they attributed this behaviour to a charging process, initiating a triclinic to hexagonal transformation and formation of point defects in MnO_x. This process is observed by a peak shift from 625 to 650 cm^{-1} in δ-MnO_2 and from 630 to 642 cm^{-1} in the mixed phase by applying a potential of up to 1.85 V *vs.* RHE. Similar intense peak at 635 cm^{-1} was found by Xu *et al.* [21] for α-Mn_2O_3 during methane combustion along with a weaker feature at 341 cm^{-1}.

Gosztola *et al.* [95] investigated the structural changes of 10 nm thin MnO_x films. They electrodeposited MnO_2 (γ-MnO_2 with ramsdellite (R-MnO_2) structure along with randomly distributed domains of β-MnO_2 and $Mn(OH)_2$ on an electrochemically roughened Au electrode. Then, they performed *in situ* Raman spectroscopy during galvanostatic reduction (0.16 to -0.96 V *vs.* RHE) and linear sweep voltammetry (0.22 to -0.90 V *vs.* RHE) in 1 M KOH. A broad band at 585 cm^{-1} was attributed to the Mn−O vibrations prior to the reduction process, a growing band at higher cathodic potentials at 670 cm^{-1} was associated with electron rich Mn−O−Mn units, along with a 415 cm^{-1} band assigned to Mn−OH in MnOOH, and a 470 cm^{-1} band attributed to Mn−OH species in $Mn(OH)_2$.

The potential induced behaviour of MnO_x relies on a variety of factors, such as the oxidation state, crystal structure, electrolytic environment, and deposition process, so RS bands have to be assigned with care and respect to the experimental section of the literature.

4 Experimental

This chapter is meant to explain the conduction of the experimental work in this thesis. First, an overview of the ultra high vacuum system, where samples have been synthesized and analysed, is given. After that, the exact preparation and production procedure of substrates and samples is written down. Then, the use of X-ray photoelectron spectroscopy, electrochemistry, and Raman spectroscopy as investigative methods is explained in detail regarding instrumentation, parameters, and measurement processes.

4.1 General Experimental Procedure

The samples in this work underwent an experimental procedure, depicted in the flow diagram in figure 4.1, based on which this chapter explains the methods and parameters used to investigate the electrocatalysts. The overall procedure started with the substrate preparation, surface enhancement for Au, a HNO_3 etch for Ni foil, and a polishing and grinding procedure for stainless steel (SS), followed by deposition of TMOs *via* reactive magnetron sputtering. The chemical composition was determined with XPS in line to address discrepancy of activity in EC. Raman spectroscopy was performed as a characterization technique and *operando* to investigate surface processes during the OER. XPS was again performed after EC to find permanent surface chemistry changes of the sample.

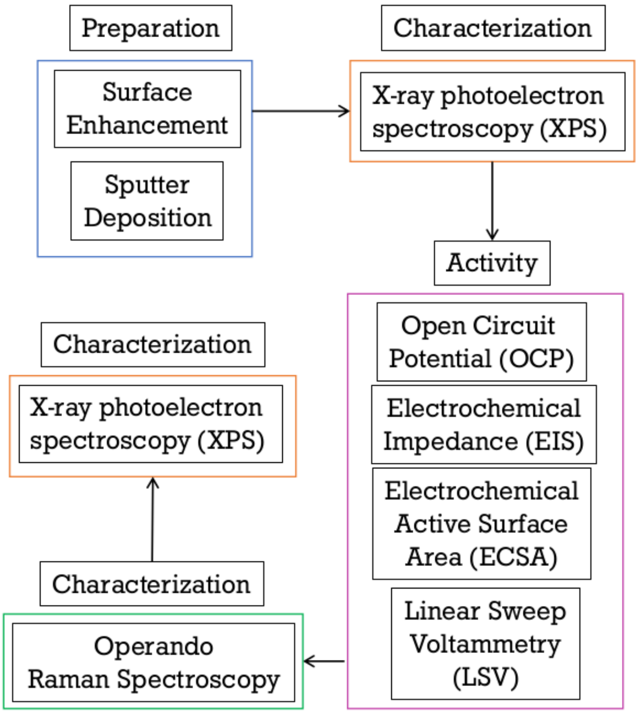

Figure 4.1: Overview of the experimental procedure in this work. Starting from preparation, the timeline is indicated by black arrows. All steps are explained in this chapter in detail.

4.2 Darmstädter Integrated System for Fundamental Research

Reactive magnetron sputtering and XPS investigation have been conducted in the **Da**rmstädter **I**ntegrated **Sy**stem for **Fun**damental research (DAISY Fun). A detailed view of the DAISY-Fun is found in figure 4.2, a picture of the UFO is displayed in figure 4.3.

Samples are introduced into the ultra high vacuum (UHV) *via* two different load locks. UHV in the DAISY-Fun means an operating pressure of 10^{-8} to 10^{-10} mbar. To introduce samples, the load lock is fluted with N_2. The MBE-chamber possesses a height-adjustable, rotatable sample manipulator where a holder for a maximum of four $\sim 1\,\mathrm{cm} \times 1\,\mathrm{cm}$ samples is placed. Two different sputter sources enable co-sputtering with stoichiometry control by two different power boxes. A heater with adjustable height is mounted above the sample holder for annealing or sputtering at elevated temperatures. The system allows sample movement by manipulator arms to measure XPS in line without atmospheric contact.

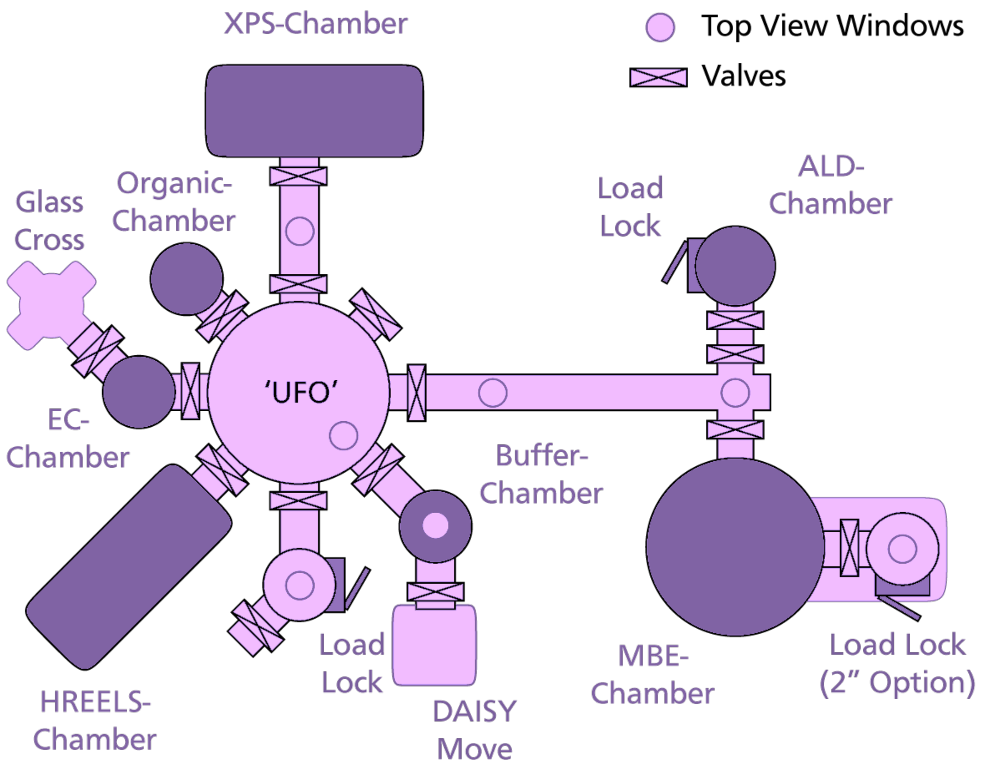

Figure 4.2: Darmstädter Integrated System for Fundamental Research (DAISY Fun); all parts of the ultra high vacuum (UHV) system are shown in the figure; important for this work were the MBE chamber, the XPS chamber, the 'UFO', the load lock connected to the 'UFO', the tube connecting the 'UFO' and the MBE chamber, and the load lock (2" option) connected to the MBE-chamber.

4.3 Substrate Preparation

Different substrates were used for the sample deposition. Most measurements in this work were conducted on three coin-shaped gold plates (Schiefer % Co., 99.9 % purity) with a diameter of 12 mm and 1 mm in thickness. The surface composition was validated with XPS measurements. Most peaks visible in the spectra (figure 5.2) can clearly be assigned to gold. The carbon core level peak C 1s can be detected due to contact with atmosphere before.

Au: Pure gold was used to allow surface enhanced Raman spectroscopy (SERS) for investigation of thin metal oxide layers. For increasing the intensity of the vibrational bands in Raman spectroscopy, the surface of gold is enhanced. A detailed description of the process and its results can be found in section 5.

Stainless steel: Austenitic stainless steel (SS, X5CrNi18-10, 1.4301) with an area of 1 cm^2 has been used as a substrate. The chemical composition is listed in table 4.1.

Table 4.1: Chemical Composition of the Stainless Steel Substrates. All values regarding the element fraction are given in mass-%.

	C	Si	Mn	P	S	Cr	Ni	N
min.	-	-	-	-	-	17.5	8.0	-
max.	0.07	1.0	2.0	0.045	0.03	19.5	10.5	0.1

The unworked SS were sanded to a plane and homogeneous surface with abrasive SiC grinding paper (Struers) of European (P-grade) grit sizes of P320, P1000, P2400, and P4000 at a speed of 150 rpm for 10 to 20 min each. Afterwards, the samples were cleaned in an ultrasonic bath in distilled H_2O for 5 min to remove residual dust and material.

Diamond polishing (DP-Paste M, Struers) steps were executed with grain sizes of 6, 3, 1, and 1/4 µm with a single force sample operation of 15 to 20 N with a wheel and specimen holder speed

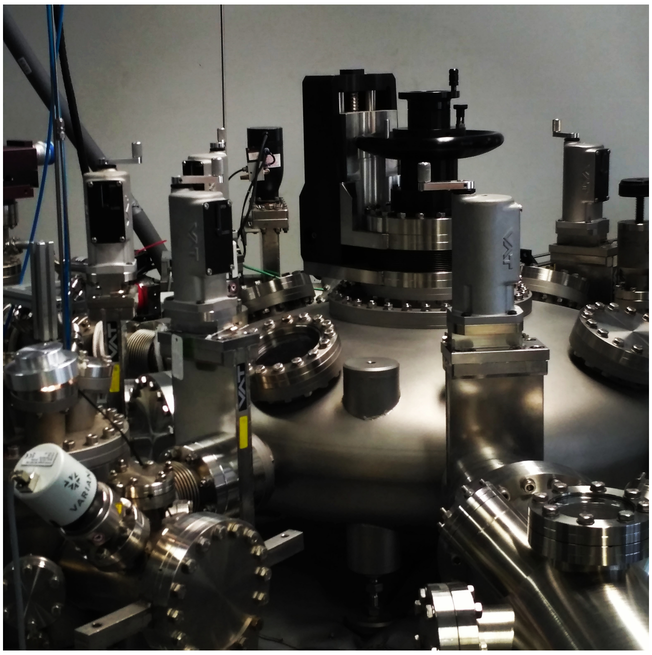

Figure 4.3: Photography of the Daisy-Fun UFO, connecting load lock, tube from MBE, and XPS with a 360° rotatable manipulator arm. The pressure in each chamber is secured with VAT UHV gate valves.

in the opposite direction at 150 rpm for 4 min. A lubricant (DP-Lubricant Blue, Struers) was provided to moist and cool the substrates. After each step, the substrates were rinsed with H_2O. Sanding and polishing was executed on a Buehler Phoenix 4000 sample preparation system. To remove all residual dirt, glue, and diamond paste from the substrates, they were cleaned two times in acetone and once in isopropanol in an ultrasonic bath for 10 min each.

The substrates were coated with a thin Au layer afterwards. While still being an electric conductor, Au has an extensive double layer region which in the presence of most electrolytes shows no Faradaic behaviour [96]. This allows proper investigation of top layers without errors due to catalytic activity of SS. As it is seen in table 4.1, SS contains high amounts of Ni which is known to be an excellent non-precious catalyst towards the OER in alkaline media. Au layers were deposited in a Quorum Q300T D Sputtercoater—designed to grow metallic thin films by Ar-sputtering on metallic targets—with an Au-target at a current of 30 mA over 125 s, to generate an intermediate layer of *ca.* 50 nm thickness.

Ni foil: Ni foil with an area of 1 cm^2 has been cut out of a thin Ni sheet with a thickness of *ca.* 1 mm. To remove the native passivating oxide layer of the foil, an etching process was conducted according to ref [97].

The substrates were etched in dilute nitric acid (3 parts HNO_3 to 7 parts H_2O) for 30 s and immersed in millipore water. Afterwards, they were rinsed with CH_4O and dried under N_2. Concentrated HNO_3 is known as a rapid etching agent for Ni, so diluting with H_2O will decelerate the process. After etching, the substrates were immediately introduced into the UHV to prevent new oxide layer formation.

4.4 Reactive Magnetron Sputter Deposition

The gas mixture for sputtering was set with mass flow controllers (MKS Instruments), using Ar (99.999%, Air Liquide) and O_2. With a heater above the samples, the temperature was adjusted from RT to 600 °C. The substrate holder was rotated at 30 rpm during sputtering to increase the film thickness uniformity [98]. A photography of a co-sputtering process with two active sources is given in figure 4.4. Nomenclature of NiO_x samples is explained in box 4.1, for MnO_x in box 4.2.

NiO_x: For the synthesis of NiO_x, sputtering was performed with a gas mixture of 19.6 sccm Ar and 0.4 sccm O_2 at a DC power of 15 W, using a metallic Ni target (2 in, 99,95 %, Kurt J. Lesker Co.) at 0.03 mbar. The target was pre-sputtered for 2 min with closed shutters before conducting a 9 min deposition. For deposition at elevated temperatures, desired T is hold for at least 5 min before sputtering.

MnO_x: For deposition of MnO_x, a metallic Mn target (Kurt J. Lesker, 99 %) has been used. The target was pre-sputtered for 10 min before each deposition. MnO (Mn^{II}) and MnO_2 (Mn^{IV}) were directly deposited on Au with a DC sputter power of 20 W at a pressure of 0.03 mbar. To grow Mn^{II}, a gas

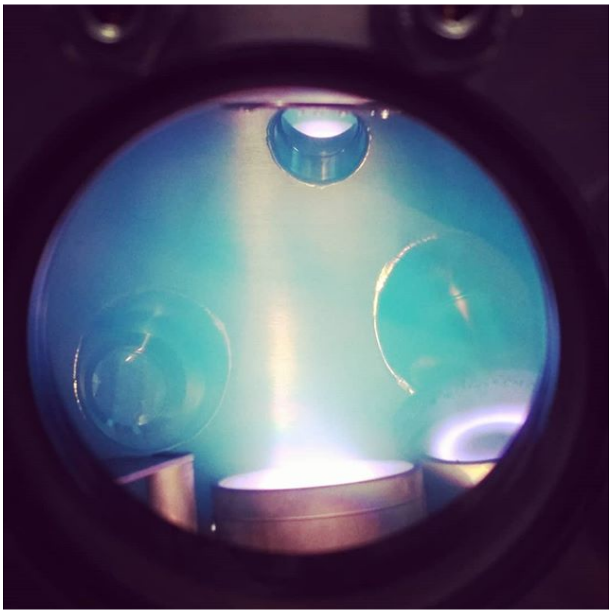

Figure 4.4: Inside the MBE chamber: Both sputter sources active (molybdenum in the front, manganese in the back) during a co-sputtering deposition process. The substrates are mounted on the sample holder at the top of the picture. Sputtering is performed with a Ar/O_2 gas mixture.

mixture of 19.9 sccm Ar and 0.1 sccm O_2 was used, for Mn^{IV}, the Ar content was reduced to 19.6 sccm and O_2 increased to 0.4 sccm. It was not possible to deposit Mn_2O_3 (Mn^{III}) directly on Au, since the usual sputter parameters resulted in thicker layers of Mn^{II}. As a consequence, Mn^{III} was synthesized by sputtering Mn^{IV}, and annealing the sample at 600 °C for 1 h in Ar atmosphere (20 sccm) to thermally reduce the Mn^{IV} species under O_2 evolution according to equation 4.1.

$$2\,MnO_2 \xrightarrow{\Delta} Mn_2O_3 + \frac{1}{2}O_2 \qquad (4.1)$$

4.5 X-Ray Photoelectron Spectroscopy

In XPS analysis, first a survey spectra of the sample is recorded with a relatively high pass energy E_{pas}, low resolution scan over a large E_{BE} range. This survey provides a useful first impression to identify interesting regions which are then investigated with lower E_{pas} and thus higher resolution. In most cases, peaks can easily be identified due to their known position while different oxidation states of an element only vary in a few eV.

For detail spectra, a lower E_{pas} results in lower intensity peaks and therefore higher noise to signal ratio. The noise can be reduced through multiple scans over a region. While the survey only consists of two scans, detail spectra were scanned 10 to 15 times. Also the step width in the survey spectra is *ca.* 1 eV, but is reduced to *ca.* 0.05 eV for detail spectra.

All the XPS measurements have been conducted in line directly after sputter deposition, to avoid contamination of the samples, which means all peaks are directly linked to the corresponding deposition. The XPS measurements were conducted with a hemispherical energy analyser PHOIBOS 150 (Focus 500 with XR50M) from SPECS Co., containing an Al anode with characteristic Al K_α radiation of 1486.74 eV.

Box 4.1: NiO_x—Sample nomenclature

The nomenclature of the samples will give direct insight on the substrate as well as the temperature treating process. Samples will be described as NiO_B^C, where:

- NiO: describes the chemical composition of the sample, NiO for nickel oxide
- B: provides information on the substrate; B could be Ni (nickel), Au (gold), or SS/Au (gold coated stainless steel);
- C: shows the temperature of the heater during the reactive magnetron sputtering process. C is either RT for room temperature, or 200/400/600 for the respective T in degree Celsius.

For instance, a NiO_x sample deposited on Au at a temperature of 600 °C will further be refered to as NiO_{Au}^{600}.

Box 4.2: MnO_x—Sample nomenclature

The nomenclature of the MnO_x samples will be done in a way similar to NiO_x. Samples will be described as Mn_C^B, where:

- Mn: describes the main element in the sample, Mn for manganese
- B: provides information on the main oxidation state of the sample, as it was evaluated as prepared with XPS
- C: gives helpful information on the treatment of the sample, will be EC for samples after electrochemistry

Figure 4.5: Left: Photography of the Photoelectrochemical Cell (PECC-2) from ZAHNER-Elektrik GmbH & Co. KG. used for EC measurements in this work. The cell is build for a three-electrode setup. A window allows observation of the sample during measurements. Right: Picture of a Au sample inside the Zahner cell during O_2 evolution, displaying air bubble adsorption on the surface of the sample.

4.6 Electrochemistry Measurements

A PECC-2 EC cell by ZAHNER-Elektrik GmbH & Co. KG was used for electrochemistry (EC). In a three-electrode setup the current flow between the sample, at the working electrode (WE), and a platinum wire, the counter electrode (CE) is measured. The potential is determined between the WE and the reference electrode (RE), in this case either an Ag/AgCl (0.210 V *vs.* NHE) or an Hg/HgO (0.250 V *vs.* NHE) electrode. Using an o-ring with a diameter of 7 or 8 mm, a catalytic surface of $\sim$ 0.385/0.503 cm^2 is exposed to the 0.1 M KOH (99.98 %, Carl Roth) electrolyte.

Before each experiment, the RE was calibrated by recording the open circuit potential (OCP) over a time span of 600 s as displayed in figure 4.6. The saturation value (E_{RE}) is used to select the measurement ranges for the experiment, since the scale shifts based on the RE and the pH value of the electrolyte according to Nernst equation (see equation 2.5).

During the calibration, the Zahner cell was prepared. All cell parts were cleaned with millipore H_2O and dried under N_2. Afterwards, the sample and the RE were assembled to the cell, and electrolyte was filled in. The complete cell then was mounted in a three-electrode setup.

NiO_x: All experiments were performed using a Interface 5000E potentiostat (GAMRY instruments), following a basic sequence (which was corrected in regard to the potential of the RE) as following:

(1) OCP (600 s) of Ag/AgCl *vs.* RHE
(2) OCP (300 s) of the sample
(3) EIS at OCP (1 MHz to 5 Hz)
(4) EIS at 1.1 V *vs.* RHE (1 MHz to 5 Hz)
(5) LSV at 1.0 to 2.0 V *vs.* RHE with 10 $mV\,s^{-1}$
(6) CV at 1.02 to 1.12 V *vs.* RHE (10 cycles) for different scan rates (10, 20, 50, 100, 150, 200, 250 $mV\,s^{-1}$); holding at 1.07 V for 120 s before each new scan rate;
(7) CA for 900 s at 1.52 V *vs.* RHE
(8) LSV at 1.0 to 2.0/2.1 V *vs.* RHE with 10 $mV\,s^{-1}$
(9) CA for 3600 s at 1.52 V *vs.* RHE
(10) LSV at 1.0 to 2.0 V *vs.* RHE with 10 $mV\,s^{-1}$
(11) CA for 300 s at 1.52 V *vs.* RHE
(12) CV at 1.02 to 1.12 V *vs.* RHE (10 cycles) for different scan rates (10, 20, 50, 100, 150,

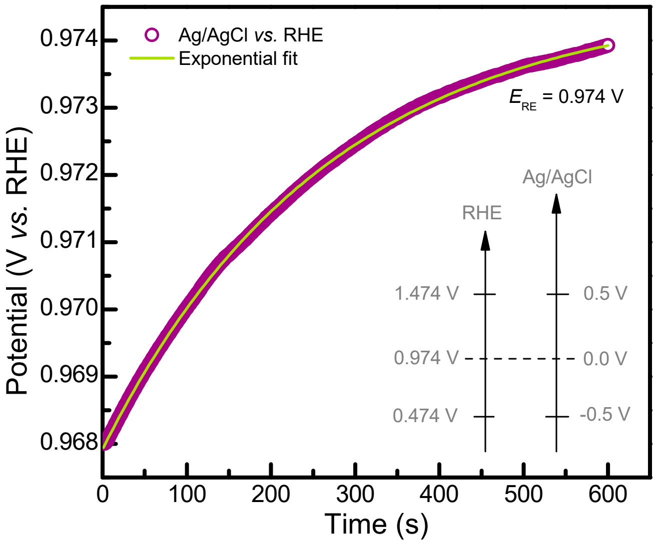

Figure 4.6: Open circuit potential (OCP) of used Ag/AgCl RE *vs.* RHE for calibration of the potential shift. The relation between Ag/AgCl and RHE is indicated in gray.

200, 250 $\mathrm{mV\,s^{-1}}$); holding at 1.07 V for 120 s before each applied scan rate

Since obtained data is measured as E_m *vs.* Ag/AgCl, all values have to be corrected to the RHE scale. Furthermore, the potential is adjusted to the IR_{el} drop from the electrolyte with the equation

$$E_{RHE} = E_\mathrm{RE} + E_\mathrm{m} - I_\mathrm{m}R_\mathrm{el} \tag{4.2}$$

where E_RHE is the potential on the RHE scale, E_RE the potential of the reference electrode (Ag/AgCl or Hg/HgO), E_m and I_m are the measured potential and current, and the resistance of the electrolyte is R_el. The reference potential is determined *via* measurement (1) as described above. The resistance of the electrolyte is determined *via* electrochemical impedance spectroscopy (EIS). The impedance value at a frequency of 10×10^{-3} Hz—determined with measurement (3)—is considered R_el. The overpotential η was calculated using

$$\eta = E_\mathrm{RHE} - 1.23\mathrm{V} \tag{4.3}$$

with 1.23 V being the theoretically needed voltage to split water. Current densities were calculated using the geometric surface areas, recalling that all substrates but nickel foil were polished to mirror finish. Chronoamperometry (CA) steps are performed with respect to the nickel oxidation wave, where $\mathrm{Ni^{II}}$ is oxidized to $\mathrm{Ni^{III}}$. To approximate the electrochemical double layer capacitance (EDLC) of the catalysts, cyclic voltammograms (CV) in a potential range of 1.02 to 1.12 V *vs.* RHE are recorded for scan rates of 10 to 250 $\mathrm{mV\,s^{-1}}$. Linear sweep voltammetry (LSV) is used to characterize the activity of the catalyst regarding its kinetic parameters, such as η and Tafel slopes.

$\mathrm{MnO_x}$: Manganese oxide catalysts have also been characterized electrochemically similar to $\mathrm{NiO_x}$. EC was performed in 0.1 M KOH using Ag/AgCl and Hg/HgO as RE. Due to the different main interests in the performance, the measurement sequence has been changed towards EC(I) and is composited of following measurement steps:

(1) OCP (600 s) of Ag/AgCl *vs.* RHE
(2) OCP (300 s) of the sample
(3) EIS at OCP (1 MHz to 5 Hz)
(4) EIS at 1.1 V *vs.* RHE (1 MHz to 5 Hz)
(5) CV at 1.2 to 1.7 V *vs.* RHE (20 cycles) with 5 $\mathrm{mV\,s^{-1}}$
(6) LSV at 1.0 to 1.9 V *vs.* RHE with 10 $\mathrm{mV\,s^{-1}}$
(7) CV at 1.02 to 1.12 V *vs.* RHE (10 cycles) for different scan rates (10, 20, 50, 100, 150, 200, 250 $\mathrm{mV\,s^{-1}}$); holding at 1.07 V for 120 s before each applied scan rate
(8) CA for 1800 s at 0.8 V *vs.* RHE
(9) CV at 1.2 to 1.7 V *vs.* RHE (20 cycles) with 5 $\mathrm{mV\,s^{-1}}$
(10) LSV at 1.0 to 1.9 V *vs.* RHE with 10 $\mathrm{mV\,s^{-1}}$

To fulfil the requirements of the manganese BMBF project and to guarantee observation of the sputtered layers without altering the surface species, another shorter program EC(II) has been conducted for EC and current-voltage curves were measured *vs.* Hg/HgO.

(1) OCP (600 s) of Hg/HgO *vs.* RHE

(2) OCP (300 s) of the sample

(3) EIS at OCP (1 MHz to 0.1 Hz)

(4) CV at 1.0 to 1.9 V *vs.* RHE (5 cycles) with $50\,\mathrm{mV\,s^{-1}}$

(5) CV at 1.0 to 1.5 V *vs.* RHE (50 cycles) with $100\,\mathrm{mV\,s^{-1}}$

(6) CV at 1.0 to 1.9 V *vs.* RHE(5 cycles) with $50\,\mathrm{mV\,s^{-1}}$

(7) CV at 1.0 to 1.9 V *vs.* RHE (2 cycles) with $10\,\mathrm{mV\,s^{-1}}$

The reference potential is determined *via* measurement (1), R_{el} is determined with EIS (3), by identifying Z_{real} at $Z_{\mathrm{imag}} = 0\,\Omega$ (see section 7.2 for detailed procedure). In EC(I), CV between 1.2 to 1.7 V *vs.* RHE has been conducted to activate the catalytic surface, while CV at 1.02 to 1.12 V *vs.* RHE was performed to investigate the EDLC of the samples. The activity is determined with LSV at 1.0 to 1.9 V *vs.* RHE. CA at 0.8 V *vs.* RHE has been done to reduce the surface species.

CV between 1.0 to 1.5 V *vs.* RHE in EC(II) has been conducted to condition the catalyst in a range without O_2 evolution and to observe possible changes of the redox processes. Different scan rates of the catalyst are applied to investigate surface processes attributed to redox changes during OER. Activity investigation is done *via* CV.

4.7 Raman Spectroscopy

As a substrate for SERS to monitor surface processes of thin films, Au or Ag is usually used. The substrate must not reveal Raman active bands overlapping with the compound to be investigated. An important parameter regarding the substrate is the excitation laser wavelength used in the experiment. It has been reported before that Au shows broad fluorescence overlapping with most important signals of the film at a wavelength of 532 nm.

First, Raman spectra were recorded using a confocal Raman microscope (alpha300 R; WITec GmbH, Ulm, Germany). For excitation, the system is equipped with a SHD Nd:YAG laser (532 nm, 22.5 mW) and a lens-based spectrometer with a CCD camera (1024 × 128 pixel, Peltier cooled to −65 °C). A long-pass edge filter was used to reject the shorter wave lengths as well as the elastically scattered photons (Rayleigh scattering and reflexion). A 50× microscope objective (working distance 2.0 mm, NA 1.0) has been used.

As a second instrument, Raman spectra were recorded using a Horiba HR800 micro-Raman spectrometer (Horiba Jobin Yvon, Bensheim, Germany) equipped with an HeNe laser ($\lambda = 632.8\,\mathrm{nm}$). The plasma emission was filtered with an interference filter and a Raman notch filter has been used for laser light rejection. The measurements were performed with a grating of $600\,\mathrm{g\,mm^{-1}}$ and a 50× microscope (NA 0.55), resulting in a spot diameter of $T = 1.22 \times (\lambda/\mathrm{NA}) = 1.4\,\mu\mathrm{m}$, as well as a 100× microscope (NA 0.8), corresponding to a beam diameter of 0.96 µm. The laser power was attenuated using neutral density (ND) filter.

Operando Raman Spectroscopy

The used *in situ* cell (TSC Raman cell, rhd instruments GmbH & Co. KG) and its parts are displayed in figure 4.7. The cell basically consists of a polyether ether ketone (PEEK) housing and cap, and an optical quartz window, made of synthetic SiO_2. A refillable microreference Ag/AgCl electrode allows for a three-electrode arrangement, a gold-plated ring electrode serves as CE. As WE, desired sample is placed on a cylindric copper electrode encased in PEEK.

A view of all cell parts is found in figure 4.7b, as well as a detailed instruction of the mounting

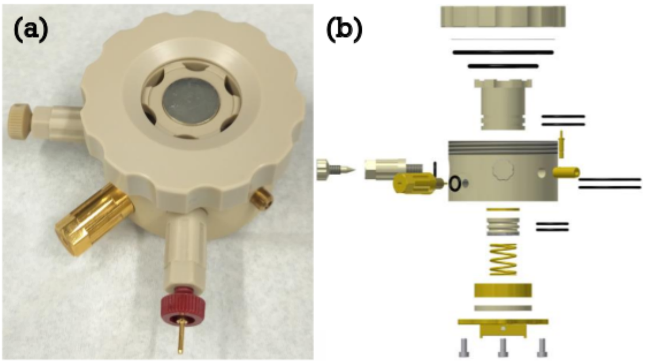

Figure 4.7: TSC Raman cell by rhd instruments; (a) photography and (b) exploded view of the cell (picture taken from rhd instruments application note). A detailed description of the cell and its parts is found in the text and in the assembly instruction in box 4.3.

procedure in box 4.3. The rook-like PEEK chess figure contains the copper electrode, the WE, and the gold-plated spring to connect the bottom gold-plated platform with the sample and is further surrounded by the gold-plated CE ring. A PEEK ring prevents the CE from short-circuiting by touching the bottom platform. The main body features the RE, a gold-plated pin to connect the CE with the potentiostat, and access for the injection. All sealing parts are represented by thick black lines in figure 4.7b.

Choosing the Raman parameters

The spectral resolution of a Raman spectrum depends on several factors, of which some are user controlled by optimizing certain parameters that will be discussed shortly, all with respect to own observations as well as available literature, for instance ref [99]:

- excitation wavelength: three different excitation wavelengths can be selected in the system, including a blue Co (488 nm), a green Ar (514.5 nm), and a red HeNe (632.8 nm) laser. To reduce fluorescence in the SER spectra, the highest possible wavelength of 632.8 nm is chosen. With higher excitation wavelength, the spectral resolution decreases, since the Raman shift is an energy related unit, making a lower grating more important to reduce the illumination time as much as possible.
- excitation power: with the Raman signal being proportional to the excitation power, most of the time the power is chosen as high as possible without thermal degradation of the sample. To prevent thermal reduction of the TMO, the power is adjusted from low to high, until a sufficient signal is achieved.
- objective: the highest NA objective is chosen that still can be applied to experiment with respect to the measurement conditions. Dry samples are inspected with a 100× objective which is not possible for samples mounted in the *operando* cell. The SiO_2 glass hinders the objective from focusing on the surface, because the objective-sample distance is too high. As a result, the 50× objective is used for *operando* Raman spectroscopy.
- grating: the system is equipped with a 600 g mm^{-1}, and a finer 1800 g mm^{-1} grating. As a rule of thumb, a higher grating results in higher resolution. However, a higher groove density grating gives a less intense spectrum, requiring longer acquisition time for an equal intensity. To minimize fluorescence in SERS, the acquisition time is kept as short as possible, making the low resolution diffraction grating the better option.
- confocal hole: the size of the entrance spectrometer confocal hole regulates the amount of light passing through the system on the sample, influencing the spatial resolution. Because of the low illumination time, high confocal pinholes of up to 950 µm in combination with low slit sizes for optimal spectral resolution are used for low scattering samples.

NiO_x: Raman spectra were acquired with a red laser (632.8 nm), by attenuating the power with ND filters (D 0.6) to *ca.* 0.48 mW. The pinhole was set to 200 and the slit size to 100 µm in combination with a 50 × LWD objective, choosing a 600 g mm^{-1} grating. The sample was illuminated for 3 s/scan, accumulating 20 scans each measurement.

MnO_x: Spectra were taken with $\lambda = 632.8$ nm, using a 600 g mm^{-1} grating, setting the pinhole to 950 µm and the slit size to 50 µm. MnO was measured with a D 0.6 filter (*ca.* 0.48 mW), accumulating 20 scans for 3 s each. At applied current, the illumination time was increased to 5 s. MnO_2 and Mn_2O_3 are reported to be easily thermally reduced during irradiation with laser light [86, 87]. These structural changes are avoided by using lower laser power, long wavelengths, larger spot sizes, and shorter exposure times [87]. Therefore, spectra—especially of dry samples—are acquired with a D 1 filter (0.2 mW) for MnO_2 (dry and *operando*), and with a D 2 filter (0.1 mW) for Mn_2O_3, changing to a D 0.6 filter for *in situ* measurements. The aquisition time was set to 3 s for 20 accumulations. Gao *et al.* [87] observed no structural changes of their MnO_x, using a 632.8 nm He-Ne laser at a power of 1 mW for 30 to 60 s of acquisition time.

Comparison of the Raman systems

As stated above, two different Raman laser systems have been used during this thesis. High background fluorescence and low intensity signal were observed using the 532 nm Nd:YAG laser, resulting in a system change towards a microscope equipped with a 632.8 nm excitation source.

Figure 4.8a displays wide range Raman spectra of as deposited NiO_x on surface enhanced Au, giving rise to a high fluorescent background (BG) signal at a laser wavelength of 532 nm. In contrast, the overall signal at 632.8 nm is of lower intensity, but allows recognition of molecular vibrational modes over the BG noise. Both spectra were recorded for an illumination time of 5 s/spectrum, accumulating 30 spectra. The green laser was set to 1 mW, the red laser was attenuated to *ca.* 0.94 mW (D 0.3).

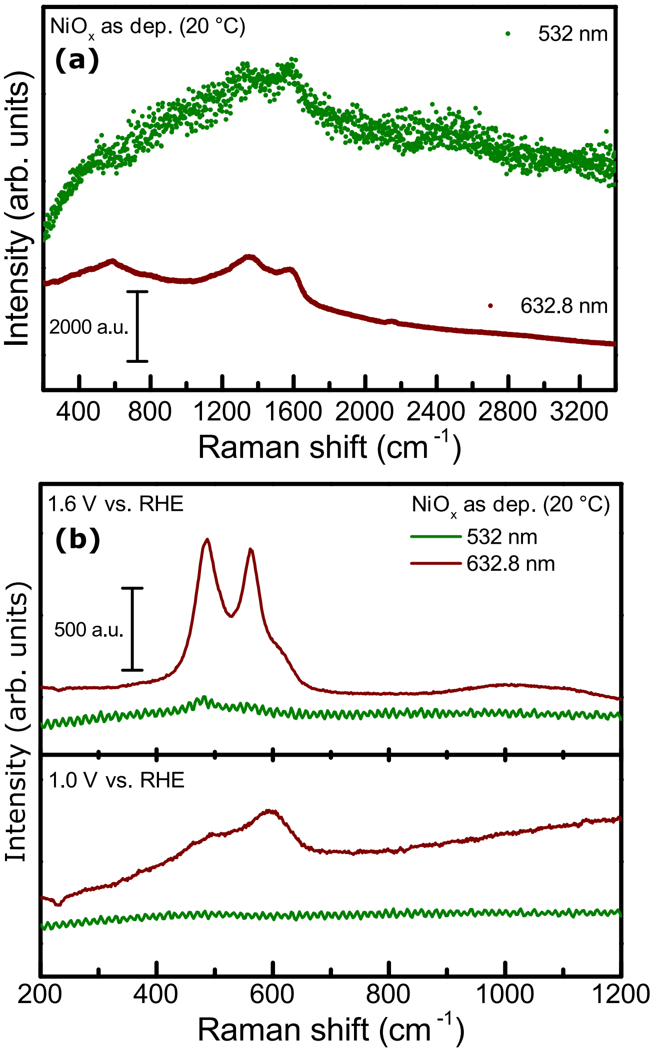

Figure 4.8: SER spectra of NiO_{Au}^{RT}, acquired with a green Nd:YAG laser (olive), and a red He-Ne laser (wine) to address the problem of fluorescence.

Figure 4.8b gives an even better impression of this problem, comparing the same NiO_x sample under working condition at 1.0 and 1.6 V *vs.* RHE.

The green laser spectrum at 1.0 V *vs.* RHE has a high noise and does not allow observation of Ni−O/Ni−OH lattice vibrations in contrast to the red laser spectrum that shows several signals that are attributed to molecular vibrational signals. At 1.6 V *vs.* RHE, two low intensity peaks arise in the 532 nm spectrum, but their signal is vanishing compared to the high intensity double band at 632.8 nm. There is also a broad signal visible between 900–1200 cm^{-1} that is not discriminated between noise and signal at 532 nm excitation.

Compared to MnO_x, the signals of NiO_x are seen as relatively easy to distinguish in Raman spectroscopy, also regarding the chemical change at rising potentials. Since the bands in NiO_x are not visible due to the high amount of fluorescence at 532 nm, the system with higher wavelength is chosen for the rest of this thesis.

Box 4.3: Assembling an filling of TSC Raman measurement cell

This short explanation deals with the correct assembling and filling procedure of the TSC Raman cell used for in situ spectroscopy:

- calibrate the Ag/AgCl micro RE *vs.* RHE during the mounting procedure
- lay down the PEEK body of the cell and check if two o-rings on top and two inside seal the cell
- insert the gold-plated ring electrode from above and evenly push down gently over the two inner o-rings
- insert the chess-figure like PEEK cylinder from above and push down until flush with the top of the casing
- insert the cylindric copper WE from above and follow with your sample, until flush with the top of the casing
- place the round glass plate on top and screw the gear wheel shaped lid onto the casing
- turn the cell around: place the insulating small PEEK ring onto the gold-plated ring electrode
- insert the gold-plated spring and follow with the gold-plated thermoblock, fix it with three screws (use the thinner part of the screwdriver and use light force)
- fill the syringe with *ca.* 2 ml of the desired electrolyte, turn the cell to the side to let one hole be the highest point of the cell and inject the electrolyte through the other hole (use the PEEK pin with a lateral hole as a help)
- when the cell is filled up, screw the RE in one hole and the sealing PEEK pin in the other hole to finish the assembly
- turn the cell around again, screw the gold plated contact pin laterally in the lower hole of the casing to contact with the ring electrode

The complete assembled cell now should look like in figure 4.7. Note that the sample touches the glass plate on top and that the electrolyte only forms a thin film due to capillary forces.

5 Electrochemical Etching of Au Substrates for SERS

Surface enhancement is an important and powerful tool for the investigation of thin films and kinetic surface processes. The results of the roughening process and the process itself are discussed with the help of XPS to verify the purity of gold after etching, EC to calculate the electrochemical surface area, AFM to study the average induced roughness due to surface enhancement, and UV-vis spectroscopy to find the optimal wavelength for laser excitation. Raman spectroscopy is applied on dry Au and in situ to investigate possible disturbances in the spectrum for further investigations.

5.1 Theoretical Background of Surface Enhancement

The Au blanks have been treated with an etching process to enhance the Raman signal. There are different models on the reason for signal amplification due to increased surface roughness [100, 101, 102]:

- Electromagnetic Enhancement (EM) Mechanism: Laser excited plasmon resonances of the metal produce amplification of the electromagnetic local field few nanometres above the surface.
- Charge Transfer (CT) Mechanism: Resonance effect due to the metal-adsorbate interaction; arises from electronic coupling.

Both contribute to the Raman signal while the extent of contribution is basically system dependent. A roughened surface increases the inelastic scattering of light due to the structured metal system [102].

SE in this work has been achieved during an electrochemical roughening process described in literature in ref [72] and in box 5.1. Prior to the electrochemical treatment, the substrates were mechanically polished in a figure-eight motion with Alumina MicroPolish (Buehler) of 1.00 and 0.05 µm to mirror finish on a cloth polishing pad (Buehler) [103]. After the etching, the substrates should reveal a brownish colour and a rough appearance, as it can be seen in the photography in figure 5.1.

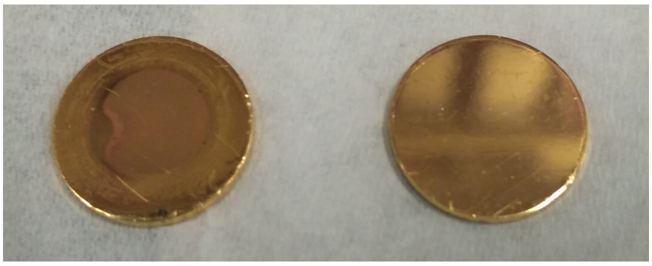

Figure 5.1: Photography of gold substrates. Polished and etched with 0.1 M KCl on the left, polished to mirror finish (0.05 µm) on the right side.

Determination of the Roughness Factor and the Electrochemical Surface Area of Gold

Different methods can be used to determine the electrochemical surface area (ECSA) of a catalyst. The method has to be applied with respect to the material. In the process of SE of Au, the roughness of the sample is increased which is shown by calculating the roughness factor (*Rf*) based on the formula

$$Rf = \frac{\text{ECSA}}{\text{Geometrical Area}} \tag{5.1}$$

The ECSA of the Au blanks is calculated by using the charge Q associated with the reduction of gold oxide. The area of the reduction peak in CV, which is proportional to the real active surface area, was integrated [104, 105, 106, 107]. Q is determined by CV in a potential range of 0 to 1.75 V *vs.* RHE with a scan rate of $50\,\text{mV}\,\text{s}^{-1}$ [72]. The charge and the ECSA are then calculated:

Box 5.1: Surface enhancement process

Herein, the surface enhancement process of Au substrates is reported, reaching an overall elevated roughness of *ca.* 44 nm along with homogeneously distributed islands with a diameter of *ca.* 400 nm.

- prepare the etching solution: mix 29 parts of millipore H_2O with 1 part 3 M KCl to receive 0.1 M KCl
- polish the Au blanks with 1.00 and 0.05 µm aluminium polish on a cloth polishing pad in a figure-eight motion; clean with millipore H_2O in between polishing steps in an ultrasonic bath
- clean in an ultrasonic bath for 5 min, dry under N_2 afterwards
- anneal in a butane flame for 1 min
- mount in a Zahner cell and fill the cell with 0.1 M KCl, calculate potential steps of the ORC for the RE
- perform 25 ORC from −0.3 to 1.2 V *vs.* SCE, hold −0.3 V *vs.* SCE for 30 s and 1.2 V *vs.* SCE for 1.3 s

$$Q = \frac{\text{Area (reduction peak)}}{\text{Scan rate}} \tag{5.2}$$

$$\text{ECSA} = \frac{Q}{390\,\mu\text{C}\,\text{cm}^{-2}} \tag{5.3}$$

The numerical value of 390 µC cm^{-2} has been suggested for polycrystalline Au in literature [107].

5.2 Investigation of the Surface Enhancement Process

For further discussion, a polished gold plate has been used as a reference and will be referred to as Au_{pol} while the gold substrate that underwent the electrochemical etching procedure will be written as Au_{etch}. Both samples were investigated with the help of XPS, EC, AFM, UV-vis, and Raman spectroscopy.

X-Ray Photoelectron Spectroscopy

After the etching process, the pureness of gold has been validated in a XP survey spectra (figure 5.2). Compared to Au_{pol}, all peaks visible can still be assigned to gold and carbon.

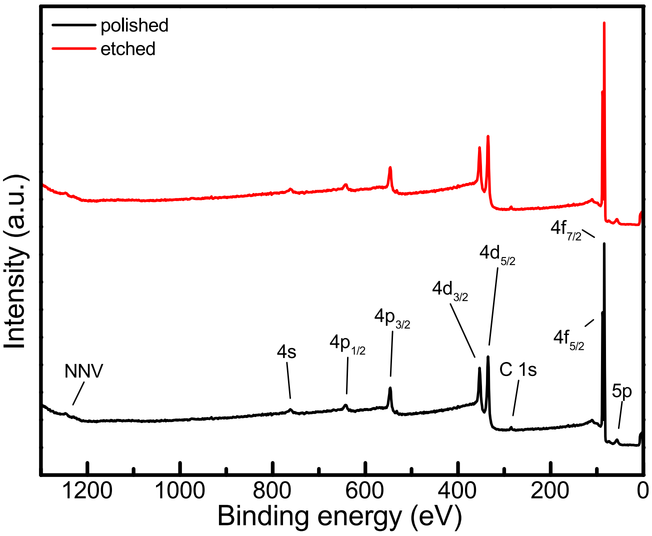

Figure 5.2: Survey spectra (XPS) of polished (black) and etched (red) Au. From left to right following gold peaks are identified: Auger peak (NNV) at *ca.* 1247 eV, 4s core level peak at *ca.* 763 eV, 4p core level peaks at *ca.* 643 and 547 eV, 4d core level peak at a*ca.* 353 eV and 335 eV, 4f core level peak at *ca.* 88 eV and 84 eV, and 5p core level peak at *ca.* 74 eV and 57 eV. Traces of carbon are detected as carbon core level peak C 1s at *ca.* 285 eV [108].

Electrochemistry

EC methods in 0.1 M KOH, uwsing Ag/AgCl as RE, have been used to characterize and compare the substrates and the changes induced with the etching process. For a first comparison regarding the increased surface area, LSV was performed as displayed in figure 5.3a.

A o-ring with a diameter of 7 mm was used, creating a geometrical surface area of *ca.* 0.385 cm^{-2}. While Au_{pol} only reaches a current density *j* of

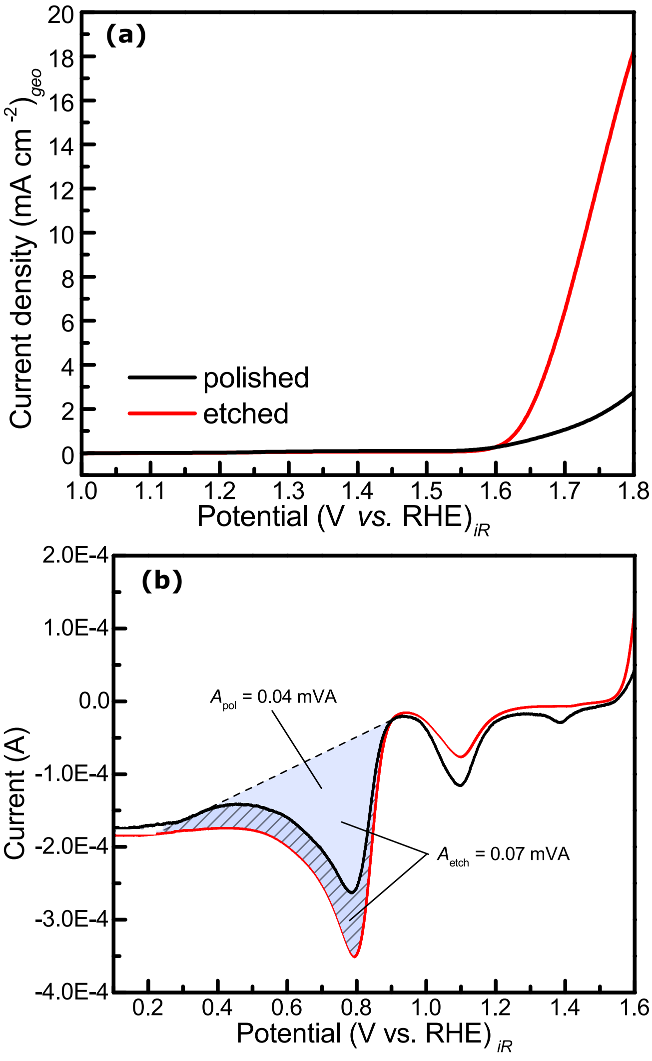

Figure 5.3: Linear sweeps of polished (black) and etched (red) Au in 0.1 M KOH depicted *vs.* the geometrical area of the sample (a); reduction cycle of Au_{pol} and Au_{etch}, performed with a scan rate of $50\,mV\,s^{-1}$ (b).

$2.8\,mA\,cm^{-2}$ at 1.8 V *vs.* RHE, the current density of Au_{etch} is around 6.5 times higher ($18.3\,mA\,cm^{-2}$) at the same potential, indicating a magnification of the exposed area.

ECSA: To approach the electrochemical surface area (ECSA), CV has been performed with a scan rate of $50\,mV\,s^{-1}$. For calculation, the reduction peak area of gold oxide was determined, which is possible due to the observation that hydrous gold oxide species form at a potential above 1.6 V *vs.* RHE and are reduced at a potential of *ca.* 0.8 V *vs.* RHE [96].

In figure 5.3b the results of the reduction path in CV are displayed. The peak between 1.0 to 1.2 V *vs.* RHE is assigned to a monolayer oxide and is not taken into account [96]. The values for the peak areas were obtained by peak integration, using a linear spline. The relevant parameters used for the calculation towards the ECSA are listed in table 5.1.

Table 5.1: ECSA calculation of gold, including the peak Area A_{peak} and the charge Q. A scan rate of $50\,mV\,s^{-1}$, a polycrystalline gold factor of $0.390\,mC\,cm^{-2}$, and a geometrical area of $0.385\,cm^2$ were used.

Sample	A_{peak} (mVA)	Q (mC)	ECSA (cm^2)	Rf
Au_{pol}	0.04	0.74	1.89	4.90
Au_{etch}	0.07	1.33	3.40	8.83

The peak area of Au_{etch} is 0.03 mVA higher than for Au_{pol}, resulting in a calculated ECSA of Au_{etch} with $3.4\,cm^2$, being therefore $1.5\,cm^2$ higher than the ECSA of Au_{pol} ($1.9\,cm^2$).

Atomic Force Microscopy

To investigate the surface roughness induced by the etching process, AFM was used. AFM surface studies were carried out using a Cypher S scanning probe microscope (Oxford Instruments, Asylum Research). Topography maps were acquired in the amplitude modulated mode using the aluminum coated cantilever Multi75Al-G (Budget Sensors). The lever sensitivity was $\sigma = 106.5\,nm\,V^{-1}$ and the force constant $k = 4.6\,N\,m^{-1}$. The cantilever was excited with a laser to tap at a frequency of $f = 77.6\,kHz$. Pictures were acquired with a scan rate of $12.5\,nm\,s^{-1}$. For analysis of the received topography results, the data processing software Gwyddion was used.

On both samples, Au_{pol} and Au_{etch}, three images on random locations were recorded, displayed in figure 5.4. An area of $100\,\mu m^2$ is projected, where one pixel in the image represents 40 nm. The resulting numerical values of the AFM studies regarding

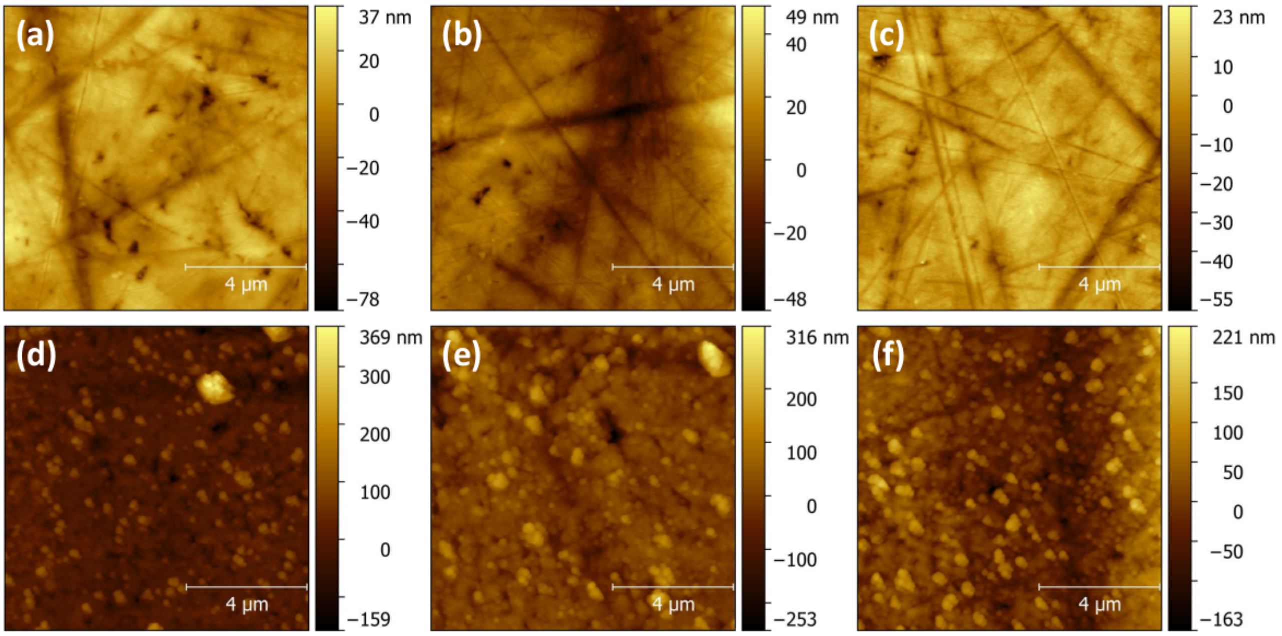

Figure 5.4: AFM images of the polished Au substrate (a–c), and the in an etching process with KCl surface enhanced Au blank (d–f). On the right side of each image, the colour scale regarding the depth of the substrate is depicted.

Table 5.2: AFM surface investigation of Au, polished to 0.05 µm (Au_{pol}) and etched with 0.1 M KCl (Au_{etch}). The average roughness R_a is calculated as root mean square (RMS) from the three R_{RMS} values obtained in each measurement (R_{RMS} for each picture in figure 5.4 is calculated by the software Gwyddion). The numbers 1 to 3 indicate the three random images taken on the surface; they correspond to (a–c) in figure 5.4 for Au_{pol} and to (d–f) for Au_{etch}.

Sample	R_a (nm)	R_{RMS} (nm)			R_{min} (nm)			R_{max} (nm)		
		1	2	3	1	2	3	1	2	3
Au_{pol}	10.53	11.75	12.23	6.86	−77.5	−48.10	−55.36	36.5	48.71	22.86
Au_{etch}	43.82	40.89	46.11	44.29	−159.3	−252.7	−163.4	368.9	315.7	220.6

the roughness investigation are tabulated in table 5.2.

The AFM images of Au_{pol} (figure 5.4a–c) show an inhomogeneous surface with scratches in a range of 48 to 78 nm in depth due to previous polishing process with aluminium paste. Since the polishing is done manually, the direction of the scratches is not uniform, and further giving rise to dark spots visible in the images corresponding to deeper structures, indicating a non-perfect abrasion. The surface is in general less uniform towards the bulk material. The sample has been used in an etching and deposition process before, so the dark spots are seen as deep pits in the Au bulk, that are not completely removed in the re-polishing process.

After the etching with 0.1 M KCl, the AFM images of Au_{etch} have a more structured appearance. Light islands indicate a more homogeneously distributed surface roughness, resulting in high contrast in the coloured image due to the distance of island and residual surface structure regarding the z-axis. The approximated diameter of these islands are in a range of 350 to 450 nm.

The RMS roughness as well as the minima and maxima values are taken directly from the software Gwyddion. The average roughness R_a then is calculated as quadratic mean from the RMS roughness of each image. The R_a of Au_{pol} (10.5 nm) can be multiplied by a factor of 4.2 towards Au_{etch} (43.8 nm) with used KCl etching process.

UV-vis spectroscopy

In order to obtain the wavelength for most effective SER scattering, the substrate is excited at its localized surface plasmon resonance peak (LSPR) which can be estimated at the absorption peak in an UV-vis measurement [109, 102]. To determine the LSRP of etched Au substrates, UV-vis reflectance spectroscopy was performed using a Lambda 900 UV/Vis/NIR spectrometer (Perkins-Elmer GmbH, Germany). Due to the nanostructure of the surface, light is scattered diffusively. This makes it hard to estimate the real absorbance of the sample. Therefore, the normalized reflectance is plotted in figure 5.5.

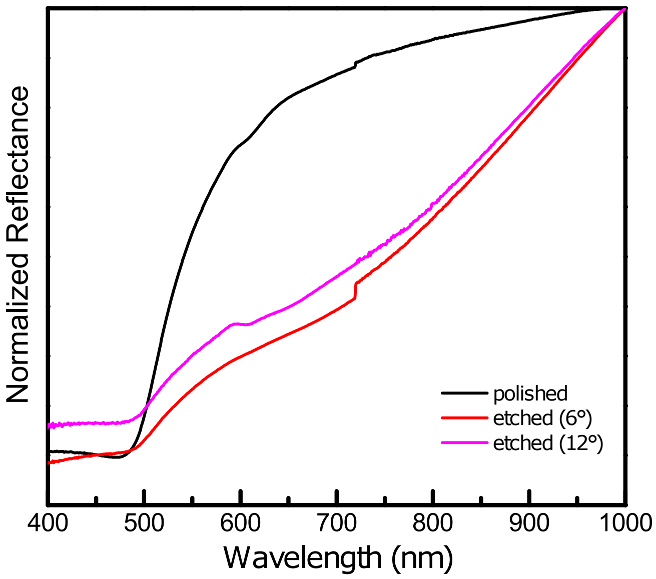

Figure 5.5: UV-vis reflectance spectrum (normalized) of polished (black) and etched (red) Au at a 6° angle as well as etched Au at a 12° angle (magenta), revealing low reflectance below ∼ 500 nm. The spectrum is displayed from 400 to 1000 nm wavelength.

All substrates show very low reflectance below a wavelength (λ) ~ 500 nm where the main LSRP of Au is suspected [110, 111]. Another absorbance feature is detected at around 600 nm that is less prominent for $\mathrm{Au_{etch}}$ measured at 6°. The absorbance A of $\mathrm{Au_{pol}}$ is approximately estimated as $A = 1 - R$ (transmittance T is neglected for the solid gold coins), where R is the reflectance, whereas $\mathrm{Au_{etch}}$ reveals diffusive scattering of the incident light due to the structured surface. This diffusive scattering is angle dependant as depicted in figure 5.5. The angle between light source and detector has been changed from 12 to 18° resulting in higher reflectance of the sample, especially for wavelengths below ~ 700 nm. During Raman spectroscopy measurements, the angle between lens and substrate can be considered 0° which seems to be suitable for the LSRP.

UV-vis spectroscopy has been used to study the properties of Au nanoparticles (AuNP) depending on their size and shape [112]. Haiss *et al.* studied AuNP sized 1.5 to 100 nm and revealed a red shift of the LSRP for bigger particles from $\lambda = 525$ to 585 nm, growing exponentially above a AuNP diameter of 25 nm [110]. Further, the growth in the intensity of the LSRP has been reported for AuNP up to 10.5 nm [113].

Based on the UV-vis data, a laser wavelength nearest to 500 nm is suggested. During experiments with a laser wavelength of 532 nm, very high fluorescence was detected on the spectrum with a signal higher than the molecule vibrations. Laser wavelength of 632.8 nm, the nearest to the second reflectance minimum in figure 5.5, gave a lot better results towards the fluorescence, as it would be expected based on the diameter of the Au particles (~ 400 nm, see figure 5.4). The low reflectance at lower wavelengths is suspected to occur mostly because of diffuse scattering of light, not due to absorbance of the Au substrate.

(*Operando*) Raman spectroscopy

All Raman spectra were acquired at a laser wavelength of 632.8 nm with an illumination time of 3 s for 20 scans. The *ex situ* spectra were recorded with a ND filter of D 0.6 while the *operando* spectra required a higher laser power, adjusted with ND filter of D 0.3.

The results of dry $\mathrm{Au_{pol}}$ and $\mathrm{Au_{etch}}$ are compared in figure 5.6 a. $\mathrm{Au_{pol}}$ under irradiation exhibits no peak due to the unoriented structure. $\mathrm{Au_{etch}}$ shows

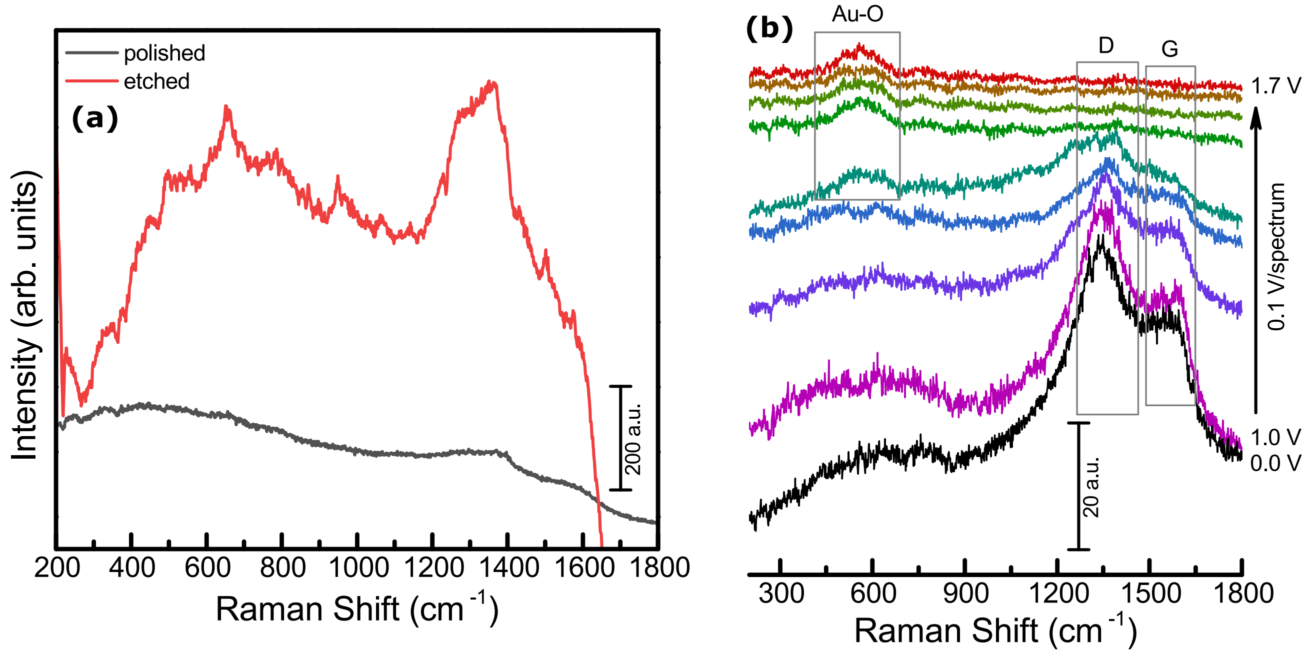

Figure 5.6: SER spectra of Au_{pol} (black) and Au_{etch} (red), excited with a laser wavelength of 633 nm (a); *operando* spectra with visible formation of Au−O and vanishing of D and G bands of adsorbed carbon.

higher intensity for the same laser power and illumination time as well as a stronger BG signal. The SER spectrum might be misleading, since it also enhances spectral artefacts that may not be molecular vibrations, so peaks have to be assigned more carefully. However, the intensity of these artefacts is quite low compared to the real signal that is achieved by a film deposited on Au_{etch}. The overlapping broad bands between 1200 to 1400 cm^{-1} are assigned to adsorbed carbon [114]. The peak at 633 cm^{-1} is associated with a weak Au−O stretching mode, originating from adsorbed oxygen, as it ia similarly found on roughened silver electrodes [115, 116].

Raman spectroscopy has been conducted *operando* with Au_{etch} as WE in 0.1 M KOH in a potential range of 1.0 to 1.7 V *vs.* RHE. The SER spectra were recorded in 0.1 V steps and are stacked in figure **??** to reveal the change of the surface species during OER. At 0 to 1.0 V *vs.* RHE the substrate has a Raman signal similar to the dry sample in figure 5.6b with Raman bands at 1347 and 1538 cm^{-1} corresponding to the D and G band of (adsorbed) carbon [117]. Until 1.3 V *vs.* RHE these features blue-shift towards 1388 and 1590 cm^{-1}, and are not detectable in the spectrum at 1.4 V *vs.* RHE anymore.

At the same potential, the peak attributed to the Au−O stretching mode (ν(Au−O)) at 574 cm^{-1} is observed [118, 73]. This vibrational mode has been found at 580 cm^{-1} for a Au−O bond by high-resolution electron energy loss spectroscopy (HREELS) [119]. According to the Pourbaix diagram of Au, above 1.0 V *vs.* RHE and for a pH value of 12.88 for 0.1 M KOH, Au(OH)_3 should be formed which was found at 635 to 677 cm^{-1} in literature, or as an Au–OH stretching mode at *ca.* 425 cm^{-1} [120, 118, 121]. This feature is not clearly detected during the OER of Au in this work. In literature, a peak at 815–830 cm^{-1} has been attributed to the ν(O−O) vibration in Au–OOH [118, 115]. Since this band is known to be weak in 0.1 M KOH and occur more prominent in acids, it is not detected here compared to the weak intensity signal of ν(Au−O). An improvement regarding the spectrum was not achieved with higher laser power or longer irradiation time.

6 Investigation of Nickel Oxide

In this chapter, reactively magnetron sputtered NiO_x *is investigated, deposited on different substrates at temperatures of RT to 600 °C. The goal was to gain insght into the substrate and temperature dependence of* NiO_x *as electrocatalyst towards the OER. The chemical composition is investigated by in line XPS, revealing deficient* NiO_x *species,vanishing at higher temperature depositions. In EC, these deficient structures seem to support the catalytic activity of* NiO_x *by the means of overpotentials and charge storage ability, as investigated by capacitance measurements. XPS of the cycled samples exhibits higher conversion of NiO to* $Ni(OH)_2$ *during cycling in 0.1 M KOH for defect-containing* NiO_x*. Operando Raman spectroscopy is used to investigate the surface species and intermediates of* NiO_x *in alkaline environment to understand the difference in catalytic activity due to the defect-free structure of high temperature deposited* NiO_x*.*

6.1 Photoelectron Spectroscopy of NiO_x

To determine the chemical composition of NiO_x in regard to the deposition temperature T_{dep}, XP spectra were recorded on Au_{pol} in line after the sputtering process. The survey spectra of these measurements are displayed in figure 6.1.

All peaks in the survey are assigned to either nickel, oxygen, or gold. Compared to the Au spectrum in figure 5.2, the most prominent gold core level peak Au 4f has low intensity, but is still visible under the NiO_x layer along with a weak gold core level peak Au 4d.

Most information regarding the composition of NiO_x is found in the nickel core level peak Ni $2p_{3/2}$ and oxygen core level peak O 1s. Detail spectra of these regions were recorded and are displayed in figure 6.2. All spectra were corrected with a Shirley background (BG) before fitting.

O 1s: The O 1s region was fitted with Gaussian-Lorentzian (GL) curves. For NiO_{Au}^{RT} (figure 6.2b), three components are assigned. One for oxygen induced defects or vacancies (O_V) and two for O^{2-} lattice oxygen bound to NiO_x (O_L–Ni^{II}/O_L–Ni^{III}). The NiO_x components are associated with *ca.* 63 % NiO (Ni^{II}) at 529.2 eV (lit.: 529.4 to 529.9 eV) and *ca.* 15 % Ni_2O_3 (Ni^{III}) at 530.7 eV (lit.: 530.9 to 531.7 eV), respectively [123, 124]. The need for a third peak to describe the O 1s region of NiO_x has been reported before [125]. The oxygen found in this region at 532.0 eV has been attributed to deficient, interstitial, and peroxo-like species (531.1 to 531.9 eV) with a concentration of *ca.* 22 % [125, 126, 127]. The overlap with O_L–Ni^{III} makes this region difficult to fully understand. The higher FWHM of O_L–Ni^{III} of 1.6 eV in contrast to 1.1 eV for O_L–Ni^{II} has been reported and is associated with oxygen-rich nickel oxide species [124].

For NiO_{Au}^{600} (figure 6.2d) only two components are necessary to describe the O 1s region. These are associated with *ca.* 94 % O_L–Ni^{II} at 529.4 eV and small amounts of *ca.* 6 % O_L–Ni^{III} at 531.6 eV. This peak is not only associated with O_L–Ni^{III} but also with small amounts of O_V due to the peak shift to higher E_{BE}, and in accordance to the defect free Ni $2p_{3/2}$ region in figure 6.2c.

Ni $2p_{3/2}$: The difficult to analyse Ni 2p region was fitted with a line shape derived by single crystalline NiO [122]. Since for a GL peak fit of the Ni $2p_{3/2}$ region, a total amount of six to seven peaks are necessary [128], to which the oxidation state of Ni can not clearly be assigned, the envelope of Uhlenbrock *et al.* [122] is used for deconvolution. A perfect NiO surface exhibits a characteristic low binding energy peak (LBEP) in the region of 853.4 to 854.4 eV, but also reveals a shoulder at 855.6 eV in the high binding energy peak (HBEP) which over-

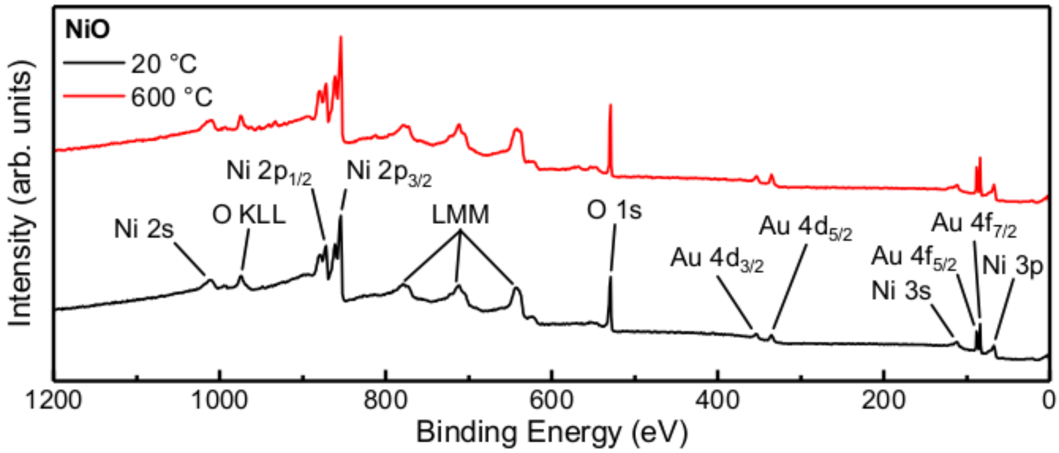

Figure 6.1: Survey of NiO_x deposited at RT and 600 °C. From left to right following peaks can be identified: nickel core level peak Ni 2s at *ca.* 1009 eV, oxygen Auger peaks O KLL at *ca.* 1013, 999, and 978 eV, nickel core level Ni 2p peak at *ca.* 870 and 853 eV, nickel Auger peaks Ni LMM at *ca.* 778, 772, and 712 eV, oxygen core level peak O 1s at *ca.* 531 eV, gold core level peaks Au 4d at *ca.* 353 and 335 eV, nickel core level peak Ni 3s at *ca.* 111 eV, gold core level peaks Au 4f at *ca.* 88 and 84 eV, and nickel core level peak Ni 3p at *ca.* 67 eV [108].

laps with the region of $Ni(OH)_2$ and $Ni(CO)_3$ at 855.1 to 855.6 eV [124, 125].

Comparing the Ni $2p_{3/2}$ region of NiO^{RT}_{Au} and NiO^{600}_{Au}, the line fit derived from single crystalline NiO fits perfectly for NiO^{600}_{Au}, while NiO^{RT}_{Au} exhibits a second region which was also fitted creating a line shape attributed to deficient species, mainly Ni^{III}. The HBEP is suspected to contain most of the Ni^{III} species. Since this peak is more intense in NiO^{RT}_{Au}, this observation is in accordance to the higher O_L–Ni^{III} content in the O 1s region. The deficient region is suspected to contain also Ni induced vacancies, defects, and NiO_x species oxidized other than Ni^{II}/Ni^{III} (Ni_{def}). Based on the XPS evaluation, NiO^{RT}_{Au} contains *ca.* 13 % defective Ni species. Thus, not all Ni^{III} is taken into account by the Ni^{III}/Ni_{def} region due to the visible O_L–Ni^{III} peak in the 600 °C sample. The decrease of Ni^{III} content in NiO_x with increased T treatment has been reported, along with higher oxidized NiO_x species as well as decrease of chemisorbed O^{2-}/O_V at temperatures above 400 °C [125, 129].

Substrate dependence: Although only NiO_x on Au_{pol} has been discussed in this chapter, NiO_x was also investigated on other substrates relevant such as SS/Au, Ni, and p^+ doped Si. The defect states of NiO_x were observed on all other materials which is why they are not further discussed in this work. Also the deposition on Au_{etch} has been investigated, with no visible differences in the spectra. In fact, the growth of NiO_x seems to be independent of the substrate. A special focus will always rely on Au, since it is used for surface enhancement and operando Raman spectroscopy.

Temperature dependence: To gain deeper knowledge about how the different species in NiO_x vary with the deposition temperature T_{dep}, reactive magnetron sputtered samples have been analysed with XPS also for 200 and 400 °C.

Figure 6.3a and b show the XP detail spectra of NiO_x recorded in line on Au_{pol} for temperatures of RT, 200, 400, and 600 °C. In figure 6.3a, the Ni $2p_{3/2}$ region is displayed and the previously discussed characteristic line shape of NiO_x is observed. The LBEP of Ni $2p_{3/2}$ has been attributed to oxidative Ni^{II} species, whereas the HBEP contains Ni^{III} as well as Ni_{def}. With increasing T_{dep}, the ratio of these two peaks changes towards lower amounts of Ni^{III} and Ni_{def}. This is peculiar observable in the O 1s region, as it is tabulated in table 6.1.

This observation is consistent with the line fits in figure 6.2a as it shows absence of deficient Ni

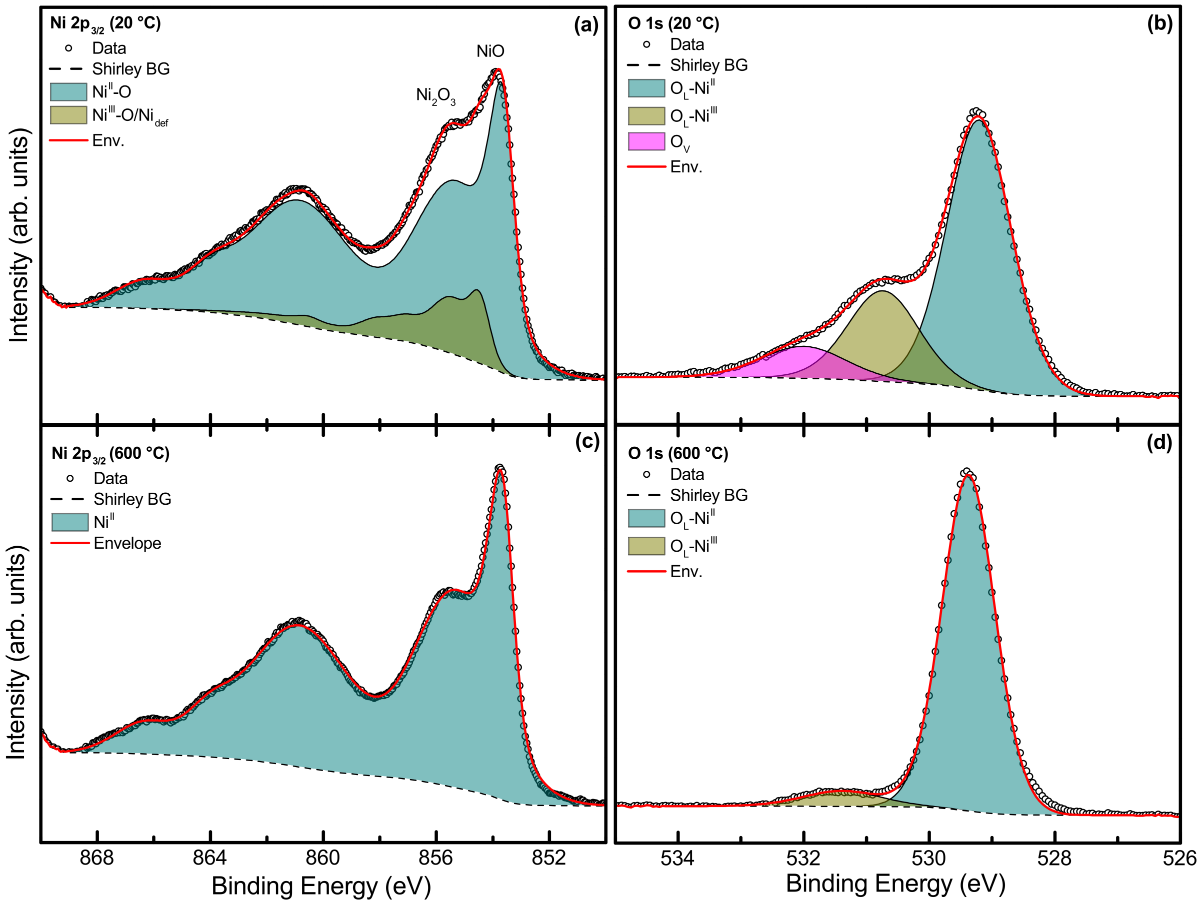

Figure 6.2: Detail spectra (XPS) of NiO_x, nickel core level peak Ni $2p_{3/2}$ for NiO^{RT}_{Au} (a) and NiO^{600}_{Au} (c) and oxygen core level peak O 1s for NiO^{RT}_{Au} (b) and NiO^{600}_{Au} (d). Deposition at RT (a–b) and 600 °C (c–d) is investigated. The peaks were corrected with a Shirley background. O 1s spectra are deconvoluted by Gaussian curves; Ni $2p_{3/2}$ regions are fitted with a single crystal NiO line shape [122].

Table 6.1: Deconvolution of the oxygen species in the O 1s region of NiO_x.

	Concentration (at-%)		
Sample	O_L–Ni^{II}	O_L–Ni^{III}	O_V
NiO^{RT}_{Au}	63.43	14.82	21.75
NiO^{200}_{Au}	78.56	12.82	8.63
NiO^{400}_{Au}	92.18	7.01	0.81
NiO^{600}_{Au}	94.41	5.59	–

species at $T_{dep} = 600\,°C$. The same trend is observable in the O 1s region in figure 6.3b, where the amount of O_L–Ni^{III} and O_V decreases with increasing T_{dep}.

6.2 Electrochemistry of NiO_x

Current-voltage curves were measured with a scan rate of $10\,mV\,s^{-1}$, using 0.1 M KOH as electrolyte and Ag/AgCl as RE. The data was *iR*-corrected by electrochemical impedance spectroscopy, as described in section 4.6.

OER Activity

Linear sweeps (LS) of the samples are displayed in figure 6.4 with a potential window relevant to the OER. For data evaluation, the second of three sweeps after 1 h of CA at 1.52 V *vs.* RHE is taken into account. The kinetic parameters are summarized in table 6.2. For reasonable comparison, the overpotential η has been determined at a current density $j = 10\,mA\,cm^{-2}$.

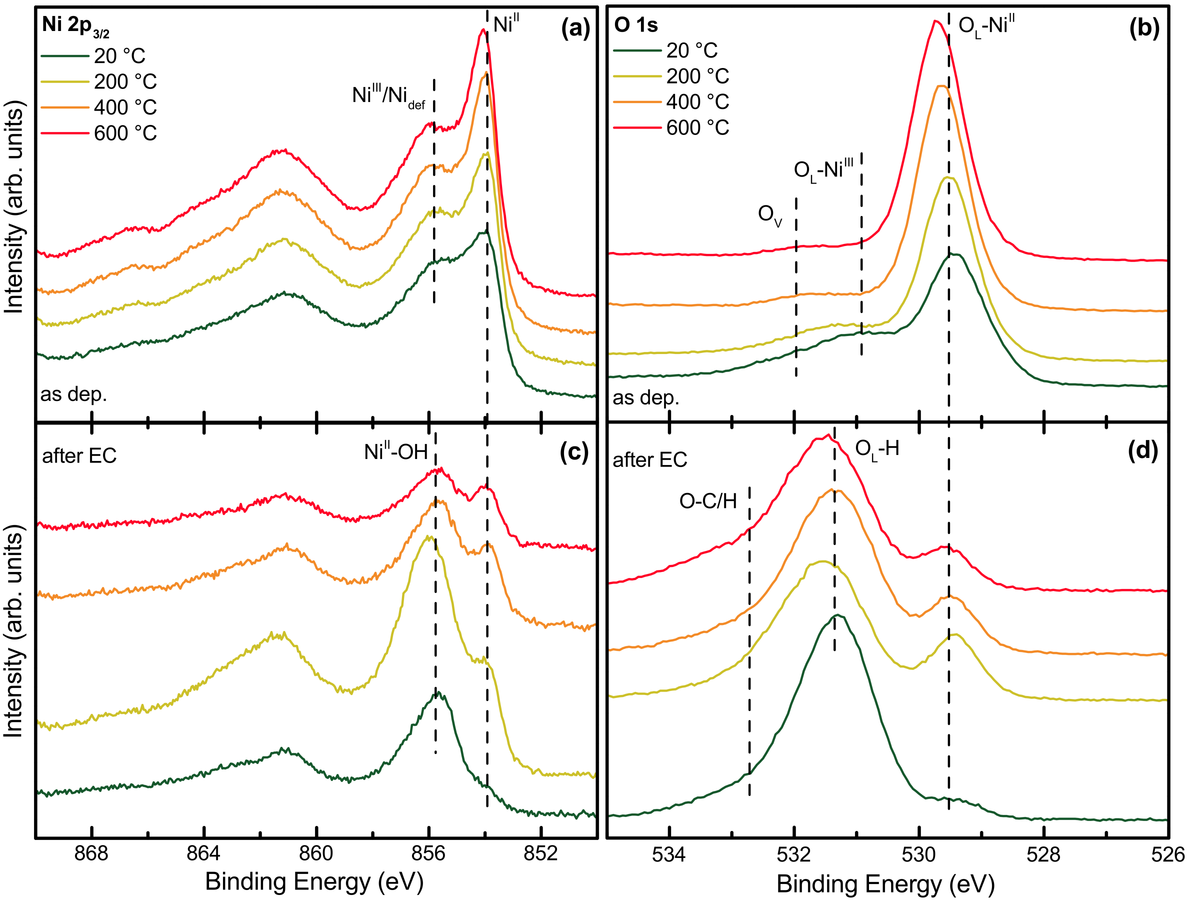

Figure 6.3: Detail spectra (XPS) of NiO_x core level peaks Ni $2p_{3/2}$ and O 1s, as deposited (a, b) and after EC (c, d). Deposition at RT, 200, 400, and 600 °C is investigated. The BE positions of the different surface species are indicated by a gray dashed line.

The LS in figure 6.4a show a typical behaviour for NiO_x. All samples feature a cathodic current peak at 1.41 to 1.48 V *vs.* RHE corresponding to the oxidation of $Ni(OH)_2$ to NiOOH, involving the intercalation/deintercalation of protons followed by a current due to O_2 evolution [130, 131]. For $NiO^{RT}_{SS/Au}$ and NiO^{RT}_{Au} the oxidation wave is observed at lower potentials E in contrast to all 600 °C samples. Further, the oxidation waves of NiO^{600}_{Ni}, $NiO^{600}_{SS/Au}$, and NiO^{600}_{Au} reach currents lower around a factor of 10 compared to NiO^{RT}_{Au}, indicating a lower rate of conversion towards the NiOOH. Furthermore, the current-potential response of the catalyst changes from battery behaviour to capacity behaviour [131]. NiO^{RT}_{Ni} reveals a broad oxidation wave directly merging into the area of O_2 evolution, suggesting sluggish kinetics even at low scan rates.

The activity comparison was conducted by comparing the overpotential η ($\eta = E_{RHE} - 1.23\,V$) at a given current density of 10 mA cm^{-2}. The baseline sample NiO^{RT}_{Ni} reveals η values of 400 mV, increasing to 430 mV by changing the deposition temperature T_{dep} to 600 °C. NiO_x on Au has η values of 390 and 410 mV for RT and 600 °C. The η of $NiO^{RT}_{SS/Au}$ is 370 mV, rising to 400 mV at a deposition at 600 °C. The Tafel slopes (figure 6.4b) are determined as well, revealing similar values of 50, 42, and 46 mV dec^{-1} for NiO_x on Ni, SS/Au, and Au, decreasing at $T_{dep} = 600$ °C to 37, 36, and 37 mV dec^{-1}.

Substrate dependence: $NiO^{RT}_{SS/Au}$ is the most active catalyst after deposition at RT (370 mV). NiO^{RT}_{Au} and NiO^{RT}_{Ni} reach $j = 10$ mA cm^{-2} at η values 20 and 30 mV higher. Comparing the activity at elevated T during the deposition, $NiO^{600}_{SS/Au}$ has a 10

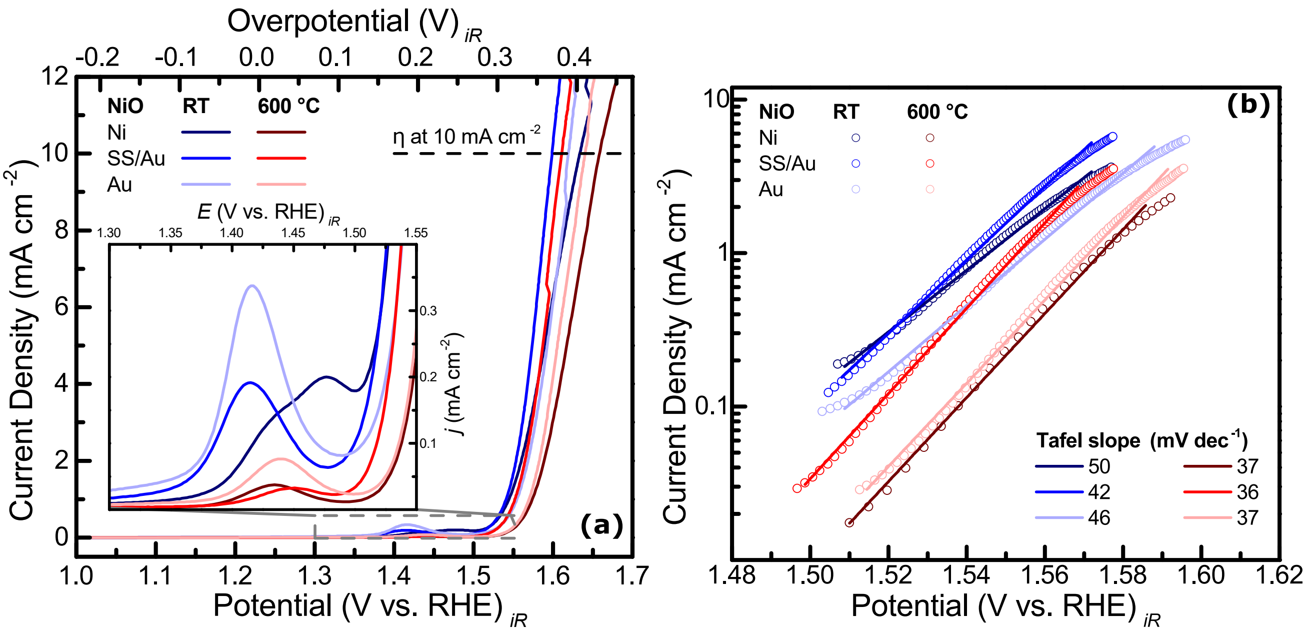

Figure 6.4: Activity comparison of NiO_x deposited at RT and 600 °C. NiO_x was deposited and measured on Ni foil, Au coated SS, and Au blanks. (a) Linear sweeps were recorded in 0.1 M KOH vs. Ag/AgCl with a scan rate of $10\,mV\,s^{-1}$, displayed from 1.0 to 1.7 V *vs.* RHE. The black dashed line indicates the overpotential at $10\,mA\,cm^{-2}$. The inset plot shows the typical oxidation wave of NiO. (b) Tafel plots are displayed in a potential range of 1.48 to 1.62 V *vs.* RHE; the Tafel slopes are determined *via* a linear fit of the current-voltage curves at a logarithmic current density axis.

Table 6.2: Kinetic parameters towards the OER for NiO_x on different substrates, magnetron-sputtered at varying temperatures T. Results were obtained from current-voltage curves (LSV) with $10\,mV\,s^{-1}$ in 0.1 M KOH. The received overpotential η at $10\,mA\,cm^{-2}$, the Tafel slope, and the anodic charge transfer coefficient α_a are given.

Substrate	T (°C)	η at $10\,mA\,cm^{-2}$ (mV)	Tafel slope ($mV\,dec^{-1}$)	α_a
Ni foil	RT	400±4	50±0.2	0.502
	600	430±2	37±0.4	0.684
SS/Au	RT	370±1	42±0.2	0.519
	600	400±4	36±0.1	0.695
Au	RT	390±1	46±0.4	0.539
	600	410±1	37±0.2	0.678

and 30 mV lower η than NiO_{Au}^{RT} and NiO_{Ni}^{RT}, respectively. Therefore, an increase in the activity due to lower η values is observed for NiO_x that has been deposited on Au or a gold-supported substrate such as SS. The increase due to gold-support is associated with a charge transfer from Ni cations to highly electronegative Au atoms [73, 132].

While NiO_{Ni}^{RT} exhibits a referential Tafel slope of $50\,mV\,dec^{-1}$, this is lowered by gold-support to $46\,mV\,dec^{-1}$, and further to $42\,mV\,dec^{-1}$ by using gold-coated SS as a substrate. Corrigan [133] investigated the Tafel slopes of electrodeposited hydrous nickel oxide electrodes in dependence of the iron content in 5.5 M KOH, obtaining a Tafel slope of $72\,mV\,dec^{-1}$ for rigorously Fe free electrolyte. 1 M KOH was estimated to contain ≤0.66 ppm (*ca.* 0.0001 %) Fe by Klaus *et al.* [134], observing Tafel slopes of 45 to $55\,mV\,dec^{-1}$ in their unpurified electrolyte for electrodeposited $Ni(OH)_2$ electrocatalysts. In contrast, Corrigan [133] reported a Tafel slope of $70\,mV\,dec^{-1}$ for same impurity value.

Temperature dependence: All samples revealed a lower η for the defect-containing depositions at RT. The temperature dependence of a catalyst is evaluated based on the difference of η observed after RT and 600 °C deposition on the same sample. Due to this assumption, NiO_x on Ni foil and gold-coated SS have a similar temperature dependence of 30 mV, that is slightly lowered to 20 mV by using only Au as a substrate.

The Tafel slopes are lowered in defect-free NiO_x samples by 13, 12, and 9 mV dec^{-1} for NiO_x on Ni, SS/Au, and Au, to similar values of 36 to 37 mV dec^{-1}. The catalytic activity of NiO_x at higher current densities is increased with a defect-free surface. As a consequence, defects at the surface are suspected to assist during the adsorption of hydroxides and formation of intermediates such as oxyhydroxides at lower E. At increased E, however, their positive influence on the activity is lowered, and is even suspected to hinder desorption processes that are needed to free catalytically active sites for further OER. Studying the turnover frequency (TOF) of NiO_x with regard to the T_{dep} is helpful to further investigate this phenomenon.

Activity over time: The activity over cyclation time was studied, exemplified for NiO_{Au}^{RT} and NiO_{Au}^{600}. As explained in section 4.6, CA was applied at 1.52 V *vs.* RHE, first for 900 s and later again for 3600 s (4500 s in total). LSV curves with 10 mV s^{-1} were recorded in a potential range of 1 to 2 V *vs.* RHE before, between, and after the CA steps.

The results are displayed in figure 6.5 with an inset plot revealing the typical Ni^{II}/Ni^{III} oxidation wave of $Ni(OH)_2/NiOOH$. For both NiO_{Au}^{RT} and NiO_{Au}^{600} a decrease in η is stated. While NiO_{Au}^{RT} before CA reveals an overpotential of 500 mV at $j = 10\,\mathrm{mA\,cm^{-2}}$, it decreases to 430 mV (−70 mV) after 900 s and 390 mV (−110 mV) after 4500 s. Even though $E = 1.52\,\mathrm{V}$ *vs.* RHE is hold much longer after the first CA step, η only decreases 40 mV more. NiO_{Au}^{600} does not reach $j = 10\,\mathrm{mA\,cm^{-2}}$ at an applied voltage of 2 V *vs.* RHE, but exhibits η of 470 mV after 900 s CA, decreasing further to 410 mV.

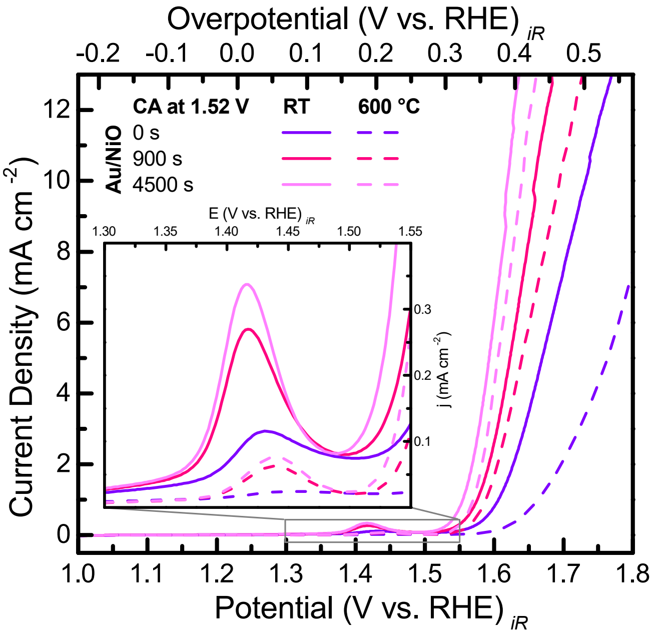

Figure 6.5: Activity comparison of NiO_{Au}^{RT} (solid lines) and NiO_{Au}^{600} (dashed lines). LSV curves were recorded in 0.1 M KOH *vs.* Ag/AgCl with a scan rate of 10 mV s^{-1} in a potential range of 1 to 2 V *vs.* RHE, before CA at 1.52 V *vs.* RHE (violet), after 900 s (pink), and after 4500 s in total (light magenta). The inset plot displays the typical oxidation wave of NiO_x between 1.30 to 1.55 V *vs.* RHE.

The increase of activity over time is addressed to the Ni^{II}/Ni^{III} oxidation visible in the inset plot in figure 6.5, since it correlates directly with η at $j = 10\,\mathrm{mA\,cm^{-2}}$. Over time, the oxidation wave grows, revealing higher j and shifts towards lower E, resulting in higher formation of Ni^{III} species, that are suspected to be active in the O_2 evolution. At first, a major part of NiO_x is converted to $Ni(OH)_2$, resulting in a high η decrease with relatively low CA time. Due to the lower drop of η later, bulk material is suspected to be converted slower due to diffusive hindrance of the needed hydroxide species provided by the KOH electrolyte.

Resistance of NiO_x

To address the varying activity of NiO_x in regard to T_{dep}, impedance spectroscopy (IS) measurements have been carried out by Jieun Kim in the context of an advanced research lab (ARL). NiO_x was deposited on p^+-Si and Au by sputtering according to the recipe described in section 4.4. The layer thickness was determined to 4.6 and 9 nm for a 9 min deposition at RT and 600 °C. IS measurements revealed a growing resistance by increasing T_{dep} and the layer thickness. However, on Au the resistance was independent on these parameters, resulting in 0.50 to 1.1 W for $\mathrm{NiO}_{\mathrm{Au}}^{\mathrm{RT}}$ and 0.55 to 0.60 W for $\mathrm{NiO}_{\mathrm{Au}}^{600}$.

By applying IS measurements to the samples used in this thesis, the influence of the electrical resistance on the catalytic activity of NiO_x on Au was disproved. Therefore, the observed disparity in EC must arise due to another reason.

6.3 Chemical Composition after EC

Another XP spectrum has been recorded for both $\mathrm{NiO}_{\mathrm{Au}}^{\mathrm{RT}}$ and $\mathrm{NiO}_{\mathrm{Au}}^{600}$ after EC, from which the nickel core level peak Ni $2p_{3/2}$ and the oxygen core level peak O 1s are depicted in figure 6.6.

Ni 2p: The Ni $2p_{3/2}$ peak was deconvoluted with the two known line shapes for single-crystalline NiO and $\mathrm{Ni}^{\mathrm{III}}/\mathrm{Ni}_{\mathrm{def}}$ as well as a new line shape for $\mathrm{Ni(OH)_2}$. In RT NiO_x, *ca.* 76 % of NiO_x species are converted into $\mathrm{Ni(OH)_2}$ during cycling. Additionally, only a small amount of $\mathrm{Ni}^{\mathrm{III}}/\mathrm{Ni}_{\mathrm{def}}$ of *ca.* 3 % is present on the surface. In contrast, only 44 % of NiO_x in 600 °C NiO_x is converted into $\mathrm{Ni(OH)_2}$. The conversion ratio of $\mathrm{Ni}^{\mathrm{II}}$ plus deficient NiO_x species to $\mathrm{Ni(OH)_2}$ is around three times higher at a T_{dep} of RT.

O 1s: Regarding the peak fitting of the O 1s region, several restrictions were made. The peak maximum for known components was kept at the same E_{BE} compared to the fit before EC with a tolerance of ±0.2 eV. The FWHM of the components was only allowed to change ±0.4 eV. Four components are found to be present on the surface of the RT sample. Residual O^{2-} in Ni−O−Ni ($\mathrm{O}_{\mathrm{L}}^{\mathrm{EC}}$–$\mathrm{Ni}^{\mathrm{III}}$) is located at 529.4 eV and oxygen induced defective species $\mathrm{O}_{\mathrm{V}}^{\mathrm{EC}}$ are located at 531.8 eV. Low amounts of O^{2-} corresponding to $\mathrm{Ni_2O_3}$ are present at 530.9 eV, based on which a conversion rate of 72 % is stated. The main peak at 531.4 eV is attributed to metal hydroxide Ni−O−H ($\mathrm{O}_{\mathrm{L}}^{\mathrm{EC}}$–H) species in $\mathrm{Ni(OH)_2}$. In a broad peak with a FWHM of 2.4 eV, residual oxygen species O–C/H such as C–O and intercalated $\mathrm{H_2O}$ are summed up. It is further not distinguished between the C–O bondings, but due to the additional peak and the shape in the core level region C 1s, C–O, adsorbed C–C, and C=O bondings are suspected. The atomic concentration of the displayed samples is found in table 6.3.

Table 6.3: Atomic concentration of oxygen species in NiO_x after EC.

	Concentration (at-%)				
Sample	$\mathrm{O_L}$–$\mathrm{Ni}^{\mathrm{II}}$	$\mathrm{O_L}$–$\mathrm{Ni}^{\mathrm{III}}$	$\mathrm{O_L}$–H	$\mathrm{O_V}$	O–C/H
$\mathrm{NiO}_{\mathrm{Au}}^{\mathrm{RT}}$	9.77	3.62	57.16	1.56	27.88
$\mathrm{NiO}_{\mathrm{Au}}^{600}$	34.86	–	57.82	–	7.32

Owing the observation that NiO_x species are converted into $\mathrm{Ni(OH)_2}$ over cycling, defective species seem to assist greatly in this process since the conversion rate is much higher for RT NiO_x. Both $\mathrm{Ni}^{\mathrm{II}}/\mathrm{Ni}^{\mathrm{III}}$ and $\mathrm{Ni}_{\mathrm{def}}$ species are converted over time. $\mathrm{O_V}$ give rise to the formation of $\mathrm{Ni(OH)_2}$ and react with hydrogen to intercalate water in the surface pores. The $\mathrm{O_L}$ species are overall considered less reactive, since not only less $\mathrm{Ni(OH)_2}$ but also lower amounts of O–C/H are formed on a defect-free surface. This is assisted due to the vanishing of $\mathrm{Ni}^{\mathrm{III}}$ species in 600 °C NiO_x.

Temperature dependence: In figure 6.3c and d, NiO_x on Au has been investigated for RT, 200, 400, and 600 °C after EC again. A trend established in previous deconvolution is visible. The ratio between the NiO_x region and the $\mathrm{Ni(OH)_2}$ in core level peak Ni $2p_{3/2}$ shrinks at elevated T_{dep} due to the lower NiO to $\mathrm{Ni(OH)_2}$ conversion. A similar behaviour is observed in the O 1s region regarding the ratio of $\mathrm{O}_{\mathrm{L}}^{\mathrm{EC}}$–$\mathrm{Ni}^{\mathrm{II}}$ and metal hydroxides $\mathrm{O_L}$–H.

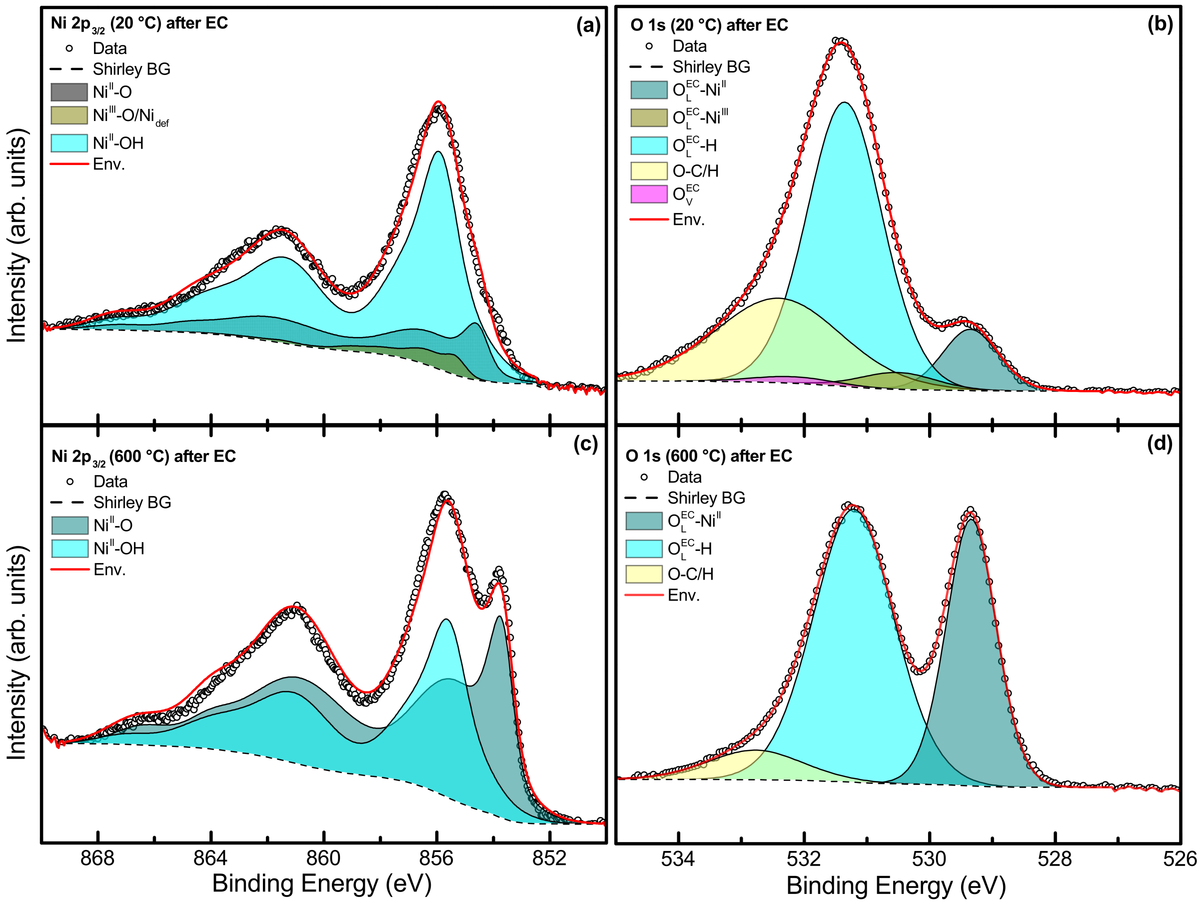

Figure 6.6: Detail spectra (XPS) of NiO_x, nickel core level peak Ni $2p_{3/2}$ for NiO_{Au}^{RT} (a) and NiO_{Au}^{600} (c) and oxygen core level peak O 1s for NiO_{Au}^{RT} (b) and NiO_{Au}^{600} (d) O 1s after EC. Both samples NiO_{Au}^{RT} and NiO_{Au}^{600} have been investigated. The peaks were corrected with a Shirley BG and the spectra are deconvoluted by GL curves.

6.4 Capacitance of NiO_x

The electrochemical double layer capacitance (EDLC) has been evaluated in a region, where conversion from $Ni(OH)_2$ to NiOOH as a faradaic process is avoided to guarantee capacity behaviour of the catalyst [131]. The results of this approximation are depicted in figure 6.7 and an example of the CV data is displayed in figure 6.7a, given for a scan rate of 100 mV s^{-1} after 4500 s of CA at 1.52 V *vs.* RHE. CV curves were measured in a potential range of 1.02 to 1.12 V *vs.* RHE with scan rates of 10 to 250 mV s^{-1}.

For evaluation, the current I of the 5th cycle at a potential of 1.07 V *vs.* RHE is taken into account and plotted against the corresponding scan rate (see dashed line in figure 6.7a). The I values are fitted linearly to determine the double layer capacitance C_{dl} as the slope of the linear fit. Whereas the curves in figure 6.7a are all relatively symmetric about the zero point of the I axis ($\sim$ 0.004 mA), the absolute current response is temperature dependent. For instance, the curves of the 600 °C samples exhibit low slopes over the potential range where in contrast the RT samples show increased I at $E = 1.12$ V *vs.* RHE of $\sim$ 0.023 mA. An ideal capacitor would reveal a potential-independent current [131].

In figure 6.7b the EDLC is measured directly after performing three LS for surface conditioning. For comparison of a change in C_{dl}, CV curves were again recorded after several LS and in total 4500 s of CA at 1.52 V *vs.* RHE. C_{dl} for RT depositions ranges from 117 to 174 µF and for 600 °C deposition from 28 to 49 µF. The obtained C_{dl} describes the capacitance with respect to the measured area of $\sim 0.385\,\mathrm{cm}^2$. For further evaluation, the specific C_{dl} is given as $\mu\mathrm{F\,cm}^{-2}$.

The intrinsic C_{dl} values at both temperatures are given in table 6.4. At RT, gold-support of $\mathrm{NiO_x}$ lowers the C_{dl} slightly by $-16\,\mu\mathrm{F\,cm}^{-2}$, while the use of gold-supported SS strongly enhances the C_{dl} by $132\,\mu\mathrm{F\,cm}^{-2}$. For the 600 °C samples, an increase for both gold-support ($+57\,\mu\mathrm{F\,cm}^{-2}$) and SS/Au ($+39\,\mu\mathrm{F\,cm}^{-2}$) is observed.

In earlier XPS investigation, the deficient nature of $\mathrm{NiO_x}$ at RT was observed (see figure 6.2). As a more stoichiometric, single-crystalline like structure has further been observed in XPS for $T_{\mathrm{dep}} = 600\,°\mathrm{C}$, this defect healing effect was also proven by Nam *et al.* with EXAFS [135]. They further correlated the pseudo-capacitance of $\mathrm{NiO_x}$ to its deficient structure and reported a higher specific capacitance for defect rich $\mathrm{NiO_x}$ as it was discussed here. Even if the mass of the catalyst has not been investigated in this study, the difference in capacitance for RT and 600 °C is mostly correlated to the defects observed in XPS.

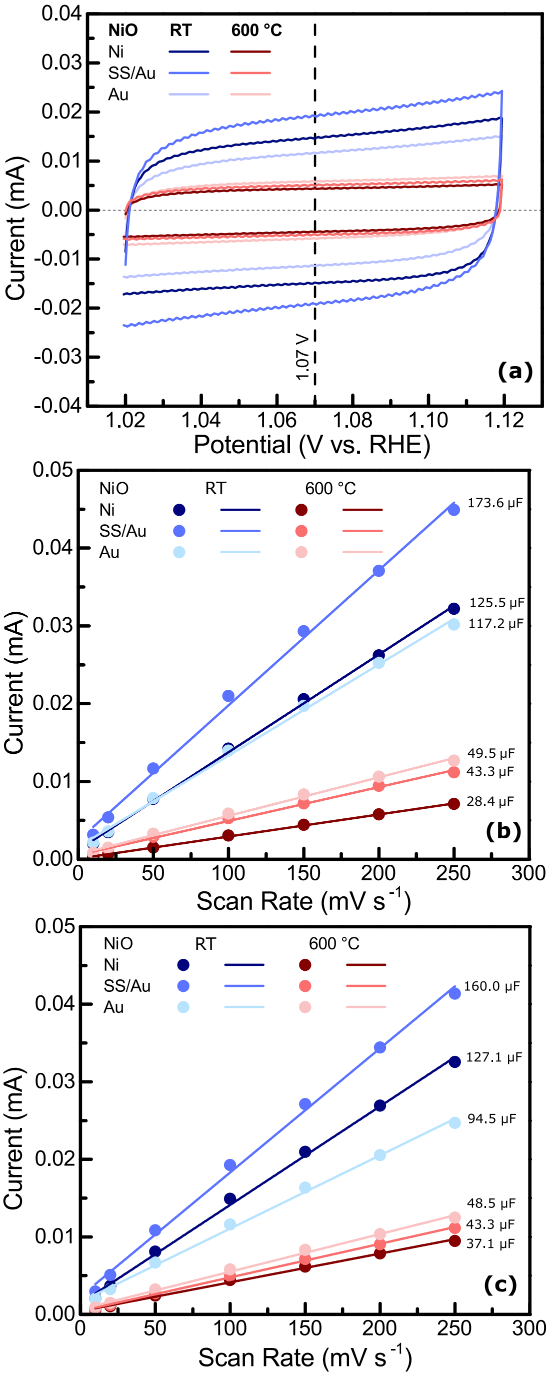

Figure 6.7: Electrochemical double layer capacitance (EDLC) of $\mathrm{NiO_x}$ on different substrates at deposition temperatures of RT and 600 °C. (a) CV curves from 1.02 to 1.12 V *vs.* RHE with $100\,\mathrm{mV\,s}^{-1}$ in 0.1 M KOH, recorded after 4500 s CA at 1.52 V *vs.* RHE. A value of 1.07 V *vs.* RHE is indicated by a vertical dashed line. Analysis based on CV curves at different scan rates (b) at the start of electrochemical measurements and (c) after 4500 s of CA at 1.52 V *vs.* RHE. The double layer capacitance C_{dl} is approximated with a linear fit in the oxidation region of the CV curves given in µF.

Table 6.4: Intrinsic double layer capacitance C_{dl} of $\mathrm{NiO_x}$ in $\mu\mathrm{F\,cm}^{-2}$ at the start of the EC procedure ($C_{\mathrm{dl}}{}^1$) and after 4500 s of CA at 1.52 V *vs.* RHE, for RT and 600 °C.

	Intrinsic EDLC ($\mu\mathrm{F\,cm}^{-2}$)			
	RT		600 °C	
Sample	$C_{\mathrm{dl}}(1)$	$C_{\mathrm{dl}}(2)$	$C_{\mathrm{dl}}(1)$	$C_{\mathrm{dl}}(2)$
$\mathrm{NiO_{Ni}}$	320	330	73	96
$\mathrm{NiO_{SS/Au}}$	452	416	112	112
$\mathrm{NiO_{Au}}$	304	247	130	127

The temperature and substrate trends stated before in the C_{dl} are still visible after 4500 s of CA at 1.52 V *vs.* RHE (figure 6.7c). All values are listed in table 6.4. An ideal approach is the evaluation of the EDLC data as specific capacitance, as the mass of the catalyst varies with T_{dep} due to the layer thickness. However, it is noted that the capacity-temperature dependence of $\mathrm{NiO_x}$ has been investigated before and a decrease in C_{dl} has been associated with the amount of NiO and $Ni(OH)_2$ of the material [131]. Srinivasan and Weidner [131] proclaimed a higher C_{dl} for less $Ni(OH)_2$ containing NiO_x due to increased adsorption of hydroxyl ions, which is their believed mechanism of charge storage. However, at temperatures above 300 °C, the C_{dl} decreases due to a decrease in the Brunauer-Emmett-Teller (BET) surface area and intrinsic capacitance.

As it is proven by XPS after EC, the conversion rate of $NiO/Ni(OH)_2$ differs with T_{dep}, resulting in higher amounts of $Ni(OH)_2$ for defect-rich structures after the same cycling time. The change in C_{dl} over time is therefore addressed to the $NiO/Ni(OH)_2$ conversion during cycling and CA at 1.52 V *vs.* RHE.

Defect-induced pseudocapacitance

To gain deeper insight into the temperature/defect dependece of NiO_x on Au regarding the EDLC, reactively magnetron sputtered films at $T_{dep} = 200$ and 400 °C have also been investigated. The results of this measurements are depicted in figure 6.8.

Evaluation of figure 6.8a reveals that the C_{dl} from oxidation and reduction differs in a range of 0.1 to 0.9 µF. Also after 4500 s of CA at 1.52 V *vs.* RHE the difference of the redox C_{dl} is 0.9 µF at the maximum. In this regime, for oxidation and reduction, C_{dl} is seen as equal and the root mean square (RMS) of both values used. The results are tabulated in table 6.5.

A trend of the EDLC regarding the temperature is observed. Before/after cycling, C_{dl} of NiO_x decreases steadily with T_{dep}. The decrease in C_{dl} is correlated to the amount of defective species on the surface that also decreases with higher T_{dep}. Another trend is observed with the influence of the cycling time on the catalysts. The lower T_{dep}, the higher the change of C_{dl} over time. NiO_{Au}^{RT} decreases over the CA duration about $-60\,\mu F\,cm^{-2}$, NiO_{Au}^{200} around $-26\,\mu F\,cm^{-2}$, and for NiO_{Au}^{400} and NiO_{Au}^{600} only a slight drop of −6 and $-3\,\mu F\,cm^{-2}$ is visible. This phenomena has been attributed to the formation of $Ni(OH)_2$ before which is lower for NiO_x at increased T_{dep}. This is in accordance to previous observations regarding the oxidation wave discussed before (depicted in figure 6.5). The most accurate description is the vanishing of previously accessible defective sites on the surface that are either filled by intercalated H_2O or O_{ads} species, or are converted into $Ni(OH)_2$ during cycling.

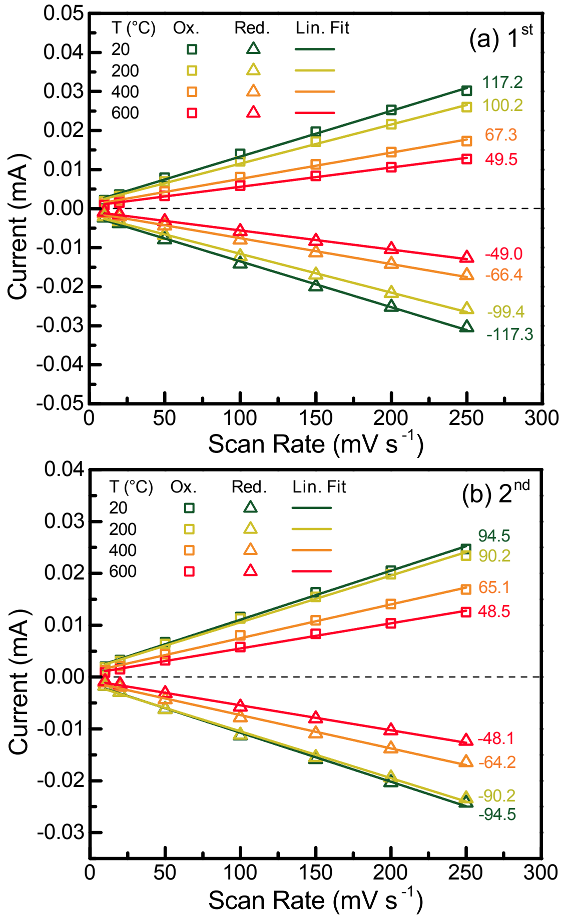

Figure 6.8: Electrochemical double layer capacitance (EDLC) of NiO_x on Au at deposition temperatures of RT, 200, 400, and 600 °C. Analysis based on CV at different scan rates (a) at the start of electrochemical measurements and (b) after 4500 s of CA at 1.52 V *vs.* RHE. The capacitance is approximated with a linear fit of the oxidation/reduction values and written inside the graph in µF.

An increase in T_{dep} further results in the decrease of the intrinsic capacitance, that is known to correspond to the electrochemical surface area of the catalyst [131]. The mechanism of charge storage in $Ni(OH)_2$ is the intercalation of H^+, whereas for

Table 6.5: Intrinsic double layer capacitance C_{dl} of NiO_x on Au in μF cm^{-2} at the start of the EC procedure ($C_{dl}{}^1$) and after 4500 s of CA at 1.52 V *vs.* RHE, for RT, 200, 400 and 600 °C.

	Intrinsic EDLC (μF cm^{-2})	
Sample	$C_{dl}(1)$	$C_{dl}(2)$
NiO_{Au}^{RT}	304	247
NiO_{Au}^{200}	260	234
NiO_{Au}^{400}	174	169
NiO_{Au}^{600}	127	125

NiO_x adsorption, and reaction of OH^- on the surface is involved. The difference in C_{dl} is therefore attributed to bulk material being involved in the reaction of $Ni(OH)_2$ which is less possible for the bigger OH^- molecules [136]. This explanation is conclusive with the XPS investigation (figure 6.6), where the amount of $Ni(OH)_2$ on the surface drastically differs for samples deposited at RT and 600 °C over cycling.

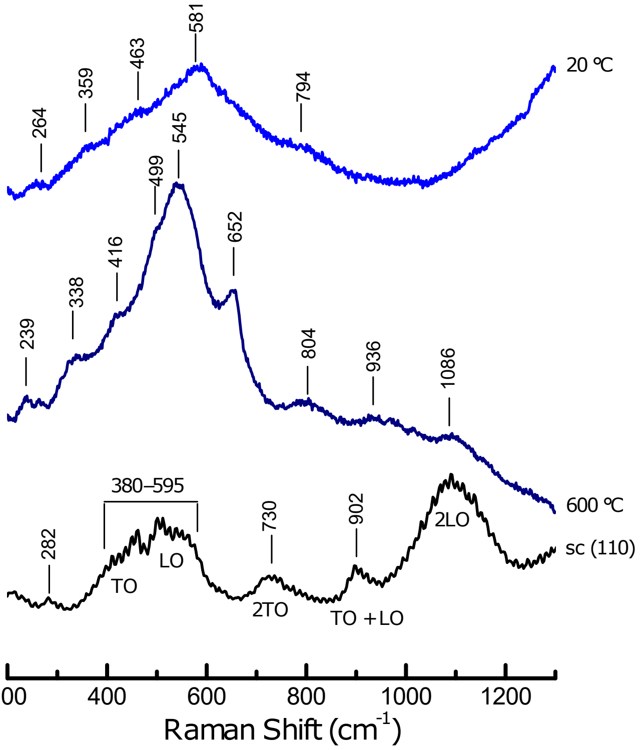

Figure 6.9: Raman spectra of single crystalline (110) NiO (black), NiO_x deposited at 600 (navy) and RT (blue) in a wavenumber range of 200 to 1300 cm^{-1}. The vibrational modes of the single-crystal are attributed to the corresponding bands: 1P TO (380 to 440 cm^{-1}), 1P LO (560 to 595 cm^{-1}), 2P 2TO (730 cm^{-1}), 2P TO + LO (902 cm^{-1}), and 2P 2LO (1100 cm^{-1}).

6.5 Raman Spectroscopy of NiO_x

Reactive magnetron sputtered NiO_x on roughened Au substrates have been studied in Raman spectroscopy. Figure 6.9 shows the Raman spectra of the as deposited samples at RT and 600 °C in comparison to a NiO single crystal with (110) orientation, measured in a range of 200 to 1300 cm^{-1}.

According to previous investigations, the Raman scattering in NiO originates from a one-phonon (1P) transverse optical (TO) mode at 380 to 440 cm^{-1}, and a 1P longitudinal optical (LO) mode at 560 to 595 cm^{-1}. Three peaks at 730, 902, and 1100 cm^{-1} were assigned to the two-phonon (2P) scattering (2TO, TO + LO, 2LO) [137, 138, 139]. The feature at 282 cm^{-1} is not assigned to a special mode but reoccurs in NiO_{Au}^{600} at 239 cm^{-1} and in NiO_{Au}^{RT} at 264 cm^{-1}. It is also suspected with very low intensity in the Au substrate in figure **??**, therefore it is associated with ν(M−M) vibrations such as ν(Au−Au) (lit.: 79 to 165 cm^{-1}) [140] or ν(Ni−Ni). In literature, ν(M−M) vibration for solid compounds such as Sn, Hg, Mn, and Cd show stretching at 157 to 208 cm^{-1} [141]. The vibration could be assigned to ν(M–M) in deficient Ni_2O_3, as it does appear in non-single metal oxides such as Fe_2O_3 [142, 143]. Since the Au vibrations at this frequency range are of rather low intensity, the vibrational bands can also be assigned to ν(Ni−O) stretching vibrations as they occur in complex Ni and oxide containing compounds [140].

Comparing the single crystal data with the sputtered NiO_x samples, the characteristic Raman peaks shrink or vanish due to the amorphous surface layers in accordance to in literature investigated annealed NiO_x powders [144]. In NiO_{Au}^{600}, two 2P modes reveal a blue-shift towards 804 cm^{-1}

(2TO) and 936 cm^{-1} (TO + LO), whereas the 2LO mode shifts towards slightly lower wavenumbers (1086 cm^{-1}). The 1P band is known as an indicator for the quality of single crystals and becomes more pronounced in powders due to the presence of defects and surface effects which can also be observed for sputtered films here [138]. In contrast to the suggestion by the XPS data of NiO_{Au}^{600}, the high temperature NiO_x is not revealing a defect-free structure, since they are still present in the strong 1P band. As the whole spectrum reveals a blue-shift, the sharp peak at 652 cm^{-1} is associated with the 1LO mode of Ni−O which overlaps with the dominant 1TO mode. This mode exhibits strong background signals at 338, 416, 499 cm^{-1} and a maximum at 545 cm^{-1} which are estimated to be more pronounced due to the surface enhancement process.

Raman spectrum of NiO_{Au}^{RT} exhibits a broad peak between 360 to 720 cm^{-1} attributed to the overlap of the 1TO and 1LO optical modes in NiO at 794 cm^{-1}, a weak peak arises due to the blue shifted 2TO mode of Ni−O [145]. Similar background signal as in NiO_{Au}^{600} is observed at 369 and 463 cm^{-1}. The comparison of the positions of these bands further strengthen the assumption of spectral artefacts due to surface enhancement.

6.6 *Operando* Raman spectroscopy of NiO_x

NiO_x thin film electrocatalysts have been studied under working condition in 0.1 M KOH electrolyte with Raman spectroscopy. The samples were mounted in the Raman cell (figure 4.7) and installed firmly under the microscope, after being connected to the GAMRY potentiostat. The freshly prepared films on Au_{etch} were first cycled 30 times in a potential range of 1.0 to 1.5 V *vs.* RHE in the Raman cell to condition the surface. Afterwards, a potential of 1.0 V *vs.* RHE was applied for 10 min to stabilize the catalyst and its surface processes. In the following process, potential steps of 0.05 V towards 1.65 V *vs.* RHE have been carried out. The respective potential was held for at least 1 min in a chronamperometric measurement while the current was monitored to measure stable intermediates on the surface.

Raman spectra were acquired with a laser power of 3 mW, attenuated by ND filters, and an illumination time of 3 s in a wavenumber range of 200 to 1400 cm^{-1}. The spectrum was accumulated 20 times to reduce noise and enhance the signal to noise ratio.

NiO_x deposited at RT

Figure 6.10a displays the SER spectrum of the *in situ* measurement for NiO_{Au}^{RT}. Below a potential of 1.4 V *vs.* RHE, two bands are visible in the spectrum which are assigned to the combined 1P 1TO and 1LO mode at 598 cm^{-1} in NiO and the A_{1g} stretching mode of Ni^{II}–O in $Ni(OH)_2$ at 503 cm^{-1} [72]. For pure $Ni(OH)_2$, a wavenumber region of 445 to 460 cm^{-1} has been reported for the Ni^{II}–O stretching mode [70, 146], but this peak has found to be very sensitive to defective structures and shows a blue-shift up to 534 cm^{-1} [147]. The A_{1g} stretching mode of Ni−OH in $Ni(OH)_2$ at lower wavenumbers has been reported but was not directly observed as an own peak in this case, probably due to the low Raman scattering cross-section of this species [73]. This feature is exceptionally weak for α-$Ni(OH)_2$ which is probably the present species on the catalyst, recalling that β-$Ni(OH)_2$ requires altering of the film for several days [148]. Several possible configurations of adsorbates and intermediates for metal oxides are displayed in figure 6.11.

Above a potential of 1.4 V *vs.* RHE new peaks arise in the spectrum at 486 cm^{-1} and 563 cm^{-1}, that are both attributed to the formation of NiOOH due to the oxidation of $Ni(OH)_2$. The peaks are assigned to the e_g bending vibration (486 cm^{-1}) and the A_{1g} stretching vibration (563 cm^{-1}) mode of Ni^{III}–O in NiOOH. These peaks are very intense compared to the low intensity vibrations of NiO and $Ni(OH)_2$, which is associated with a resonance enhancing effect in NiOOH [72, 73]. Under the

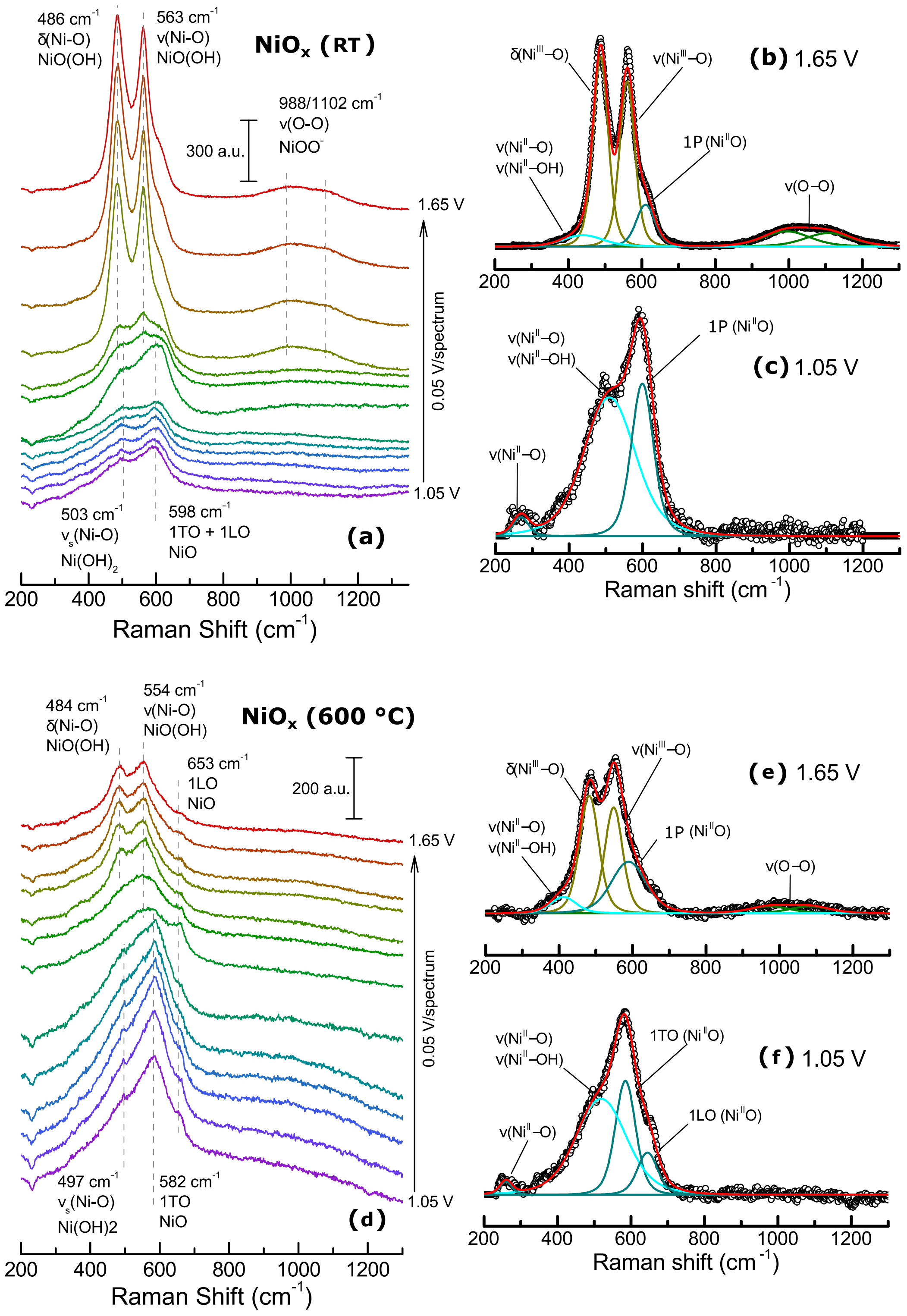

Figure 6.10: Stacked SER spectra of NiO$^{RT}_{Au}$ (a) and NiO$^{600}_{Au}$ (d) obtained at constant potentials from 1.05 to 1.65 V *vs.* RHE. The different graphs are stacked from the bottom to the top and the observed vibrations are assigned to the corresponding wavenumbers as well as the active species in the structure. Deconvoluted SER spectra of obtained at constant potentials of 1.05 V (b,e) and 1.65 V (c,f) *vs.* RHE. The graphs are fitted with a linear spline and Lorentzian curves between 200 to 1300 cm^{-1}. Oxide species are displayed in dark cyan, hydroxides in cyan, oxyhydroxides in dark yellow, and superoxide species in olive.

stretching mode of Ni^{III}–O, a shoulder is visible that is attributed to the previously described combined 1P mode of NiO that does not vanish in the process of oxidation.

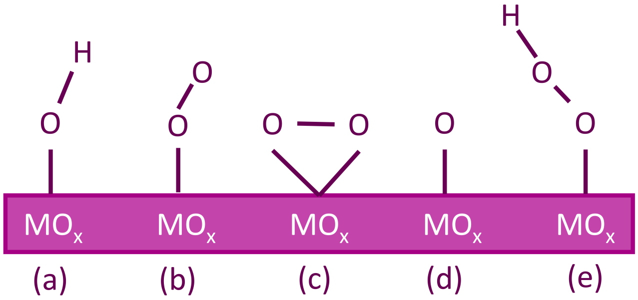

Figure 6.11: Adsorbed oxide and hydroxide intermediates on metal oxide (MO_x) surfaces. The figure illustrates M–OH (a), M–O_2 in end-on configuration (b), M–O_2 in side-on configuration (c), M–O (d), and M–OOH (e).

Starting at a potential of *ca.* 1.5 V *vs.* RHE, two bands in a region of 900 to 1200 cm^{-1} appear in the spectrum. The superoxo (O–O) vibration in the deprotonated $NiOO^-$ occurs at 988 and 1079 cm^{-1} and has been investigated in detail by Diaz-Morales *et al.* [72]. They performed Raman measurements of electrodeposited $Ni(OH)_2$ in $H_2{}^{18}O$ to observe a peak shift of this wavenumber region compared to $H_2{}^{16}O$. This method is based on Zhang *et al.* [62] who attributed a shifting peak in this region to the active oxygen species CoOO during the photocatalytic water oxidation on Co_3O_4. Further, Diaz-Morales *et al.* [72] reported two different O–O vibration modes in a region of 900 to 1150 cm^{-1} for NiO_2 species. This peak splitting occurs for superoxo structures, where the O_2^- is bound to a metal atom in line, corresponding to the side-on configuration in figure 6.11 [140]. It is also possible but unlikely for this vibration to be part of a Ni=O vibration of NiOOH, since these species occur at wavenumbers of 900 to 1000 cm^{-1} [140].

The SER spectra at 1.05 V and 1.65 V *vs.* RHE have been fitted to obtain all surface species detected with Raman spectroscopy. The data was corrected by a linear spline and deconvoluted with Lorentzian curves, the result being depicted in figure 6.10b and c. Deconvolution reveals the overlap of the two $Ni(OH)_2$ stretching modes ν(Ni^{II}–O) and ν(Ni^{II}–OH) at 1.05 V *vs.* RHE with a peak maximum at 510 cm^{-1}. The 1TO mode of NiO might contribute to the peak but is hard to deconvolute separately. The 1LO and ν(Ni^{II}–O) stretching mode of NiO is located at 599 cm^{-1}, and 269 cm^{-1}, respectively. The ratio of NiO to $Ni(OH)_2$ is *ca.* 1:2. At 1.65 V *vs.* RHE, the ν(Ni^{II}–O) in NiO is not visible any more, whereas the bending and stretching mode of Ni^{III}–O in NiOOH appear dominantly at 488 and 560 cm^{-1}, accompanied by the double O–O band of $NiOO^-$ at 994 and 1108 cm^{-1}.

NiO_x deposited at 600 °C

In figure 6.10d the SER spectra of NiO_x deposited at 600 °C are displayed. The spectra were achieved in the same manner as for NiO_{Au}^{RT}. Up to 1.35 V *vs.* RHE three overlapping bands between 375 to 650 cm^{-1} are visible in the spectrum. Two of them are assigned to the 1P 1TO + 1LO mode at 582 cm^{-1} and 2P 2TO mode at 653 cm^{-1} in NiO. The peak at 497 cm^{-1} arises from the A_{1g} stretching mode of Ni^{II}–O in $Ni(OH)_2$. At a potential of 1.35 V *vs.* RHE at 554 cm^{-1} a peak corresponding to the A_{1g} stretching vibration mode of Ni^{III}–O in NiOOH grows and reaches its full form at a potential above 1.45 V *vs.* RHE where the 1P mode of NiO can not be fully determined any more. At this potential, also the e_g bending vibration at 484 cm^{-1} of Ni^{III}–O in NiOOH arises. Over the whole potential range, the 1LO mode at 653 cm^{-1} is visible.

The SER spectra of NiO_{Au}^{600} show several differences towards the previously discussed SER spectra of NiO_{Au}^{RT}. In figure 6.10b and c, no 2P mode of NiO has been detected. The intensity of the 1P mode of NiO (582 cm^{-1}) is high compared to the vibrational modes of Ni^{III}–O in NiOOH which is probably due to the more crystalline structure of the deposited NiO_x and the low amount of $Ni(OH)_2$ formation as it already has been observed in XPS (figure 6.6). The 1P mode in NiO_{Au}^{600} red-shifts 16 cm^{-1}, and the

A_{1g} stretching mode of Ni^{II}–O in $Ni(OH)_2$ 6 cm^{-1} towards lower wavenumbers.

The $Ni(OH)_2$/NiOOH redox transition shows its distinct two peaks at a later potential of 1.45 V *vs.* RHE on NiO^{600}_{Au}. Both peaks greatly overlap with the high Raman scattering cross-section 1P mode of NiO, which makes it hard to compare the relative intensities of the samples. For wavenumbers above 660 cm^{-1}, no Raman bands are detected on first glance.

In figure 6.10e and f, the deconvoluted spectra of NiO^{600}_{Au} at 1.05 and 1.65 V *vs.* RHE are displayed. The BG was subtracted with a linear spline and the peaks fitted with Lorentzian curves between 200 to 1300 cm^{-1}. At 1.05 V *vs.* RHE, the combined 1TO/1LO and the $\nu(Ni^{II}$–$O)$ stretching mode of NiO are centered at 584/645 and 260 cm^{-1} with the overlapped $\nu(Ni^{II}$–$O)$ and $\nu(Ni^{II}$–$OH)$ stretching modes of $Ni(OH)_2$ in between. The ratio of NiO to $Ni(OH)_2$ was calculated to 1.6:1, revealing 3 times less formation of $Ni(OH)_2$ compared to NiO^{RT}_{Au}.

At 1.65 V *vs.* RHE, the bending and stretching mode of Ni^{III}–O in NiOOH appear at 482 and 549 cm^{-1}, accompanied by a smaller double O−O band of $NiOO^-$ at 947 and 1082 cm^{-1} as well as a 1P mode of NiO at 589 cm^{-1}. Compared to NiO^{RT}_{Au}, all peaks reveal a red-shift. The conversion of Ni^{III} to Ni^{IV} was estimated as a ratio of the double O−O band area of $NiOO^-$ and the $\nu(Ni^{III}$–$O)$ mode of NiOOH in NiO^{RT}_{Au} at 1.65 V *vs.* RHE and vice versa for NiO^{600}_{Au}. The formation of the deprotonated $NiOO^-$ in intensity is *ca.* 10 times higher in NiO^{RT}_{Au}, correlating to the observation of the lower activity in NiO^{600}_{Au}, as Ni^{IV} is presumably the active species in OER.

Kinetic description

The process of water oxidation on NiO_x has been studied intensely and this work forther investigated the redox system in alkaline media, based on which a scheme is introduced in figure 6.12. During contact with the electrolyte, the deposited NiO_x forms $Ni(OH)_2$ (Ni^{II}) which is further oxidized to NiOOH (Ni^{III}), occuring under the formation of a deprotonated species $NiOO^-$ (Ni^{IV}). The idea of a deprotonated NiO^- species assisting in water oxidation has been introduced, but was not further proven [72]. In this case, the vibration for this species can not be distinguished from the 1P mode in NiO, appearing as a shoulder at 598 cm^{-1}.

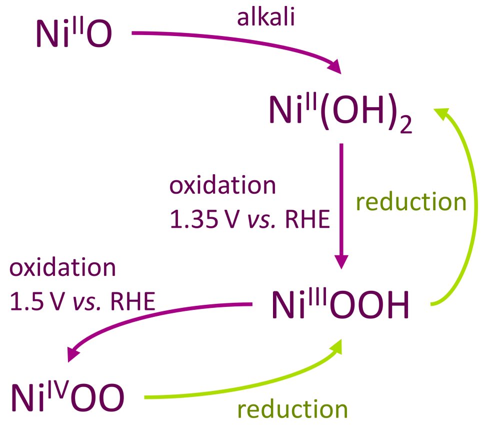

Figure 6.12: Scheme of redox processes of thin film NiO_x in alkaline media.

Either way, the O_2 formation is highly suspected to occur *via* decomposition of negatively charged surface oxide $O_{ads}{}^-$ or negatively charged superoxide $O_{2,ads}{}^-$ species [72]. The final mechanism remains unclear, if deprotonation gives rise to $O_{ads}{}^-$ and further forms the O−O bond or deprotonation of OOH_{ads} results in $NiOO^-$. It is not unreasonable for a combination of both mechanisms to take place on the surface of NiO_x.

Most of the available literature suggests the coverage of NiO_x (Ni^{II}) electrodes with $Ni(OH)_2$ (Ni^{III}) when in contact with alkaline electrolyte and further the oxidation towards Ni^{III} as in NiOOH [149]. The presence of Ni^{IV} at higher potentials as active centres towards the OER has been suggested by some authors as well based on the observed Tafel slopes [150, 149, 73].

7 Investigation of Manganese Oxide

Manganese oxide was introduced as a promising electrode material for the OER, that is of current interest for catalysis research. In this chapter, MnO_x has been synthesized in three different oxidation states, as proven wit XPS, and evaluated based on its catalytic activity. During operando Raman spectroscopy, δ-MnO_2 was present on all samples, but differed in its degree of charging, i.e. interlayer spacing and presence of Mn^{III}/Mn^{IV} cations. The cyclation duration and activation of each catalyst was able to alter the activity greatly, which will be of further interest towards dynamic investigations.

7.1 Photoelectron Spectroscopy of MnO_x

Determination of the chemical composition of sputtered MnO_x (procedure according to section 4.5) was conducted by recording XP spectra on Au_{etch} substrates in line after deposition. The growth of MnO_x was also monitored on Au_{pol} and no difference regarding the chemical composition was observed. Since the sputtering process is highly directional, not the complete surface of Au_{etch} may be covered with MnO_x. Recalling, the R_a after etching was investigated with AFM and found to be *ca.* 44 nm (see figure 5.4 and table 5.2 for comparison), compared to a layer thickness of *ca.* 10 nm. To avoid subjection to X-ray spot location, better comparison is achieved by presenting MnO_x on Au_{pol}. Au_{pol} covered entirely with MnO_x was used in EC for better evaluation of the surface area, while Au_{etch} was needed for SER measurements.

The survey spectra of MnO_x are displayed in figure 7.1. All peaks visible are assigned to manganese, oxygen, and gold. The most prominent region of Au in figure 5.2, core level peaks Au $4f_{5/2}$ and Au $4f_{7/2}$, overlap directly with the multiplet of manganese core level peak Mn 3s. Gold core level peaks Au $4d_{3/2}$ and Au $4d_{5/2}$ are still visible in the spectra underneath the MnO_x layer, especially on Mn^{III} which is suspected to possess a lower thickness due to the annealing step. The difficult to determine oxidation state of Mn with XPS is highly debated in literature. Therefore, one of the most common approaches is used, determining the E_{BE} distances in the Mn 2p and Mn 3s regions. This is especially difficult for Mn on Au due to the overlap of intense features. More information regarding the chemical composition is delivered by the O 1s region, and lastly the Mn 3p region for stoichiometry evaluation.

Mn 2p: The main phase of MnO_x is determined with manganese core level peak Mn 2p by the E_{BE} difference $\Delta E 2p_{1/2}$ between the Mn $2p_{1/2}$ peak and the Mn $2p_{1/2}$ shake-up satellite. The high resolution spectra of the Mn 2p region and the respective peak positions are displayed in figure 7.2.

The Mn $2p_{3/2}$ peak is hard to deconvolute, since in most available literature such as Ilton *et al.* [151] or Biesinger *et al.* [152], six to eight peaks are used for data fitting without clear assignment of an oxidation state therein. Even for powders of 99 % purity, the peak area is not deconvoluted with less Gaussian-Lorentzian peak fits. Therefore, the $\Delta E 2p_{1/2}$ is used as an indicator for the main phase in the Mn 2p region based on the work of Gorlin and Jaramillo [153], who used the work of Di Castro and Polzonetti [154] (care for the wrong reference in the Gorlin paper, where Matsumoto *et al.* [155] is cited) as reference. In Mn^{II}, the lowest $\Delta E 2p_{1/2}$ is calculated to 6.5 eV (lit.: 5.4 to 6.0 eV), whereas higher values are found for Mn^{III} with 9.8 eV (lit.: 10 to 10.5 eV), and 11.8 eV in Mn^{IV} (lit.: 11.8 to 11.9 eV). Table 7.1 lists these values compared to the literature data. The discrepancy of the $\Delta E 2p_{1/2}$ values is associated with the purity of the synthesized MnO_x phase, matching perfectly in Mn^{IV} but

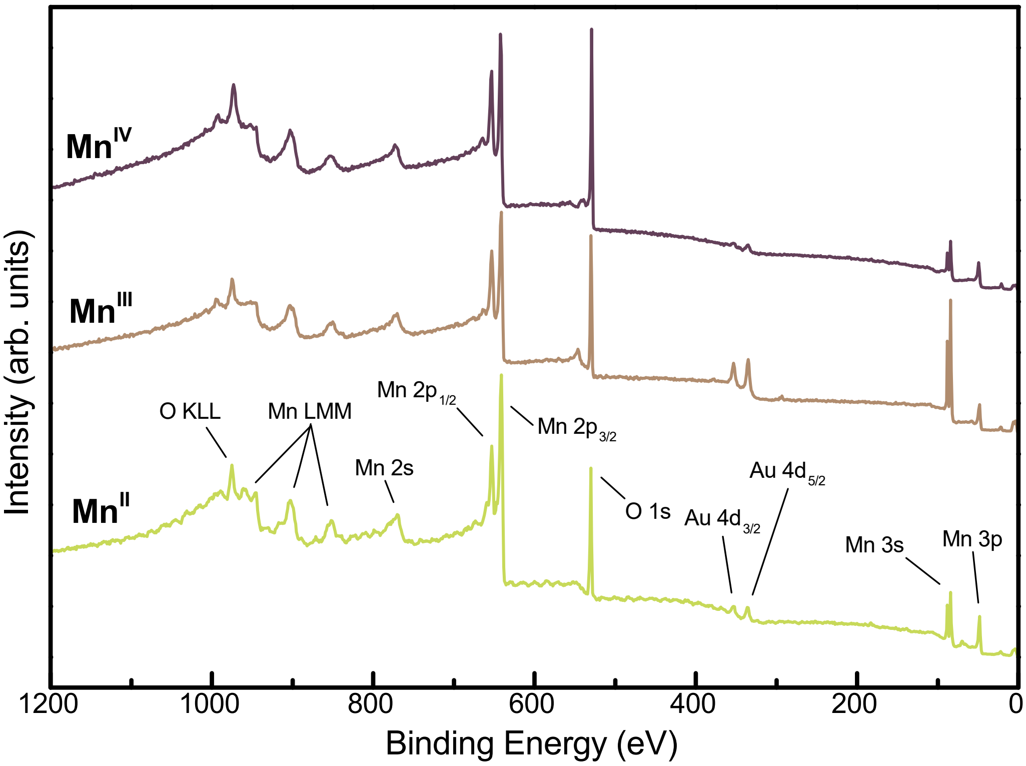

Figure 7.1: XP survey spectra of MnO_x samples deposited on Au with the main oxidation phase of Mn^{II} (chartreuse), Mn^{III} (khaki), and Mn^{IV} (maroon) in a BE range of 0 to 1200 eV. From left to right following peaks can be identified: oxygen Auger peaks O KLL at *ca.* 999 and 975 eV, manganese Auger peaks Mn LMM at *ca.* 952, 903, and 853 eV, manganese core level peak Mn 2s at *ca.* 772 eV, manganese core level peak Mn 2p at *ca.* 653 and 642 eV, oxygen core level peak O 1s at *ca.* 530 eV, gold core level peak Au 4d at *ca.* 354 and 335 eV, manganese core level peak Mn 3s at *ca.* 88 and 84 eV, and manganese core level peak Mn 3p at *ca.* 48 eV [108].

revealing small aberrations in Mn^{II} and Mn^{III}, indicating other oxidized Mn species or defect states present on the surface. Also displayed in figure 7.2, only Mn^{II} phase shows a Mn $2p_{3/2}$ satellite at 647.2 eV [152].

It is well known that higher oxygen content in MnO_x results in a shift of the Mn $2p_{1/2}$ satellite to higher E_{BE} [154]. The Mn $2p_{1/2}$ peak is located at 653.1 eV in Mn^{II} (lit.: 653.3 eV [89]) and Mn^{III}, and 653.3 eV in Mn^{IV}. Powders of 99 % purity give peak positions of 653.4 eV for Mn^{III} and 654.1 eV for Mn^{IV} [156, 157]. In contrast to $\Delta E 2p_{1/2}$, the values match well for Mn^{III}, but reveal a shift of *ca.* 0.8 eV in Mn^{IV}, indicating unpurity of the sputtered Mn^{IV} layers.

Mn 3s: Further work on the examination of the oxidation states in MnO_x is done with the help of the manganese core level peak Mn 3s, also based on the work of ref [153, 154]. The peak distance of the multiplet splitting in the Mn 3s region was found to differ for Mn^{II}, Mn^{III}, and Mn^{IV}. For the evaluation of the peak distances in the sputtered samples, gold core level peak Au 4f had to be discriminated in the spectrum, as displayed in figure 7.3.

The Mn 3s region was subtracted with a Shirley BG and deconvoluted with GL peak fits. The Au 4f was fitted, using a line shape derived from a high resolution Au 4f region from a pure Au sample, as it is displayed in figure 5.2. For the best possible fit of this peak, four GL peaks were necessary, two with low FWHM of 0.6 eV at 87.7 and 84 eV, attributed to pure Au^{O} metal, and two peaks with higher FWHM of 1.4 eV at the same BE values, attributed to small amounts of oxidized $Au^{\delta+}$ species [158, 159]. Mn deposited on a Ti substrate was used as a reference to retrieve a line shape for the Mn 3s region. The

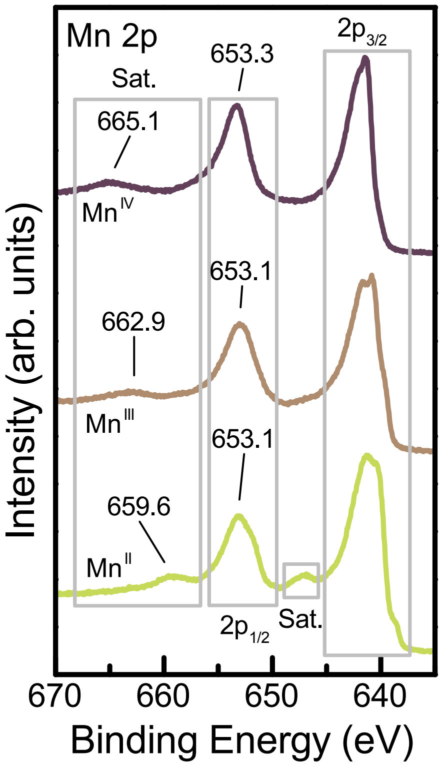

Figure 7.2: XP detail spectra of Mn core level peak Mn 2p in a E_{BE} range of 670 to 635 eV. $\mathrm{MnO_x}$ samples deposited on Au with the main oxidation phase of $\mathrm{Mn^{II}}$ (chartreuse), $\mathrm{Mn^{III}}$ (khaki), and $\mathrm{Mn^{IV}}$ (maroon) are displayed. The E_{BE} of the Mn $2p_{1/2}$ satellite, Mn doublet peak Mn $2p_{1/2}$, Mn $2p_{3/2}$ satellite, and the Mn dublet peak Mn $2p_{3/2}$ are indicated by gray boxes.

main oxidation states of these Mn samples on Ti were clearly assigned with the $\Delta E2p_{1/2}$ and the $\Delta E3s$, offering literature matching values of 6.3 eV in $\mathrm{Mn^{II}}$ (lit.: 5.8 to 6.1 eV), 5.2 eV in $\mathrm{Mn^{III}}$ (lit.: 5.1 to 5.5 eV), and 4.8 eV $\mathrm{Mn^{IV}}$ (lit.: 4.5 to 4.7 eV) [153, 154].

The line shapes were allowed to move ±0.1 eV in their FWHM and ±0.2 eV in the E_{BE}. Further, both Mn 3s peaks were allowed to retrieve the best possible fit with one additional GL fit each. In $\mathrm{Mn^{III}}$, no improvement of the spectrum was achieved with additional peaks. This might be the case due to the annealing process, diminishing the influence of oxidic species such as gold oxide or chemisorbed oxygen. In $\mathrm{Mn^{II}}$, the additional peaks are located at 88.2 and 84.5 eV with FWHM of 0.8 and 1.0 eV. $\mathrm{MnO_x}$ species in oxidation states different from $\mathrm{Mn^{II}}$ may also contribute to the spectrum but are hard to deconvolute separately. Due to the similar FWHM and E_{BE}, the majority of these additional peaks is attributed to $\mathrm{Au^{\delta+}}$ species. Two additional peaks are located at 87.1 and 83.5 eV in $\mathrm{Mn^{IV}}$. In contrast to $\mathrm{Mn^{II}}$, these peaks are not assigned to Au due to the shift to lower E_{BE}, but are rather associated with $\mathrm{MnO_x}$ species in an oxidation state lower than +4 in compliance with the Mn 3s positions of $\mathrm{Mn^{II}}$ and $\mathrm{Mn^{III}}$.

The $\Delta E3s$ values were investigated after deconvolution and calculated to 6 eV ($\mathrm{Mn^{II}}$), 4.9 eV ($\mathrm{Mn^{III}}$), and 4.3 eV ($\mathrm{Mn^{IV}}$). The results compared to the literature values are listed in table 7.1. It is obvious that the deconvolution with the Au 4f line shape combined with the unclear existence of differently oxidized Mn and Au species exhibit values differing slightly (±0.2 eV) from literature. A trend regarding lower $\Delta E3s$ for higher oxidation states clearly is observed and appears in used references as well.

O 1s: In figure 7.4, the spectra of $\mathrm{Mn^{II}}$, $\mathrm{Mn^{III}}$, and $\mathrm{Mn^{IV}}$ are subtracted with a Shirley BG and deconvoluted with GL curves. The main phase $\mathrm{O{-}Mn^{\alpha}}$, where α is the oxidation state of the superior phase (as asserted before), peaks are found at 529.1 ($\mathrm{Mn^{IV}}$), 592.8 ($\mathrm{Mn^{III}}$), and 530 eV ($\mathrm{Mn^{II}}$) in accordance with usual values for metal/manganese-oxygen bondings (lit.: 529.6 to 530 eV) [160, 156, 157]. These peaks show typical FWHM values of 1.0 to 1.1 eV. In $\mathrm{Mn^{III}}$ and $\mathrm{Mn^{IV}}$, an additional Mn−O−Mn peak at a $E_{\mathrm{BE}} = 530.9$ and 530.2 eV is visible, attributed to $\mathrm{O{-}Mn^{\delta}}$ and $\mathrm{O{-}Mn^{\delta+1}}$, where δ is an oxidation state < 3. The FWHM of these peaks are again metal-oxygen typical values of 0.9 ($\mathrm{O{-}Mn^{\delta}}$) to 1.2 eV ($\mathrm{O{-}Mn^{\delta+1}}$), taking higher values in $\mathrm{Mn^{IV}}$ due to the higher possibility of different oxidation states of $\mathrm{O{-}Mn^{\delta+1}}$.

All three $\mathrm{MnO_x}$ possess oxygen species attributed to oxygen vacancy induced defects ($\mathrm{O_V}$) at 531.5 to 531.8 eV, as it was similarly found in $\mathrm{NiO_x}$ in this work (see figure 6.2 at 530.7 eV) and discussed in detail. These $\mathrm{O_V}$ species reveal higher FWHM

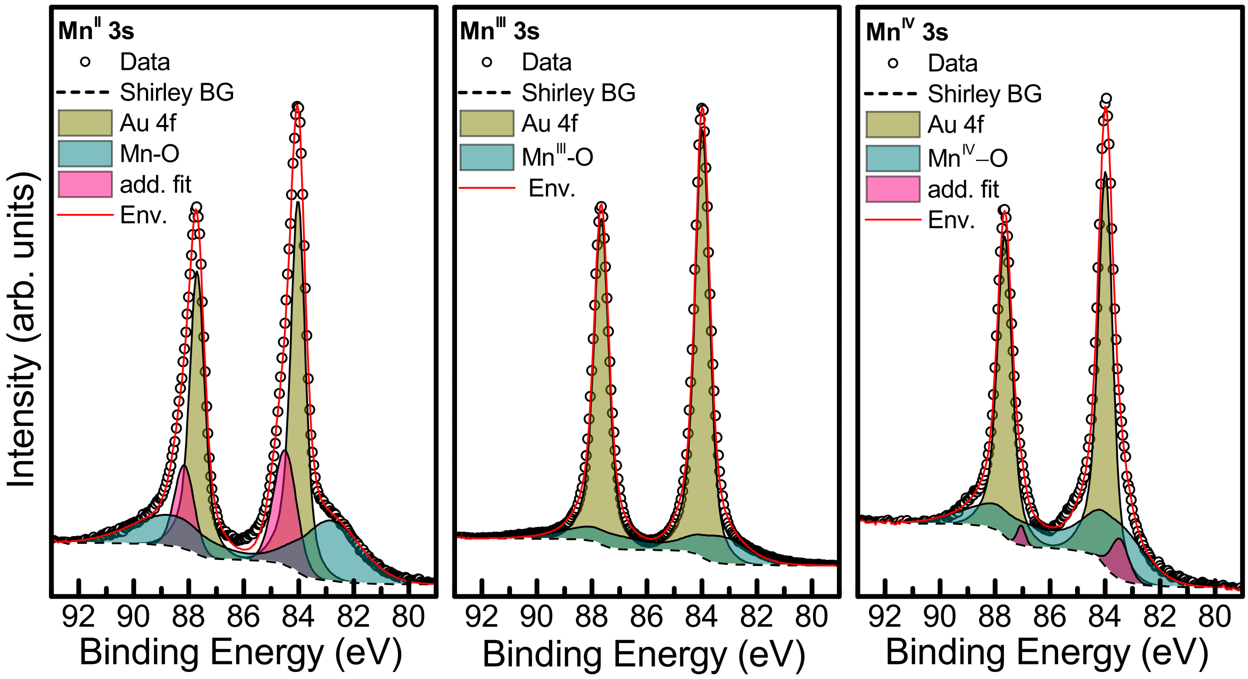

Figure 7.3: XP detail spectra of Mn core level peak Mn 3s in a BE range of 79 to 93 eV. MnO_x samples deposited on Au with the main oxidation phase of Mn^{II} (a), Mn^{III} (b), and Mn^{IV} (b) are displayed. The spectrum is subtracted with a Shirley BG, the peaks are deconvoluted with line shape curves to obtain the Au core level Au 4f (dark yellow), and the Mn core level Mn 3s (dark cyan). If necessary, the data was fitted additionally with Gaussian-Lorentzian peaks (pink).

Table 7.1: XPS values for spin orbital splitting Mn $\Delta E2p_{1/2}$ and multiplet splitting Mn $\Delta E3s$ for this works MnO_x samples, obtained here and compared to the literature values from ref [153] and [154].

Sample	$\Delta E2p_{1/2}$ (eV)	Lit. [153]	$\Delta E3s$ (eV)	Lit. [153]
Mn^{II}	6.5	5.4–6.0 (MnO)	6	6.0–6.1 (MnO)
Mn^{III}	9.8	10.0–10.5 (Mn_2O_3)	4.9	5.1–5.4 (Mn_2O_3)
Mn^{IV}	11.8	11.8–11.9 (MnO_2)	4.3	4.5 (MnO_2)

values of 1.2 (Mn^{III}) to 1.9 eV (Mn^{IV}). Especially in Mn^{IV}, the broad peak and the overlap with the O–Mn$^{\delta+1}$ species indicate unclear deconvolution in minor areas of the spectra.

Evaluation of the Mn/O stoichiometry

To further investigate the sputtered MnO_x species, the proportion of manganese and oxidic species on the surface is investigated. For best possible results regarding the Mn peak areas, Mn 3p has been chosen, since Au $4p_{1/2}$ at *ca.* 643 eV overlaps with the Mn 2p region. The strong Au 4f region overrules the Mn 3s region intensely, leaving only Mn 3p uninfluenced by the Au substrate.

The Mn 3p stoichiometry is investigated *via* the corrected area values A_{corr}, determined in CasaXPS with a region after Shirley BG correction. The BG corrected MnO_x XPS data with A_{corr} is displayed in figure 7.5. The peak area data has to be corrected in regard to several factors, such as the atomic sensitivity factor (SF), the transmission factor *Tf* and the inelastic mean free path λ_i, resulting in a relative sensitivity factor (RSF), calculated by CasaXPS. The raw area values, A_{corr}, and Mn/O ratio is listed in table 7.2. The correction has been done directly in CasaXPS with RSF = 1.42 for Mn 3s and 2.93 for the O 1s region and *Tf*, specially evaluated for used XP spectrometer, along with λ_i, either listed [161]

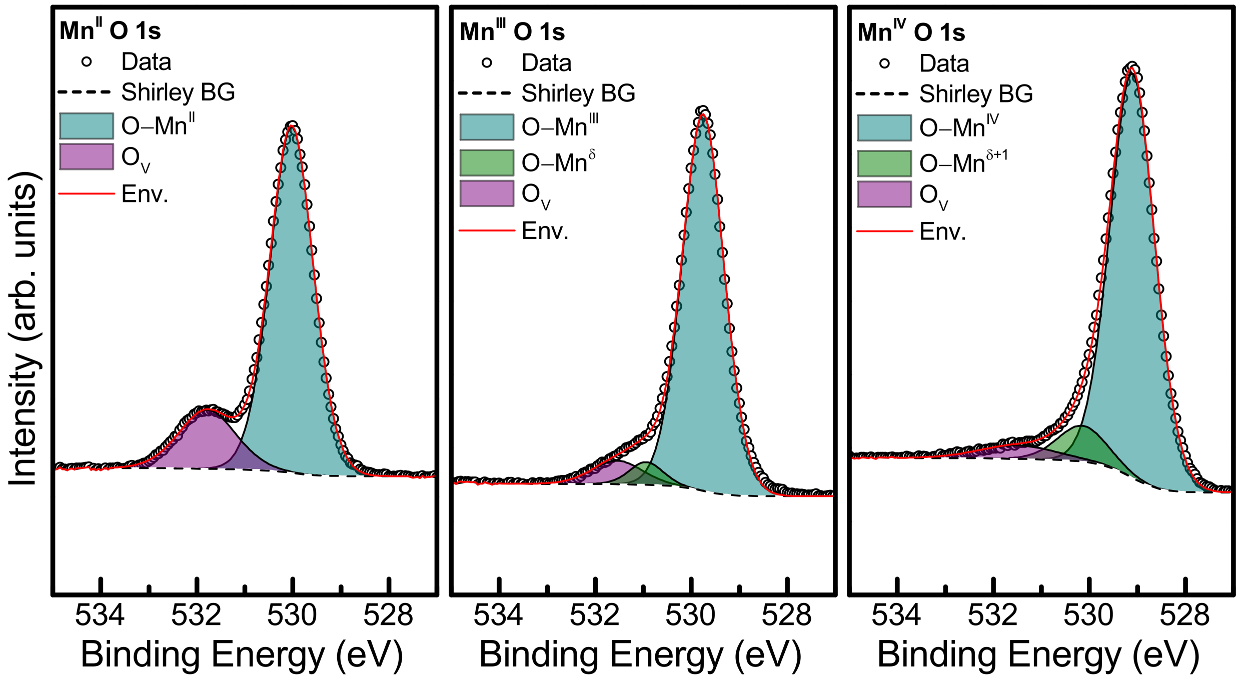

Figure 7.4: XP detail spectra of oxygen core level peak O1s in a BE range of 527 to 535 eV. MnO_x samples deposited on Au with the main oxidation phase of Mn^{II} (left), Mn^{III} (middle), and Mn^{IV} (right) are displayed. The spectrum is subtracted with a Shirley BG, the peaks are deconvoluted with Gaussian-Lorentzian curves to obtain the surface oxygen bound to Mn in the main phase (dark cyan) and in a minor phase (olive), as well as oxygen vacancies (purple).

or calculated, *e.g.* with a software from the national institute of standards and technology (NIST) [162]. A_{corr} has been calculated according to:

$$A_{\mathrm{corr}} = \frac{A}{\mathrm{SF} \times Tf \times \lambda_{\mathrm{i}}} = \frac{A}{\mathrm{RSF}} \qquad (7.1)$$

In the O 1s region, O–Mn$^{\delta}$ species have been deconvoluted, influencing the calculated peak area of the Mn 3p region. To address the main species evaluated with the Mn 2p and the Mn 3s region, the area of the high peak in the O 1s spectra (see figure 7.4), which is suspected to contain the Mn−O−Mn species of the main oxidation state (listed as Mn$^{\alpha}$ in table 7.2), has been used to determine the Mn/O ratio.

In a perfect MnO film, the ratio of Mn^{II}/O is 1, in contrast to a determined ratio in the sputtered film of 0.93, indicating a slight hyper-stoichiometry of oxygen species. The ratio is close to 1 as expected from the O 1s shape, not revealing visible manganese species in a oxidation state different from Mn^{II} and residual oxygen is probably bound in gold oxide species as displayed in figure 7.3a.

For Mn_2O_3, a relation of 2Mn^{III}/3O gives a ratio of 0.67, differing significantly from the determined ratio of 0.52, showing excessive oxygen on the sample. Mn_2O_3 has been synthesized by annealing MnO_2 at 600 °C for 1 h, so residual MnO_2 species might be present in the sample. According to discussed literature, Mn_2O_3 is reduced to Mn_3O_4 at higher T of *ca.* 590 °C by heating in Ar atmosphere. Due to local heating and excess of Mn species in the sample, Mn_3O_4 supposedly has already formed. The E_{BE} shift in the O 1s region of Mn^{III} suggests Mn$^{\delta}$ species with an oxidation state < 3.

The Mn^{IV}/O ratio of MnO_2 has been calculated to 0.43, compared to an ideal ratio of 0.5. The difference of ideal and experimental value is similar to Mn^{II} and the variation is attributed to Mn$^{\delta}$ species in the O 1s region of Mn^{IV} such as Mn_2O_3, Mn_3O_4 or Mn^{II}.

Table 7.2: Raw area values, corrected Area values A_{corr}, and manganese to oxide ratio, determined with XPS, evaluated for the core level peaks Mn 3p and O 1s. The correction has been done in regard to the SF, T, and λ_i values directly with CasaXPS. Areas are given for different Mn—O peaks derived from O 1s, where α is the corresponding oxidation state of the sample and δ is a oxidation state ≤ 3.

Sample	Region	Raw area	$A_{\mathrm{corr}}(\mathrm{Mn}^{\alpha}\text{–O})$	$A_{\mathrm{corr}}(\mathrm{Mn}^{\delta}\text{–O})$	$\mathrm{Mn}^{\alpha}/\mathrm{O}$
$\mathrm{Mn}^{\mathrm{II}}$	Mn 3p	10198.8	7511.51	–	0.93
	O 1s	20496.9	8084.15	–	
$\mathrm{Mn}^{\mathrm{III}}$	Mn 3p	8076.11	5941.59	–	0.52
	O 1s	30170.84	11349	549.87	
$\mathrm{Mn}^{\mathrm{IV}}$	Mn 3p	7634.17	5623.52	–	0.43
	O 1s	36122.67	12977.7	1266.25	

7.2 Electrochemistry of MnO_x

Electrochemistry investigation of MnO_x species on Au_{pol} was performed in 0.1 M KOH with two different protocols, using Ag/AgCl in EC(I) and Hg/HgO in EC(II) as RE (see experimental section for details). Each protocol was conducted with a freshly prepared sample. All correction values regarding the potential scale shift *vs.* RHE and the resistance of the electrolyte R_{el} are presented in table 7.3.

R_{el} is determined by EIS at the OCP of the catalyst, displayed in figure 7.6 for EC(I). The resistance values in the picture are already corrected towards the geometrical surface area of the catalyst (~0.385 and ~0.503 cm^{-2}). To determine the correction value R_{el} for each sample, the real impedance value Z_{Real} at an imaginary impedance value closest to $-Z_{\mathrm{Imag}} = 0\,\Omega$ is taken, to disregard the capacitance of the double layer. As a result, the MnO_x species reveal R_{el} correction values of ca. 23.1 (MnO), 22.7 (Mn_2O_3), and 24.1 $\Omega\,\mathrm{m}^2$ (MnO_2).

Table 7.3: Correction values for activity investigation of MnO_x samples. The values for the RE were obtained in a 600 s OCP measurement while R_{el} is taken from a Nyquist plot, received by EIS at OCP. Note, that the higher R_{el} in Mn_2O_3 arises from the smaller o-ring diameter.

	EC(I)		EC(II)	
Sample	$E_{\mathrm{Ag/AgCl}}$ (V)	R_{el} (Ω)	$E_{\mathrm{Hg/HgO}}$ (V)	R_{el} (Ω)
MnO	0.979	46	0.894	46
Mn_2O_3	0.978	59	0.900	47
MnO_2	0.980	48	0.904	48

The electrochemical characterization presented in figure 7.7a demonstrates the significantly higher OER activity of MnO_2 compared to the other MnO_x samples. The current-voltage curves show an approximately linear course until *ca.* 1.5 V *vs.* RHE, before the current onset and O_2 evolution starts. If the current onset is described by the overpotential η at a current density j of 0.1 $\mathrm{mA\,cm^{-2}}$, MnO_2 reveals the lowest onset η of 370 mV, followed by MnO (390 mV), and finally Mn_2O_3 with 410 mV. Evaluation of η at $j = 5\,\mathrm{mA\,cm^{-2}}$ results in a similar trend, presenting $\eta = 490$ mV for MnO_2, 540 mV for Mn_2O_3, and 550 mV for MnO. The Tafel investigation, displayed in figure 7.7b reveals a low slope of 62 $\mathrm{mV\,dec^{-1}}$ for MnO_2 and higher slope values of 77 $\mathrm{mV\,dec^{-1}}$ for Mn_2O_3 and 88 $\mathrm{mV\,dec^{-1}}$ for MnO. All relevant kinetic parameters are summarized in table 7.4.

In the inset plot in figure 7.7a, the visible redox processes before the OER region are displayed. Mn_2O_3 shows almost no change in current density during oxidation and only a low reduction peak starting at *ca.* 1.15 V *vs.* RHE, decreasing to $-0.07\,\mathrm{mA\,cm^{-1}}$ at 1.0 V *vs.* RHE. MnO and MnO_2 exhibit a similar shape in the investigated region with a spontaneous increase in current density at *ca.* 1.25 V *vs.* RHE to $j = 0.5\,\mathrm{mA\,cm^{-2}}$ on MnO and 0.7 $\mathrm{mA\,cm^{-2}}$ on MnO_2. At $E = 1.0$ to 1.25 V *vs.* RHE, MnO_2 reveals a higher j than MnO, resulting in a similar increase at 1.25 V *vs.* RHE. On the reduc-

Table 7.4: Kinetic parameters obtained during EC of MnO_x in 0.1 M KOH, according to EC(II). The evaluation of the overpotential η at 0.1 and 5 mA cm^{-2}, the Tafel slope and the anodic charge transfer coefficient α_a is given.

Sample	η at 0.1 mA cm^{-2} (mV)	η at 5 mA cm^{-2} (mV)	Tafel slope (mV dec^{-1})	α_a
MnO	390	550	88	0.287
Mn_2O_3	410	540	77	0.328
MnO_2	370	490	62	0.407

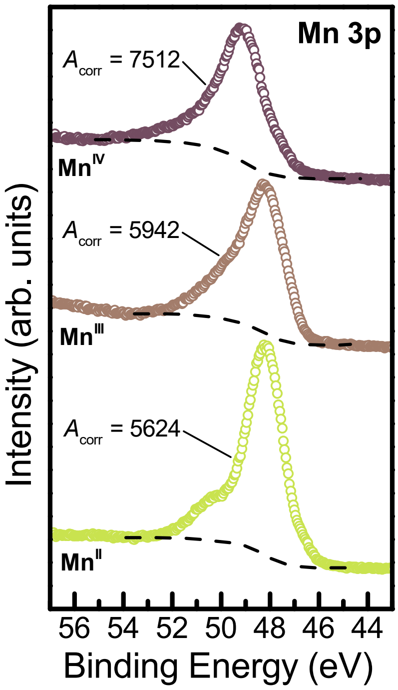

Figure 7.5: XP detail spectra of Mn core level peak Mn 3p in a BE range of 57 to 43 eV. MnO_x samples deposited on Au with the main oxidation phase of Mn^{II} (chartreuse), Mn^{III} (khaki), and Mn^{IV} (maroon) are displayed. The regions are subtracted with a Shirley BG and the peak areas A_{corr}, corrected for the relative sensitivity factor RSF, transmission factor T, and inelastic mean free path IMFP, are given.

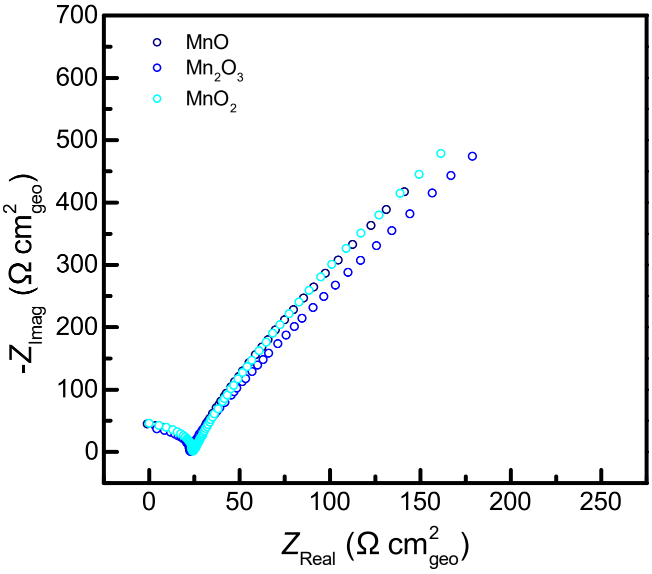

Figure 7.6: Nyquist plot of the EIS data at OCP, determined for MnO (navy), Mn_2O_3 (blue), and MnO_2 (cyan) in EC(I) in 0.1 M KOH. The impedance values in the plot have been corrected towards the geometrical surface area of the catalysts exposed to the electrolyte during EC (0.503 cm^2 for MnO and MnO_2 and 0.385 cm^2 for Mn_2O_3).

tion side, both curves have a relatively strong peak at 1.07 (MnO) and 1.08 V *vs.* RHE (MnO_2), reaching current densities of −0.19 and −0.21 mA cm^{-2}, respectively.

The overall OER performance of Mn^{IV} is superior to Mn^{II} and Mn^{III}. While Mn^{II} shows a lower onset η to Mn^{III} ($D = 20$ mV), Mn^{III} already performs better at $j = 5$ mA cm^{-2} ($D = 10$ mV) and is suspected to improve at higher current densities due to the −11 mV dec^{-1} lower Tafel slope. The reactively sputtered MnO_x catalysts seem to not only differ in their surface properties, *i.e.* their electrochemically available/accessible surface area and provided charge transport, but also in their intrinsic activity due to their large differing Tafel slope values [163].

The activity of screen-printed β-MnO_2 was investigated by Fekete *et al.* [163] for different thicknesses in 0.1 M NaOH (pH 12.9) and an increase in activity has been detected for up to 4.2 µm. They reported an onset η of 450 mV that could be reduced to below 300 mV by nanostructuring MnO_2, reaching $j = 10$ mA cm^{-2} at $\eta = 550$ mV. Gorlin and Jaramillo [153] investigated an electrodeposited, mostly Mn^{III} containing nanostructured MnO_x catalyst in 0.1 M NaOH, reporting an overpotential of

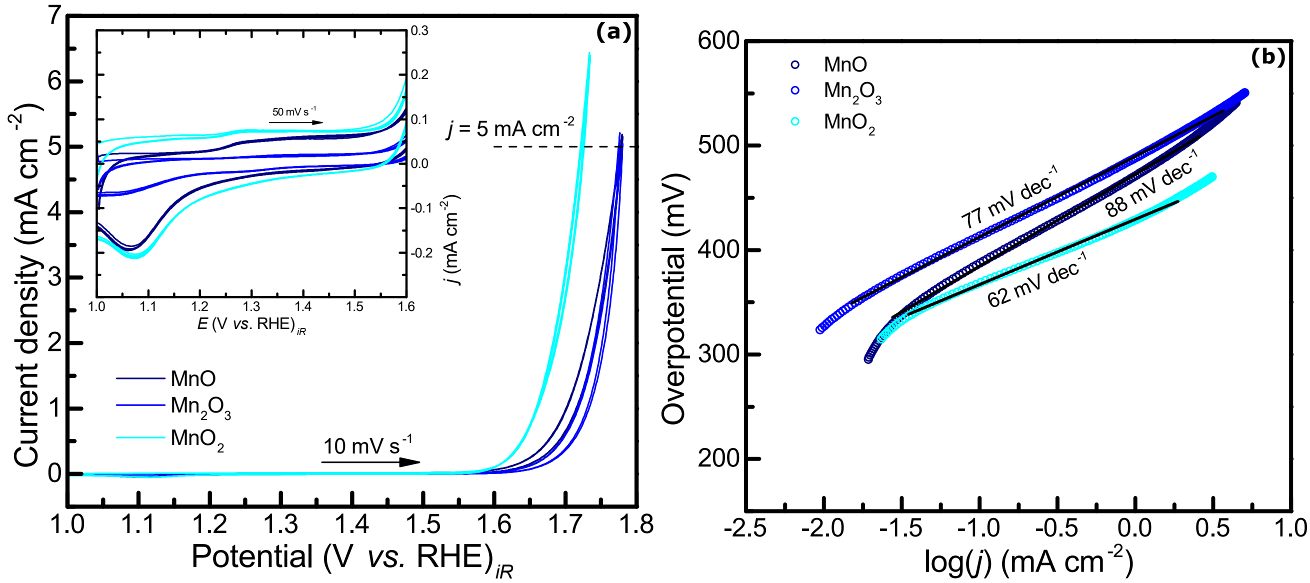

Figure 7.7: Activity evaluation of MnO_x on Au in 0.1 M KOH, presented from 1.0 to 1.8 V *vs.* RHE. Data of MnO is displayed in navy, Mn_2O_3 in blue, and MnO_2 in cyan. (a) CV data after conditioning for 50 cycles between 1.0 to 1.5 V *vs.* RHE with 100 mV s^{-1} according to EC(II). CV are recorded with 10 mV s^{-1} from 1.0 to 1.9 V *vs.* RHE, the overpotential at 5 mA cm^{-2} is indicated by a dashed line. The inset plot displays CV data recorded with 50 mV s^{-1} from 1.0 to 1.9 V *vs.* RHE, zoomed in to estimate the redox wave. (b) Tafel plot, displayed as a function of the overpotential η and the logarithmic current density log(j). Data received from CV depicted in (a), recorded with 10 mV s^{-1}, fitted linearly to obtain the Tafel slope.

540 mV at $j = 10$ mA cm^{-2}. For comparison, in the same test procedure, carbon-supported RuO_2 and IrO_2 reached 10 mA cm^{-2} at $\eta = 390$ mV.

Fekete *et al.* [163] further report Tafel slopes for their commercial and nanostructured β-MnO_2 catalysts of close to 90 mV dec^{-1}, indicating similar intrinsic properties regardless of the surface structure. Without inducing structural change over time in MnO_x, from this experiment MnO_2, *i.e.* Mn^{IV}, is suspected to be the active state during O_2 evolution in alkaline media. Also, in literature the enhancement of MnO_x with gold-support is elaborately discussed. Even traces of Au have been reported to activate MnO_x, indicating local, interfacial interactions between Au and MnO_x [164]. While Au=O and Mn−O−Au are both inactive for water oxidation, they are working as hydrogen acceptors, therefore increasing catalytic activity of the OER by decreasing the free energy of e$^-$ transfer steps involving hydrogen [165, 166].

Behavior over cyclation time

One major point of interest in studying MnO_x as a possible catalyst for water oxidation is not only the stability over time, but also the changes induced in regard to the electrochemical performance. To address these questions, samples have been studied in the previously introduced EC(I). LS were recorded after an activation step of 20 cycles with 5 mV s^{-1} from 1.2 to 1.7 V *vs.* RHE (Act$_1$) in 0.1 M KOH. The results of these sweeps along with the evaluation of the Tafel slopes are displayed in figure 7.8. In contrast to the previously discussed CV data, the activation was carried out at higher potentials, reaching the O_2 evolution regime.

All samples present a similar shape with no obvious oxidation wave, but with slightly different onset potentials, starting at the lowest with MnO_2 (370 mV), followed by Mn_2O_3 (400 mV) and MnO (410 mV). The onset potential is again defined as the overpotential η at a given current density j of 0.1 mA cm^{-1}. Regardless of the different onset, all

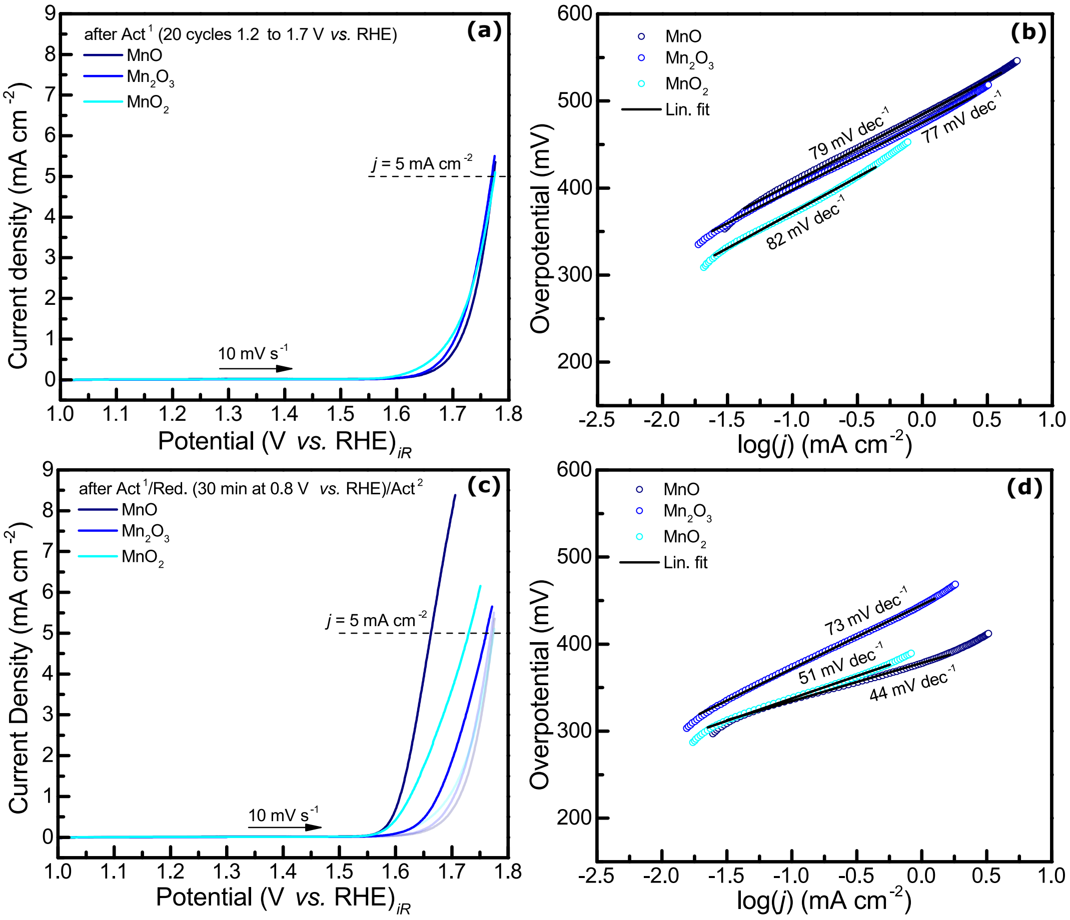

Figure 7.8: Activity evaluation of MnO_x on Au in 0.1 M KOH, measured from 1.0 to 1.9 V *vs.* RHE. Data of MnO is displayed in navy, Mn_2O_3 in blue, and MnO_2 in cyan. (a) LSV data after conditioning for 20 cycles between 1.2 to 1.7 V *vs.* RHE with 5 mV s^{-1} (Act$_1$) according to EC(I). (c) LSV data after Act^1, reduction at 0.8 V *vs.* RHE for 30 min, and reactivation for 20 cycles between 1.2 to 1.7 V *vs.* RHE with 5 mV s^{-1} (Act$_2$). The data from above is indicated as transparent sweeps for direct comparison. LSV were recorded with 10 mV s^{-1} from 1.0 to 1.9 V *vs.* RHE, the overpotential at 5 mA cm^{-2} is indicated by a dashed line. (b) and (d) Tafel plots, displayed as a function of the overpotential η and the logarithmic current density log(j), fitted linearly.

samples show an overpotential η of 540 mV at a current density of 5 mA cm^{-2}. This behaviour is explained with the evaluation of the linear region, revealing the lowest Tafel slope of 77 mV dec^{-1} for Mn_2O_3 and the highest for MnO_2 with 82 mV dec^{-1}, having MnO in between with 79 mV dec^{-1}.

To compare obtained results with the performance after longer cycling time, the experiment was redone. To reduce the surface species oxidized during the cycling procedure and to investigate the reproducibility of these results, all samples were hold at 0.8 V *vs.* RHE for 30 min. Afterwards, a reactivation step (Act$_2$) was carried out, cycling 20 times between 1.2 to 1.7 V *vs.* RHE with 5 mV s^{-1}. These results are visible on the bottom of figure 7.8, where in the bottom left the LSV curves after Act$_1$ are again indicated by transparent lines for direct comparison.

The activity of the MnO_x differs greatly after reduction and reactivation. While MnO and MnO_2 have a similar η at $j = 0.1$ mA cm^{-1} of 340 mV, the O_2 evolution of Mn_2O_3 starts at higher η of 370 mV. Compared to previous results after Act^1, all onset potentials were improved, greatest in MnO with −70 mV, whereas the onset η of MnO_2 and Mn_2O_3 was lowered by −30 mV in both cases. At a current density $j = 5$ mA cm^{-1}, MnO shows an η of 430 mV, compared to 500 mV of MnO_2, and

Table 7.5: Kinetic parameters obtained during EC of MnO_x in 0.1 M KOH, according to EC(I), tabulated after Act_1 and Act_2. The evaluation of the overpotential η at 0.1 and 5 mA cm^{-2}, the Tafel slope and the anodic charge transfer coefficient α_a is given.

Sample	Act step	η at 0.1 mA cm^{-2} (mV)	η at 5 mA cm^{-2} (mV)	Tafel slope (mV dec^{-1})	α_a
MnO	Act_1	410	540	79	0.320
	Act_2	340	430	44	0.574
Mn_2O_3	Act_1	400	540	77	0.328
	Act_2	370	530	73	0.346
MnO_2	Act_1	370	540	82	0.308
	Act_2	340	500	51	0.495

530 mV of Mn_2O_3. In regard to the data after only Act^1, the η of Mn_2O_3 has changed barely (−10 mV), while MnO_2 was improved by 40 mV, and the activity of deposited MnO has been improved greatly by 110 mV.

By investigating the behavior at higher potentials, *i.e.* the Tafel slopes, the performance change after the 2nd activation step is also very pronounced. MnO reveals a low Tafel slope of 44 mV dec^{-1}, corresponding to an improvement of 35 mV dec^{-1}. The Tafel slope of MnO_2 is improved by 31 mV dec^{-1} towards 51 mV dec^{-1}, while Mn_2O_3 is hardly changed by 4 mV dec^{-1} to 73 mV dec^{-1}.

Activation of MnO_x

The processes during activation Act_1 and reactivation Act_2 are worth being studied in detail due to the high activity enhancement. To recall, both activations have been carried out by cycling 20 times from 1.2 to 1.7 V *vs.* RHE with a scan rate of 5 mV s^{-1}. The course of the CV for all MnO_x samples is displayed in figure 7.9, the inset plots show the same graphs, but a more detailed view of the O_2 evolution onset.

After Act_1, all samples show typical behaviour for CV curves, rising to the maximum j and decreasing with lower applied potential at lower j than before. All samples also decrease in their maximum current over the cycling duration, as it is visible due to the colour mapping. After reduction at 0.8 V *vs.* RHE and a second activation step Act_2, the behaviour of the catalysts changes to increased current densities—after reaching the maximum—on the back way from 1.7 to 1.2 V *vs.* RHE. Similar to activated samples after Act_1, the current density decreases over cycling duration.

As already stated during the LSV evaluation, the current densities increase at the same applied potentials along with a shifted onset regarding the O_2 evolution. Mn_2O_3 after Act_1 in figure 7.9c shows very low degradation during cycling, same behaviour is again observed for MnO_2 after Act_2 in figure 7.9f.

To compare the degradation of the current density over cycling duration, the j values at an arbitrary potential of 1.6 V *vs.* RHE have been evaluated for every cycle on each sample. Figure 7.10 displays these values along with an exponential fit of the data to investigate a linear region of the current density, *i.e.* a saturation value of the activation/reactivation process.

In figure 7.10a, MnO_x after Act_1 is compared, revealing similar behaviour for MnO (0.07 to 0.01 mA cm^{-2}) and Mn_2O_3 (0.10 to 0.02 mA cm^{-2}) with rapidly decreasing in j at 1.6 V *vs.* RHE for the first 4 to 5 cycles, flattening out until cycle 8 and 10, respectively, and then staying more or less constant until cycle 20. After Act_1, no finished charging process is observed. The behaviour is slightly different for MnO_2 (0.11 to 0.04 mA cm^{-2}), starting at higher j initially, decreasing rapidly after 3 cycles, and staying constant for the residual cycles 5 to 20.

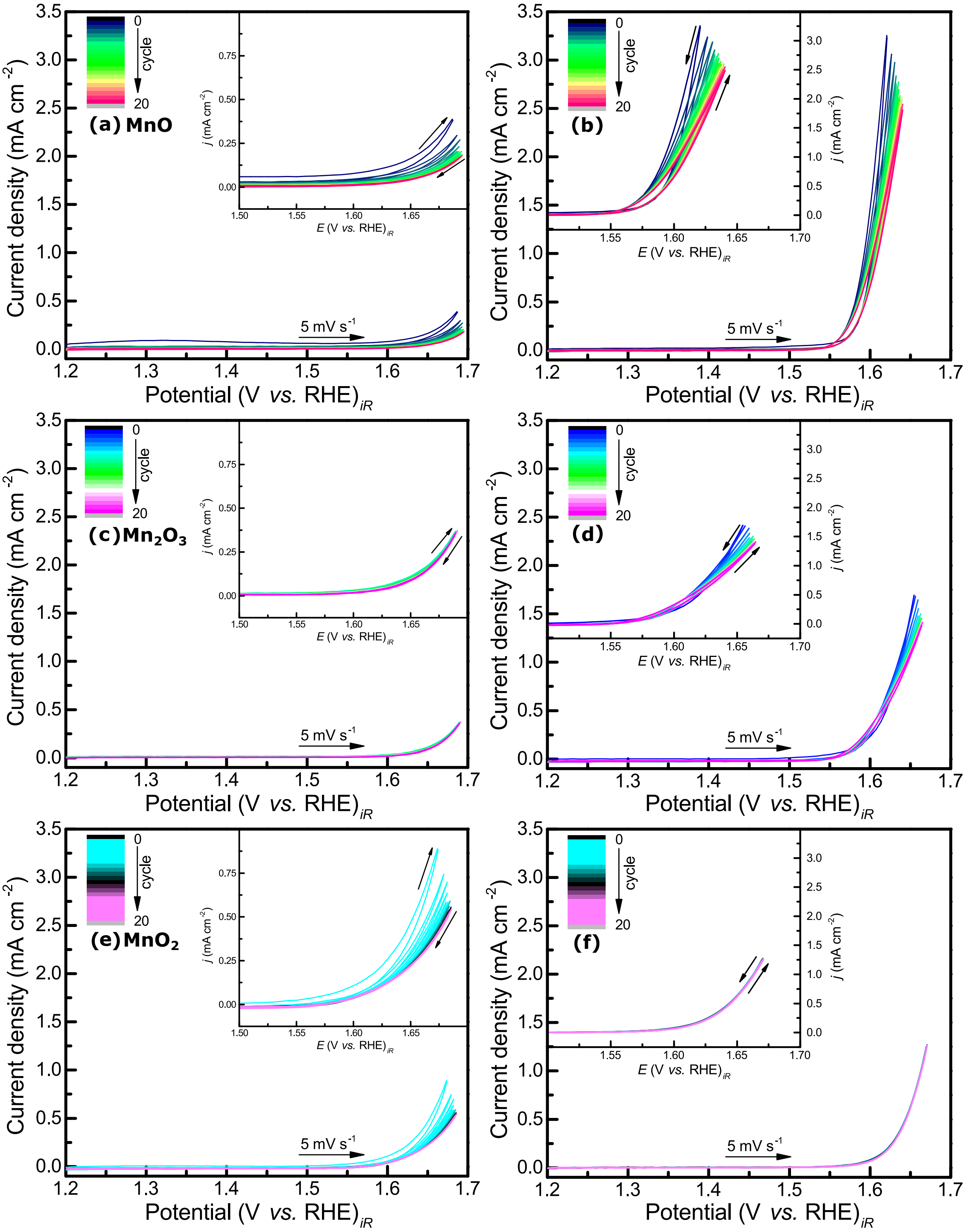

Figure 7.9: Activation (Act_1) and reactivation (Act_2) process for MnO_x. Both procedures have been carried out as 20 cycles with 5 mV s^{-1} from 1.2 to 1.7 V *vs.* RHE in 0.1 M KOH. The course of the CV from the 1st to 20th is displayed as a color map. MnO (a,b) starts navy and goes over into pink, Mn_2O_3 (c,d) is blue into magenta, and MnO_2 (e,f) goes from cyan into light magenta. The inset plots display a more detailed view of the onset region into O_2 evolution from 1.5 to 1.7 V *vs.* RHE.

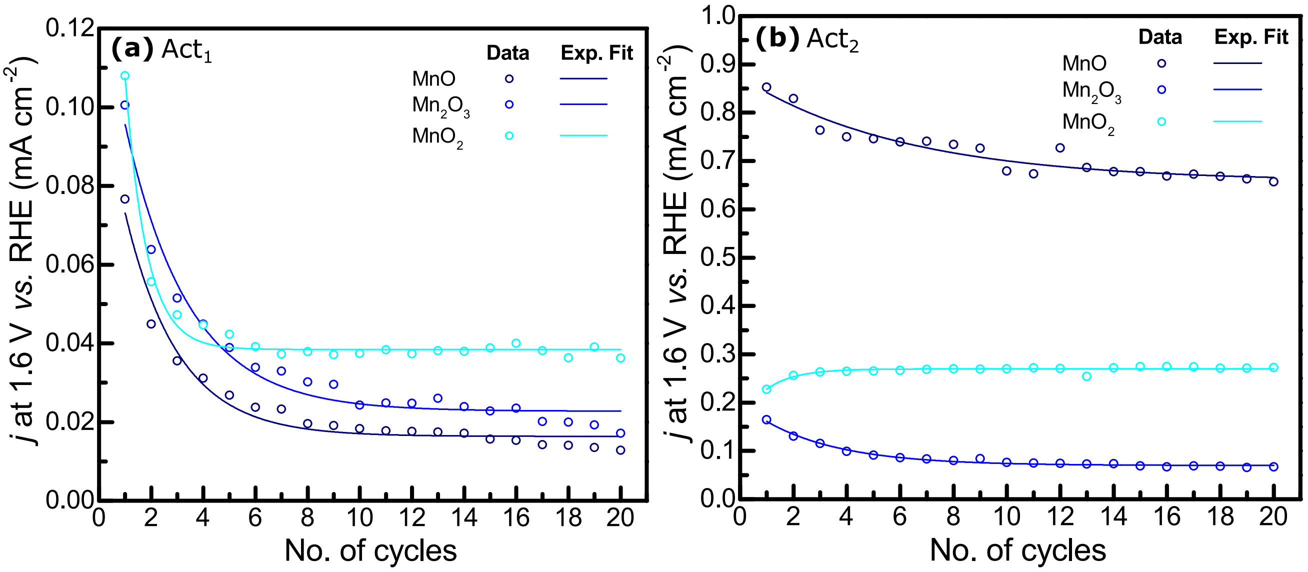

Figure 7.10: Current density at 1.6 V *vs.* RHE during the activation Act$_1$ (a), and reactivation Act$_2$ (b), given for each cycle and fitted exponentially to investigate a saturation current density. Both activation processes have been carried out for 20 cycles from 1.2 to 1.7 V *vs.* RHE with 5 mV s^{-1}, using 0.1 M KOH as electrolyte.

After Act$_2$, displayed in figure 7.10b, the overall behaviour of MnO_x changes significantly. All samples show higher activity in the investigated region. In contrast to MnO and Mn_2O_3, the activity of MnO_2 (0.23 to 0.27 mA cm^{-2}) is slightly enhanced over cycling duration, with increasing *j* up to cycle 5 and staying constant for the residual cycling. Mn_2O_3 (0.16 to 0.07 mA cm^{-2}) reveals the overall lowest *j*, decreasing more rapid in the first 4 cycles, reaching a plateau from cycle 7 to 11, further decreasing afterwards. In comparison, high current densities are achieved by MnO (0.85 to 0.67 mA cm^{-2}), showing inconsistent behaviour, jumping ±0.05 mA cm^{-2}, before flattening from cycle 16 to 20. The charging process might not be finished in MnO.

The process of activation is mainly associated with the oxidation of MnO_x towards Mn^{IV} species [93, 92]. The almost instantaneously flattening of the current density in MnO_2 during Act$_2$ indicates full conversion of Mn species in other oxidation states towards Mn^{IV} during the previous cycling. Partially reduced species during the CA at 0.8 V *vs.* RHE may be converted quickly during the first cycles or not be reduced at all during CA. The highest activity during Act$_1$ for MnO_2 is associated with the highest initial amount of Mn^{IV} on this sample. This is conclusive with the decreasing activity with decreasing Mn oxidation state.

The early flattening region of Mn_2O_3 during Act$_1$ is associated with the high temperature deposition hindering oxidation of the Mn species on the sample, similar to the lower rate of Ni^{II}/Ni^{III} conversion in the high temperature NiO_x samples. During reduction at 0.8 V *vs.* RHE, Mn_3O_4 is suspected to be formed on the samples which is more voluntary oxidized towards Mn^{IV} during Act$_2$.

MnO however, exhibits very low current densities at first due to its low overall oxidation state, but also gives a relatively high current response at low potentials for the first cycle and reveals steady decrease of *j* at 1.6 V *vs.* RHE, indicating gradually formation of catalytically active Mn^{IV} species during the activation. The CA at 0.8 V *vs.* RHE, in contrast to the other MnO_x, gives rise to oxidation towards Mn_3O_4 of residual Mn^{II} species on the sample, resulting in high activity during Act$_2$ due to the oxidation of made available Mn^{III} species. As a consequence, MnO does not exhibit an equilibrium *j* during Act$_2$ (see figure 7.10b) because of further oxidation of the Mn species.

Capacitance of MnO_x

The EDLC has been evaluated in the same region and in the same manner as NiO_x before, presenting the results in figure 7.11. CV was measured in a potential range of 1.02 to 1.12 V *vs.* RHE with scan rates of 10 to 250 $mV\,s^{-1}$. Several approaches to the EDLC investigation can be found in literature, *e.g.* cycling at 0.9 to 1.3 V *vs.* RHE with scan rates between 5 to 100 $mV\,s^{-1}$ for Mn_2O_3 and Mn_3O_4 [167], or cycling with the same scan rate from 0 to 1 V *vs.* RHE to evaluate MnO_2 as supercapacitor [142]. The EDLC of Mn_3O_4 has also been investigated by cycling between 0 to 0.8 V *vs.* RHE with 50 $mV\,s^{-1}$ [168].

To generate consistency in the evaluation of the TMO in this work, the same region as for NiO_x has been chosen, the current value of the 5th cycle at a potential of 1.07 V *vs.* RHE (see dashed lines in figure 7.11a to c) is plotted against the scan rate. A linear fit of the obtained current values is used to determine the capacitance as the slope of the fit, as it is displayed in figure 7.11d.

The general shape of the CV curves of MnO and MnO_2 is similar, revealing a flat shape for low sweep rates, especially for 10 and 20 $mV\,s^{-1}$ and a constant oxidation current as a consequence. More peculiar at higher scan rates, the oxidation current rises until *ca.* 1.06 V *vs.* RHE, merging into a relatively linear I response until 1.12 V *vs.* RHE. The reduction current on the other hand decreases exponentially until *ca.* 1.09 V *vs.* RHE and further linearly for the remaining E. Overall, this behavior seems more pronounced for MnO, also due to the higher oxidation and reduction currents achieved.

In comparison, the overall I response by Mn_2O_3 is *ca.* 10 times lower than MnO. During the oxidation, Mn_2O_3 does not reach a flattening current plateau, but increases to the maximum value at $E = 1.12$ V *vs.* RHE. When reduced, Mn_2O_3 exhibits a much narrower exponential current drop until *ca.* 1.15 V *vs.* RHE, before the linear region starts. All MnO_x posses a higher reduction current response with a trend towards even lower currents at decreasing E.

By plotting I at $E = 1.07$ V *vs.* RHE against the scan rate as described above, a linear fit is applied to calculate the pseudo-capacitance of MnO_x for the anodic (charge) and cathodic (discharge) curves. Due to the overall low I achieved by Mn_2O_3, a fairly low C_{dl} of 66 (anodic) and 60 µF (cathodic) is calculated. It is noted once more, that the EC evaluation of Mn_2O_3 has been conducted on a lower geometrical surface area. The highest C_{dl} is reported for MnO with 741 µF on the anodic branch, but only 671 µF based on cathodic currents, creating a C_{dl} redox difference of 70 µF. MnO_2 has an anodic C_{dl} of 541 and 493 µF for the cathodic, respectively, resulting in a difference of 48 µF.

Taking the RMS values of both branches and calculating the EDLC in regard to the geometrical surface area, more comparable results are obtained. The intrinsic C_{dl} of MnO is calculated to 1379 and MnO_2 to 1031 $\mu F\,cm^{-2}$. Mn_2O_3 still has low C_{dl} of 164 $\mu F\,cm^{-2}$. Mn_2O_3 has been synthesized by annealing MnO_2 at 600 °C for 1 h after deposition, resulting in a difficult to compare surface structure in regard to the other MnO_x samples. Still, when comparing the other two MnO_x, a higher C_{dl} is reported for the cycled MnO.

Looking at the CV results in figure 7.7, a low I reduction peak has been observed in the investigated region for the EDLC, consistent with the CV shapes at different scan rates in this area. For a more reliable result, a region with less pronounced current changes, *i.e.* redox processes, such as 1.35 to 1.45 V *vs.* RHE, could have been evaluated. Overall, the I response on the positive and negative sides are not symmetric, resulting in major value differences regarding the EDLC. The investigated MnO_x samples, as a consequence, may not be suitable as EC super-capacitor material [169]. The non-perfectly rectangular shape of a MnO_2 electrode has been associated with polarization resistance [170]. Not

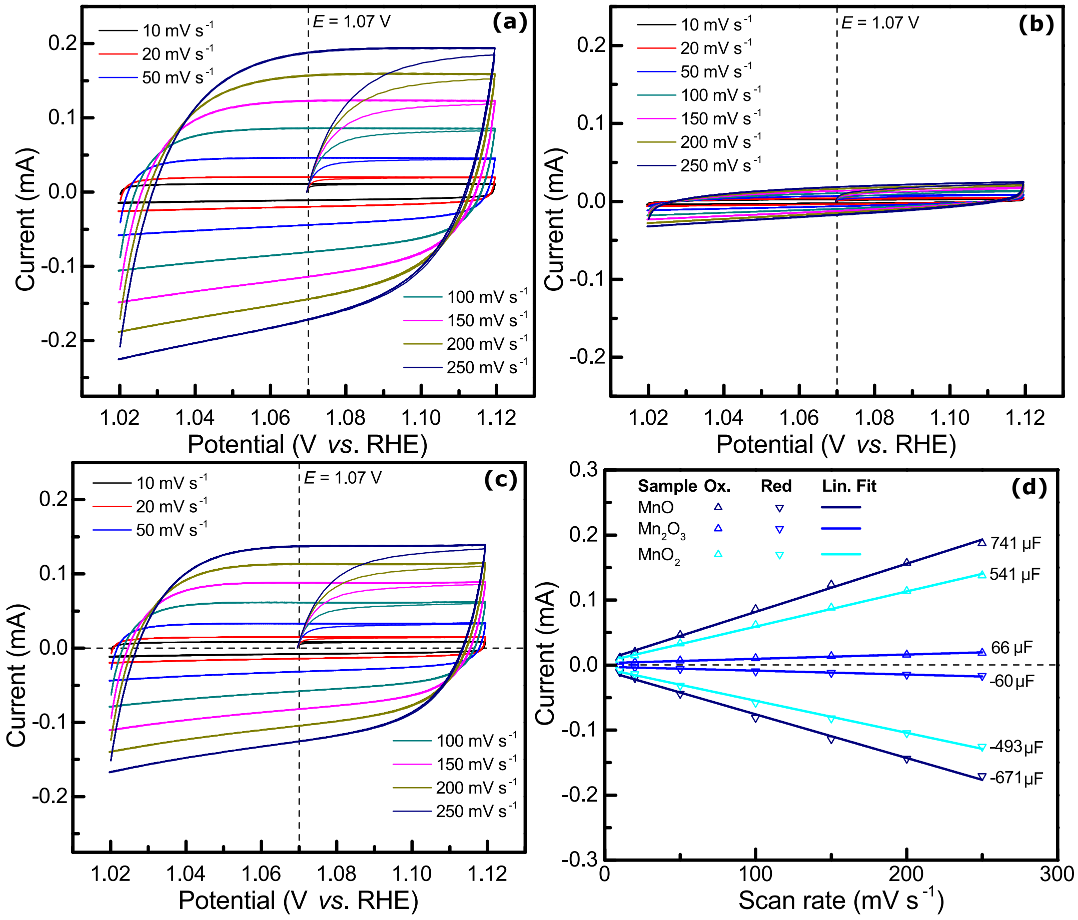

Figure 7.11: CV data of deposited MnO (a), Mn_2O_3 (b), and MnO_2 (c), recorded in 0.1 M KOH from 1.02 to 1.12 V *vs.* RHE with scan rates of 10, 20, 50, 100, 150, 200, and 250 mV s^{-1} to obtain the EDLC according to EC(I). EDLC evaluation (d), data based on the current value of CV at 1.07 V *vs.* RHE. The capacitance is approximated with a linear fit of the oxidation and the reduction current values for MnO (navy), Mn_2O_3 (blue), and MnO_2 (cyan).

only due to this characteristic behaviour, but due to previous results from literature, observing formation of MnO_2 species during cycling of MnO_x, MnO_2 along with residual Mn_2O_3 is suspected to be the main MnO_x phase during determination of the EDLC [93, 92].

The efficiency of MnO_x as pseudo-capacitors is further reported to decrease with growing film thickness, indicating that bulk material is not addressed electrochemically due to slower ionic transport or non-free diffusive protons [170]. This is important to consider, since the films in this work consist of *ca.* 10 nm thickness. Toupin *et al.* [170] investigated the chemical change of MnO_2 films with varying thicknesses with XPS and concluded a chemical change only for thin films. Their results indicate the presence of Mn^{III} and Mn^{IV} species as the reduced and oxidized form, respectively, in a E range relevant to the evaluation in this work. Furthermore, they concluded the involvement of the ionic species in the electrolyte in the charge storage mechanism of surface MnO_2. For this work, using KOH as electrolyte, a reaction mechanism is formulated as following:

$$(MnO_2)_{surface} + K^+ + e^- \longleftrightarrow (MnO_2^-K^+)_{surface} \tag{7.2}$$

In contrast, the reaction in the bulk material, where intercalation of H^+ is assumed to be the charge storage mechanism, a reduction of the Mn^{IV} to Mn^{III} is suspected to occur [170, 171].

$$MnO_2 + H^+ + e^- \longleftrightarrow MnOOH \qquad (7.3)$$

Based on previous observations and reactions, the low C_{dl} in deposited Mn_2O_3 is attributed to low interaction of the surface species, since it has been associated to be the main mechanism for charge storage. Several theories can be developed based on this observation. The annealing step towards synthesis of Mn_2O_3 prevents the sample from forming the MnO_2 species active during storage. In XPS evaluation, a fairly low amount of oxygen induced defects has been observed for thin films of Mn_2O_3 in contrast to MnO, which may be one factor for the Mn_2O_3/MnO_2 conversion during cycling, giving respect to the literature observation, that all MnO_x are oxidized to Mn_2O_3 above 0.9 V *vs.* RHE in alkaline environment [93].

7.3 Chemical Composition after EC

After activity characterization, a second XPS measurement of the three MnO_x samples was conducted to investigate the chemical change during cycling in 0.1 M KOH. As already discussed in the beginning of this chapter, a survey spectrum was recorded for a first view of each sample (see figure 7.12) and afterwards high resolution detail spectra of the core level peaks Mn 2p, Mn 3s, and O 1s. In the survey, the species on the sample were assigned to manganese and oxygen mostly, with residual potassium and carbon present due to the contact with electrolyte (KOH) and the atmosphere, respectively, along with gold from the substrate, as it was already detected on all samples before EC (see figure 7.1).

Mn 2p: The Mn 2p region was used to determine the oxidation state and as such the main oxide phase in the cycled MnO_x samples. The detail spectra after EC are depicted in figure 7.13, the results of the satellite-peak distances are available in table 7.6.

Evaluation of Mn^{II}_{EC} results in a new $\Delta E2p_{1/2}$ of 11.1 eV, matching well with the literature results for MnO_2 (lit.: 10.0 to 11.2 eV) [153, 154]. Similar results are obtained for Mn^{III}_{EC} and MMn^{IV}_{EC}, giving a $\Delta E2p_{1/2}$ value of 11.2 and 11.0 eV, respectively. From the $\Delta E2p_{1/2}$, Mn_3O_4 can be suspected to be the main phase, since a peak distance of 11.3 eV is reported by ref [154],but a closer look reveals this is not conclusive with their cited values of 10 to 10.5 eV. More available literature and the corresponding citations indicate the presence of MnO_2 at this distances.

Mn 3s: For further analysis of the main phase, again the Mn core level peak Mn 3s is taken into account and the BE distance $\Delta E3s$ used for identification. High resolution detail spectra of the Mn 3s region are displayed in figure 7.14. For Mn^{II}_{EC} and Mn^{IV}_{EC}, the Au 4f peak was deconvoluted with a Au 4f line shape in the same manner discussed earlier. To not falsify the values, no Mn line shape was used for peak fitting, instead one GL peak was allowed for each Mn 3s peak. To determine the $\Delta E3s$ values, the Au 4f peak is neglected and the maximum values of the GL curves attributed to the Mn species is considered.

The HBEP was found at 87.6 (Mn^{II}_{EC}), 87.3 (Mn^{III}_{EC}), and 87.5 eV (Mn^{IV}_{EC}), giving rise to peak distances of 3.9 (LBEP: 83.7 eV), 3.8 (LBEP: 83.5 eV), and 4.0 eV (LBEP: 83.6 eV), as listed in table 7.6. Gorlin *et al.* [153] note minimum $\Delta E3s$ values of 4.5 eV for MnO_2, indicating a non-perfect fit of the Mn 3s regions overlapped by the high intensity Au 4f peak. More peaks for deconvolution might be helpful to receive more matching values, but would have falsified the results immensely. Mn^{IV} is suspected to be the main species in all MnO_x samples after EC by deconvolution of the core level peak Mn 3s. Recall, that the suspected phase with the help of the $\Delta E2p_{1/2}$ value was Mn_3O_4.

O 1s: The O 1s region was investigated again to observe the permanent changes in the oxidic components, such as metal hydroxide species, and to deconvolute the adsorbed carbon oxide species

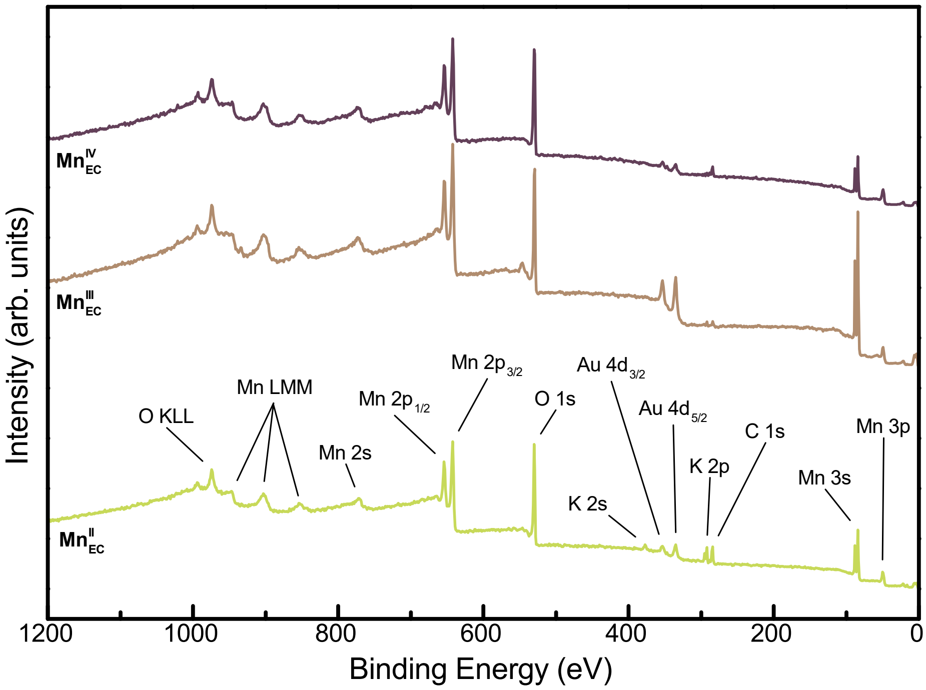

Figure 7.12: XP survey spectra of MnO_x after EC, namely Mn^{II}_{EC} (chartreuse), Mn^{III}_{EC} (khaki), and Mn^{IV}_{EC} (maroon) in a BE range of 0–1200 eV. From left to right following peaks can be identified: oxygen Auger peaks O KLL at *ca.* 994 and 974 eV, manganese Auger peaks Mn LMM at *ca.* 947, 903, and 854 eV, manganese core level peak Mn 2s at *ca.* 771 eV, manganese core level peak Mn 2p at *ca.* 654 and 642 eV, oxygen core level peak O 1s at *ca.* 530 eV, potassium core level peak K 2s at *ca.* 377 eV, gold core level peak Au 4d at *ca.* 353 and 335 eV, potassium core level peak K 2p at *ca.* 295 and 292 eV, carbon core level peak C 1s at *ca.* 284 eV, manganese core level peak Mn 3s at *ca.* 88 and 84 eV, and manganese core level peak Mn 3p at *ca.* 50 eV [108].

Table 7.6: XPS values for Mn $\Delta E2p_{1/2}$ and Mn $\Delta E3s$ splitting for the deposited MnO_x samples after EC measurements for 3 h in 0.1 M KOH, obtained in this work. The used literature suggest 10.0 to 11.2 eV for $\Delta E2p_{1/2}$, and *ca.* 4.5 eV for $\Delta E3s$ [153, 154].

Sample	$\Delta E2p_{1/2}$ (eV)	$\Delta E3s$ (eV)
Mn^{II}_{EC}	11.1	3.9
Mn^{III}_{EC}	11.2	3.8
Mn^{IV}_{EC}	11	4.0

for a stoichiometry check. Figure 7.15 presents the deconvoluted XP detail spectra of the core level peak O 1s for all MnO_x samples. The data is subtracted with a Shirley BG and deconvoluted by GL curves. Metal oxide species were allowed at 529 to 530 eV with a FWHM of 1.0 ±0.2 eV, hydroxides at 530.5 to 531.5 eV with a FWHM of 1.0 to 2.0 eV. Organic carbon oxygen species are expected at 531.5 to 533 eV, fixed at the same FWHM as the hydroxides.

The O–Mn^{α} species are present at BE values of 529.7 (Mn^{II}_{EC}) and 529.5 eV (Mn^{III}_{EC} and Mn^{IV}_{EC}), at FWHM values of 1.1 eV for Mn^{II}_{EC}/Mn^{IV}_{EC}, and 1.2 eV for Mn^{III}_{EC}. Peak area integration results in 80.1, 77.4, and 60.3 at-% of lattice oxygen species in Mn^{II}_{EC}, Mn^{III}_{EC}, and Mn^{IV}_{EC}.

Metal hydroxides are present at 531.2 and 530.8 eV for Mn^{II}_{EC} and Mn^{III}_{EC}/Mn^{IV}_{EC}, respectively, at FWHM of 1.4, 1.6, and 1.8 eV. The atomic concentration *via* peak area integration results in 17.7, 17.5, and 39 at-% for Mn^{II}_{EC}, Mn^{III}_{EC}, and Mn^{IV}_{EC}. Small amounts of adsorbed carbon oxide species along with adsorbed or intercalated H_2O are determined as following: In Mn^{II}_{EC} at 532.8 eV with a concentration of 2.3 at-%, in Mn^{III}_{EC} at 532.5 eV with 5.1 at-%, and in Mn^{IV}_{EC} at 532.9 eV with 0.8 at-% concentration.

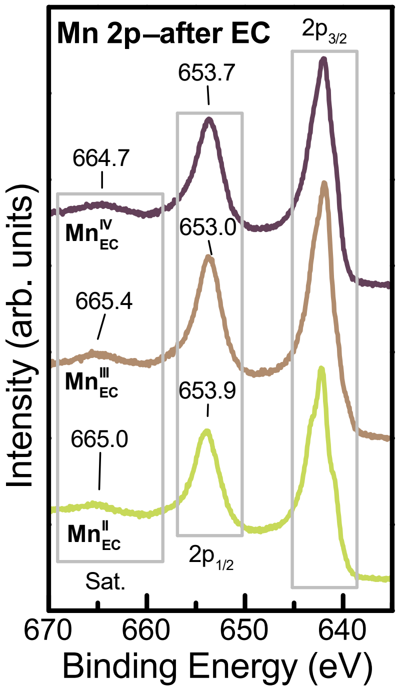

Figure 7.13: XP detail spectra of Mn core level peak Mn 2p after EC in a BE range of 670 to 635 eV. Mn$^{II}_{EC}$ (chartreuse), Mn$^{III}_{EC}$ (khaki), and Mn$^{IV}_{EC}$ (maroon) are displayed. The BE areas of the 2p$_{1/2}$ satellite, Mn 2p$_{1/2}$, and Mn 2p$_{3/2}$ are indicated by grey boxes. The important BE positions of the peaks are given.

Evaluation of the Mn/O stoichiometry after EC

To evaluate the Mn/O stoichiometry once again, not only the lattice oxide, but also the new hydroxide peak (metal hydroxide M–OH) in the O 1s region (see figure 7.15) has to be considered. Similar to the stoichiometry investigation of the freshly sputtered samples, the peak areas had to be corrected with the corresponding SF, T, and IMFP values, directly taken from the software CasaXPS, presenting the results in table 7.7. To determine the amount of MnO$_x$, again the Mn 3p region has been used, being displayed with the corresponding corrected peak area values in figure

Residual KOH was visible in all XP spectra as K 2p$_{3/2}$ peak at *ca.* 292.2 to 292.4 eV [108], which has to be considered for stoichiometry calculations, implying each potassium atom on the sample is bound to one OH-group in the O 1s region. As a consequence, the corrected peak area of K is subtracted from A_{corr}(O–H), resulting in new values for the formed metal hydroxides, as presented in table 7.8.

The peak area A_{corr}(Mn−O/OH) is now compared to both A_{corr}(O−Mn) and A_{corr}(O−H), to obtain the manganese stoichiometry on the sample. Mn(OH)$_2$ reveals a stoichiometric relation of one Mn atom to two OH-groups, so if all manganese hydroxide in the sample is present as Mn(OH)$_2$, the concentration of these hydroxide species can be calculated. Obtained knowledge about the metal hydroxide species finally allows evaluation of the correct Mn/O ratio, considering lattice oxide species. All these values are summarized in table 7.9, with the corresponding relevant peak areas and calculated concentration and ratio.

The amount of manganese used to form the estimated Mn(OH)$_2$ species is subtracted from the Mn 3p peak area and the relation to the full Mn amount gives the concentration on the samples. Subtracted Mn 3p region is than calculated against the amount of lattice oxygen in the O 1s region to determine the Mn/O ratio. While *ca.* 91.3 % of the OH species in Mn$^{II}_{EC}$ are attributed to residual KOH on the sample, a low concentration of only 2.2 % is found on this sample. In comparison, the concentration of Mn(OH)$_2$ was determined to 26.9 and 58.2 % on Mn$^{III}_{EC}$ and Mn$^{IV}_{EC}$. Recalling that all samples were cycled for the same amount of time, these results vary a lot. While Mn$^{II}_{EC}$ does form nearly no hydroxide species, Mn$^{III}_{EC}$ converts around 1/4 of its MnO$_x$ into Mn(OH)$_2$, and Mn$^{IV}_{EC}$ doubles this amount to half conversion of Mn oxide to hydroxide species.

An evaluation of the Mn/O ratios results in 0.42, indicating Mn^{IV} as the main species, as it was assumed based on the literature data of the ΔE3s multiplet splitting distance (3.9 eV compared to 4.5 eV in ref [153]). It is mentioned herein, that the amount of K found on this sample is relatively high, as it is observed in figure 7.17. Studies on K$_2$MnO$_4$ by Biesinger *et al.* [152] revealed a shoulder of the

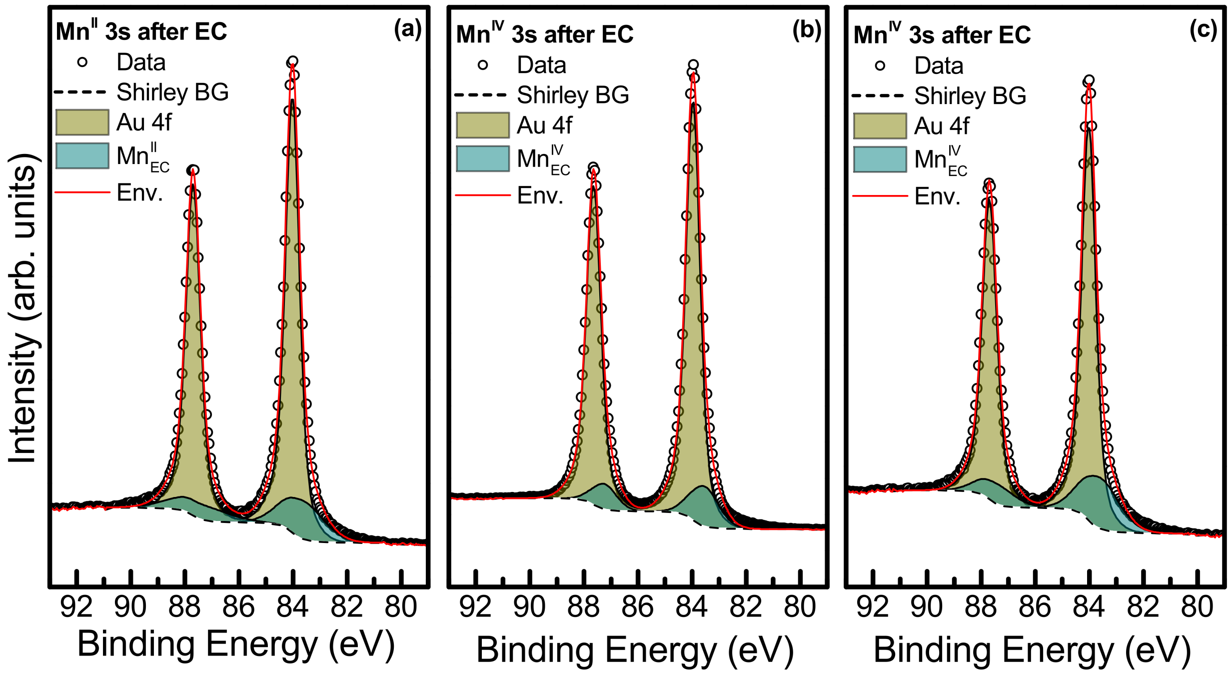

Figure 7.14: XP detail spectra of Mn core level peak Mn 3s after EC in a BE range of 79 to 93 eV. MnO$_x$ samples deposited on Au with the main oxidation phase of Mn$^{II}_{EC}$ (a), Mn$^{III}_{EC}$ (b), and Mn$^{IV}_{EC}$ (c) are displayed. The spectrum is subtracted with a Shirley BG, the peaks are deconvoluted with line shape curves to obtain the gold core level Au 4f (dark yellow) and GL curves for Mn 3s region (dark cyan).

Table 7.7: Raw area values and corrected Area values A_{corr} determined with XPS, evaluated for the core level peaks Mn 3p and O 1s. The correction has been done in regard to the SF, *T*, and IMFP values directly with CasaXPS.

Sample	Raw A(Mn 3p)	A_{corr}(Mn–O/OH)	Raw A(O 1s)	A_{corr}(O–Mn)	A_{corr}(HO–M)	A_{corr}(O–C/H_2O)
Mn$^{II}_{EC}$	4470.36	3293.39	24103.07	7612.61	1679.52	214.37
Mn$^{III}_{EC}$	4763.19	3509	31080.26	9486.14	2146.82	624.97
Mn$^{IV}_{EC}$	5063.23	3729.85	30489.47	7248.01	4685.61	91.75

LBEP in the Mn 2p region at a BE lower than 642 eV which is most prominent in obtained Mn 2p$_{3/2}$ peak of the Mn$^{II}_{EC}$ sample in figure 7.13. Stoichiometric evaluation of this theory is close to impossible, since the amount of K_2MnO_4 can hardly be estimated due to the anyway unclear shape of the Mn 2p$_{3/2\ peak}$, along with the low resolution of the K 2p$_{3/2}$ peak in the spectrum which forbids evaluation of the K–OH and corresponding K–O–Mn species.

Considering K_2MnO_4 on the sample with 100 % of present potassium being involved, Mn$^{II}_{EC}$ would exhibit a Mn(OH)$_2$ concentration of 25.4 % along with a Mn/O ratio of 0.37, being very close to Mn$^{III}_{EC}$ in regard to the metal hydroxide content, but still revealing unclear stoichiometry when it comes to the manganese to oxide ratio.

However, the presence of K_2MnO_4 lowers the calculated amount of KOH, resulting in higher values for Mn(OH)$_2$ and MnO$_x$. In K_2MnO_4, manganese occurs as Mn^{VI}, giving rise to lower values on the ΔE3s splitting. On the other hand, Mn^{III} species are reported to form a peak shoulder at *ca.* 641 eV. Since the obtained shoulder is not clearly a discrete peak, this possibility has to be considered, also with respect to the assumed main phase of Mn_3O_4 due to the obtained ΔE2p$_{1/2}$ splitting.

In Mn$^{III}_{EC}$ and Mn$^{IV}_{EC}$ the obtained ratios are 0.27 and 0.22, respectively. A ratio of 0.25 is consid-

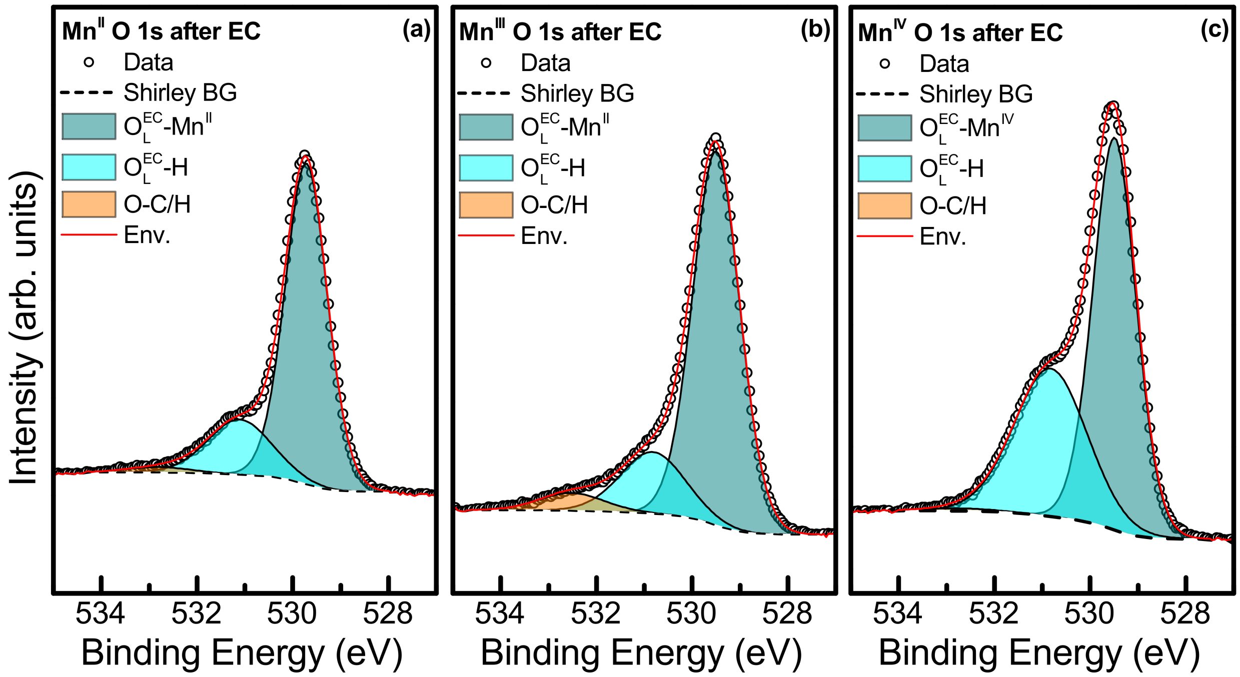

Figure 7.15: XP detail spectra of oxygen core level peak O1s after EC in a BE range of 527 to 535 eV. MMn$^{II}_{EC}$ (a), Mn$^{III}_{EC}$ (b), and Mn$^{IV}_{EC}$ (c) are displayed. The spectrum is subtracted with a Shirley BG, the peaks are deconvoluted with GL curves to obtain the surface oxygen bound to Mn in the main phase (dark cyan) and in a minor phase (olive), as well as oxygen vacancies (purple).

Table 7.8: Raw area values and corrected Area values A_{corr} determined with XPS, evaluated for the core level peaks K 2p$_{3/2}$ to subtract the amount of KOH of the OH species in the O 1s region. The correction has been done in regard to the SF, *T*, and IMFP values directly with CasaXPS.

Sample	Raw A(K 2p$_{3/2}$)	A_{corr}(K 2p$_{3/2}$)	A_{corr}(HO–Mn)
Mn$^{II}_{EC}$	3160.88	1532.69	146.83
Mn$^{III}_{EC}$	535.68	259.74	1887.08
Mn$^{IV}_{EC}$	716.07	345.68	4339.93

ered, resulting in the assumption of MnO$_4$ clusters. K$_2$MnO$_4$ is not considered on these samples due to the low amount of potassium detected in the K 2p region.

7.4 Raman Spectroscopy of MnO$_x$

While XPS usually is a powerful tool to investigate the structure of amorphous thin films, this is peculiar difficult for MnO$_x$ due to the various results in literature regarding the correlation of E_{BE} and oxidation state. The main phase of the catalysts was determined with XPS without a clear statement towards the side phases present. Therefore, SER spectra were recorded on the as deposited films on Au$_{etch}$.

The recording of Raman spectra was described detailed in section 4.7. They were acquired with respect to observations in literature regarding the thermal reduction of higher oxidized MnO$_x$. Mn$_2$O$_3$ is described as one of the most sensitive MnO$_x$ towards thermal decomposition due to irradiation with laser light. Therefore, the sample was illuminated with the highest available ND filter to tune the intensity of the laser beam to *ca.* 0.1 mW, recalling that Mn$_2$O$_3$ was observed to be stable at 1 mW of 633 nm irradiation [87].

The RS spectra of the dry catalysts were recorded within *ca.* 10 min after contact with atmosphere to prevent atmospheric oxidation. Figure 7.18 displays the results of these measurements. In CasaXPS, the obtained spectra were subtracted with a cubic

Table 7.9: Corrected peak area values A_{corr}, determined with XPS, evaluated based on the manganese core level peak Mn 3p and the oxygen core level peak O 1s. A_{corr}(Mn−OH) has been calculated by dividing A_{corr}(O−H) by 2, A_{corr}(Mn−O), by subtracting A_{corr}(O−H) of A_{corr}(Mn−OH).

Sample	A_{corr}(Mn−O/OH)	A_{corr}(Mn−OH)	A_{corr}(Mn−O)	c(Mn(OH)$_2$) (%)	Mn−O/O−Mn
Mn^{II}_{EC}	3293.39	73.42	3219.97	2.23	0.42
Mn^{III}_{EC}	3509	943.54	2565.46	26.89	0.27
Mn^{IV}_{EC}	3729.85	2169.97	1559.88	58.18	0.22

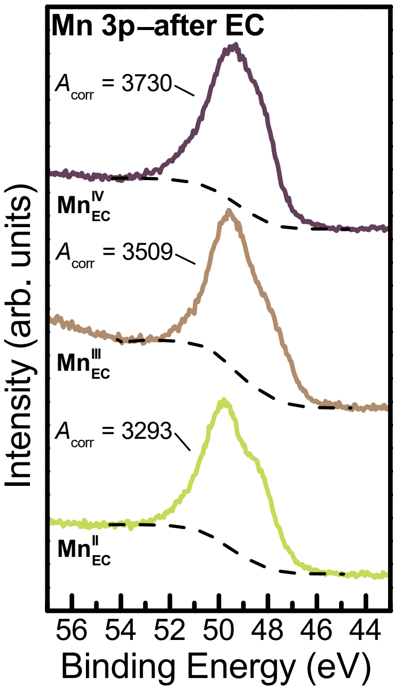

Figure 7.16: XP detail spectra of Mn core level peak Mn 3p after EC in a BE range 43 to 57 eV. Mn^{II}_{EC} (chartreuse), Mn^{III}_{EC} (khaki), and Mn^{IV}_{EC} (maroon) are displayed. The regions are subtracted with a Shirley BG and the peak areas A_{corr}, corrected for the sensitivity factor SF, transmission factor T, and inelastic mean free path IMFP, are given.

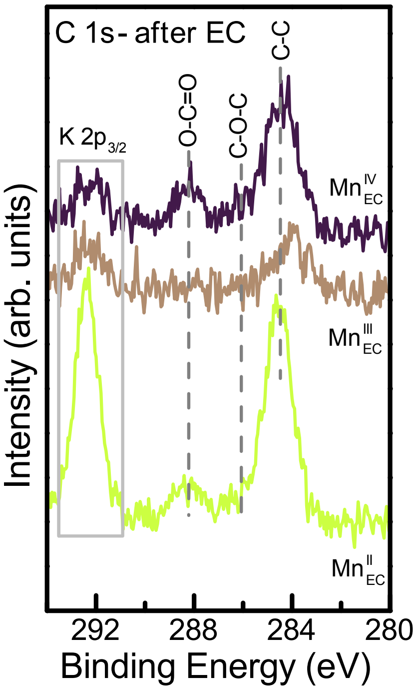

Figure 7.17: XP detail spectra of carbon core level peak C 1s after EC in a BE range 280 to 294 eV; Mn^{II}_{EC} (chartreuse), Mn^{III}_{EC} (khaki), and Mn^{IV}_{EC} (maroon) are displayed.

spline to remove the fluorescent BG, normalized to the highest peak, and fitted with Lorentzian curves, considering two adjusting parameters, the intensity and the FWHM.

A correlation of the RS spectra of MnO_x and the polymerisation degree, described by the edge-sharing of MnO_6 octahedra, was found by Julien *et al.* [83]. Generally, a Raman spectrum is characterized by two distinct, relatively intense marker modes, describing the A_g Mn−O vibrations in a MnO_6 octahedra, shifting based on the edges shared per octahedra. The highest Raman shift is observed for β-MnO_2, sharing two edges per MnO_6, the lowest in MnO with eight edges shared [83]. In manganese dioxides, these modes are denoted as $A_g(1)$ and $A_g(2)$ in accordance with An *et al.* [94], who attributed these vibrational modes to the motion of oxygen parallel and perpendicular to the basal plane.

MnO: The SER spectrum of MnO in figure 7.18a reveals two intense peaks at 569 and 659 cm^{-1} with a medium feature overlapping in between at 619

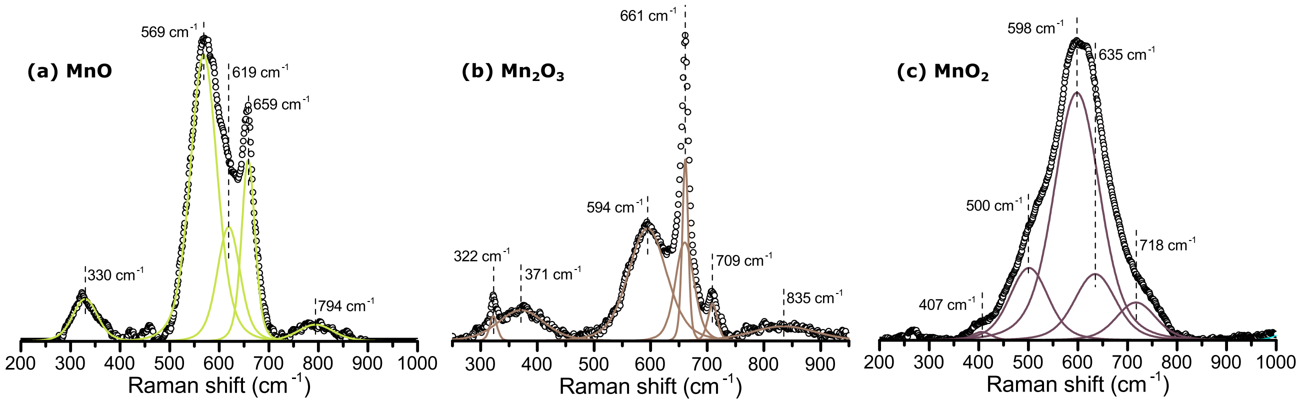

Figure 7.18: SER spectra of the as deposited MnO_x right after deposition. The figure displays MnO from 200 to 1000 cm^{-1} (a), Mn_2O_3 from 250 to 950 cm^{-1} (b), and MnO_2 from 200 to 1000 cm^{-1}. The spectra were subtracted with a cubic spline to remove fluorescence, normalized, and fitted with Lorentzian curves. The wavenumbers of the corresponding vibrational features is given.

cm^{-1}. Two weaker peaks are located at 330 and 794 cm^{-1}. The strongest peak at 569 cm^{-1} is attributed to the A_g Mn–O stretching mode of the Mn^{II} cations [83]. Compared to other MnO_x the low wavenumber of this peak arises due to the high amount of shared edges of the MnO_6 octahedra. In 99.9 % MnO powder, this peak is located at 531 cm^{-1}, indicating low long-range order in the amorphous films and presence of higher coordinated MnO_6 octahedra in the film.

The vibrational modes at 619 cm^{-1} (lit.: 591 to 595 cm^{-1}) and 659 cm^{-1} (lit.: 645 to 654 cm^{-1}) are also assigned to MnO [83, 86]. The high wavenumber band at 794 cm^{-1} can not be associated with low coordinated MnO_6 octahedra, since the highest reported wavenumber for this is 750 cm^{-1} such as in β-MnO_2 [83]. It is therefore attributed to ν(O–O) surface peroxo species that occur in the 750–920 cm^{-1} region [140]. The 330 cm^{-1} mode arises due to an overlap of a weak MnO signal and two overlapping signals at *ca.* 315 and 370 cm^{-1}, a contribution of higher oxidized MnO_x, as bands in this region arise for Mn_3O_4 and Mn_2O_3 [86]. These species contribute unclearly to the feature at *ca.* 650 cm^{-1}. The very weak signal between 400 to 500 cm^{-1} (lit.: 485 cm^{-2} in Mn_3O_4) further supports previous assumptions regarding the observed side phase [86].

Mn_2O_3: The RS spectrum of Mn_2O_3 in figure 7.18b is dominated by two overlapping bands at 660/661 cm^{-1} and a broad peak at 594 cm^{-1}. Smaller features are observed at 322, 371, 709 and 835 cm^{-1}.

The peak at 594 cm^{-1} is seen as the characteristic in-plane Mn–O stretching mode of α-Mn_2O_3. The spectrum of α-Mn_2O_3 in literature reveals a striking three band profile at 594, 661 (with bigger FWHM), and 709 cm^{-1} (lit.: 592,645, and 698 cm^{-1}), along with a signal at 322 cm^{-1} (lit.: 314 cm^{-1}) [83]. The additional narrow peak at 661 cm^{-1} is attributed to Mn_3O_4, also giving rise to the broad feature at 371 cm^{-1} (lit.: 365 to 374 cm^{-1}) and a small vibrational mode at *ca.* 485 cm^{-1} (not deconvoluted), resulting in a high FWHM of the α-Mn_2O_3 in-plane Mn–O stretching mode at 594 cm^{-1} [86].

The formation of Mn_3O_4 on the sample is not expected to occur under the laser light, but much more due the annealing of the sample for 1 h at 600 °C in Ar atmosphere before. The Mn_3O_4 peak at 648 to 659 cm^{-1} is characteristic for spinel structures, corresponding to the Mn–O breathing vibration of manganese ions in tetrahedral coordination, involving motion of oxygen atoms only [83]. The small but broad band at 835 cm^{-1} is again associated with an O–O stretching mode of surface oxygen [140]. The shift to higher wavenumbers compared to MnO is due to higher bond order (leading to lower bond distance) between the oxygen atoms in Mn_2O_3 [140].

MnO_2: Three main marker peaks are visible in the SER spectrum of MnO_2 in figure 7.18c, the most intense at 598 cm^{-1}, accompanied by two medium bands at 500 and 635 cm^{-2}, and smaller signals at 407 cm^{-1} and 718 cm^{-1}. As we know from XPS, the main phase present is in fact MnO_2, along with a small amount of other oxidized MnO_x species, there are still at least six modifications possible for MnO_2 to form a solid film. The deconvoluted three marker modes at *ca.* 500 cm^{-1}, *ca.* 570–590 cm^{-1}, and *ca.* 630–650 cm^{-1} are characteristic for manganese dioxides, and more precise attributed to δ-MnO_2 [86, 172]. The 598 cm^{-1} peak corresponds to the in-plane Mn−O stretching vibration ($A_g(1)$), and the two bands at 500 and 635 cm^{-1} to the out of plane Mn−O vibration ($A_g(2)$) of the MnO_6 octahedra [172, 94].

The previously considered β-MnO_2 is not present here due to the missing intense peak at *ca.* 660 cm^{-1}. The synthetic spinel type γ-MnO_2 has a only one sharp feature at 596 cm^{-1} and no additional peak above 646 cm^{-1} [83]. However, γ-MnO_2 exists with β-MnO_2 intergrowth, revealing a $A_g(1)$ marker band at *ca.* 572 [173]. As stated above, the main modes at 598 and 635 cm^{-1} belong to the Mn−O stretching vibration of the MnO_6 octahedra and depend on the average number of shared edges. The SER spectral resolution is not sufficient to state a clear modification of MnO_2, in fact, it is likely for the sputtered layers to reveal several combinations of manganese dioxide. Only three mineral manganese dioxides contain RS modes above 700 cm^{-1} (nsutite, romanechite, and birnessite), and deduced from the general shape of the SER spectrum, δ-MnO_2 is most likely [83].

δ-MnO_2 (synonym of the mineral birnessite) consists of layers of MnO_6 octahedra with a vacancy in every sixth site, containing more or less hydrated Mn^{III} cations [83]. The presence of Mn^{III} in MnO_2 is known to greatly enhance the catalytic activity [174]. Chan *et al.* [172] stated the remaining presence of Mn^{III} in OER active films along with a lowering of the Mn−O bond coordination number. Further, the three major modes of δ-MnO_2 are not fixed and differ based on the amount of vacancies in the MnO_6 octahedra, and the out of plane Mn−O mode above 630 cm^{-1} was reported to blue shift based on the amount of point defects [173, 94].

7.5 *Operando* Raman Spectroscopy of MnO_x

Thin films of MnO_x have been studied under working condition in 0.1 M KOH in a potential range relevant to the OER. After being mounted in the *in situ* Raman cell, the catalyst were cycled 50 times at 1.0 to 1.5 V *vs.* RHE with 100 $mV\,s^{-1}$ for surface conditioning. Afterwards, a potential of 1.0 V *vs.* RHE was applied for at least 10 min to reach a stabilized surface conditioned (monitored by CA). For *operando* measurements, the potential was increased in 0.05 V steps towards 1.70 V *vs.* RHE, holding the potential for 5 to 10 min before applying Raman spectroscopy. The discussed spectra in this chapter are the average of 20 measurements with 3 to 5 s irradiation time (see section 4.7 for details).

All *operando* spectra of the respective MnO_x phases are displayed in figure 7.19, along with deconvoluted spectra at 1.10 and 1.70 V *vs.* RHE beneath for detailed comparison of band shifts. All spectra have been subtracted with a cubic spline to remove the fluorescent background, and have been normalized to the highest peak. The *operando* spectra are stacked, and the most important bands are indicated by vertical dotted lines. To address the observed activity changes after reduction at 0.8 V *vs.* RHE, to MnO and Mn_2O_3 CA has been applied for 30 min at the same *E*. The deconvolution of the recorded spectra are presented in figure 7.20 and

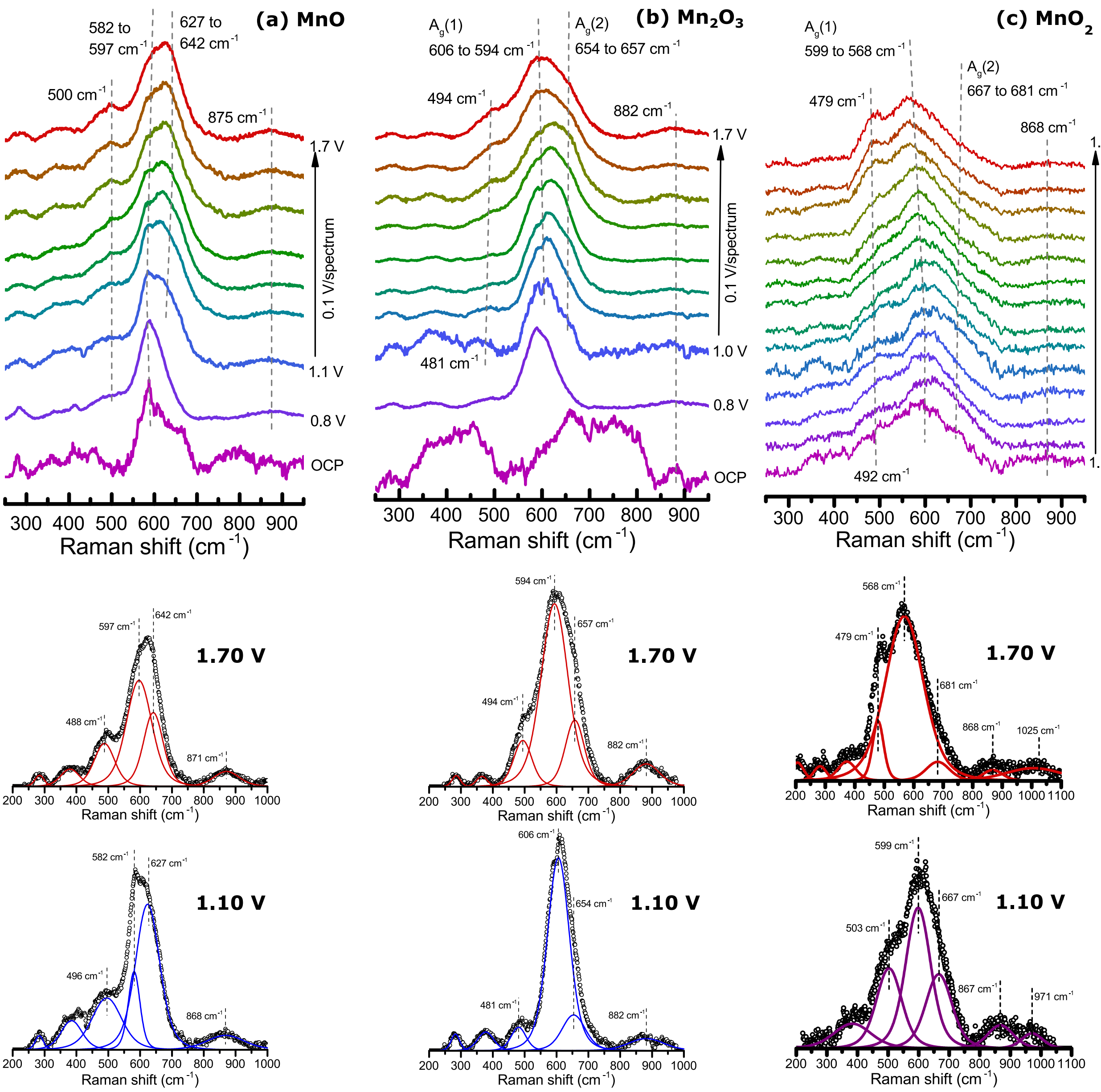

Figure 7.19: SER spectra MnO_x under working condition. The figure displays (a), Mn_2O_3 (b), and MnO_2 (c) from 250 to 950 cm^{-1}. The spectra were subtracted with a cubic spline to remove fluorescence, normalized, and deconvoluted with Lorentzian curves for 1.10 and 1.70 V *vs.* RHE below the stacked graphs. The wavenumbers of the corresponding vibrational features is given.

shall be discussed at given time in the following sections.

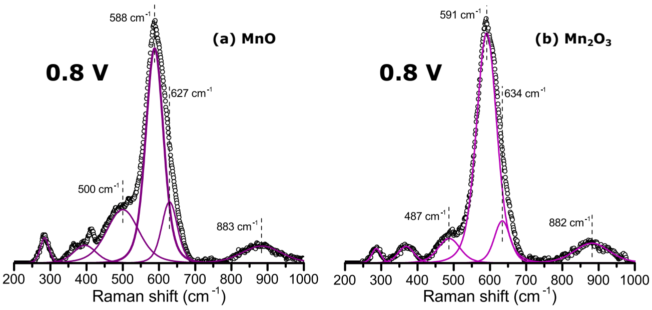

Figure 7.20: SER spectra MnO_x at 0.8 V *vs.* RHE. The figure displays (a), Mn_2O_3 (b), and MnO_2 (c) from 250 to 950 cm^{-1}. The spectra were subtracted with a cubic spline to remove fluorescence, normalized, and deconvoluted with Lorentzian curves for 1.10 and 1.70 V *vs.* RHE below the stacked graphs. The wavenumbers of the corresponding vibrational features is given.

MnO: The spectra in figure 7.19a displays the deposited Mn^{II} phase under working condition. A spectrum at the OCP has been recorded, revealing a prominent $A_g(1)$ peak at 587 cm^{-1}, along with additional peaks at *ca.* 608 and 661 cm^{-1}, resulting in similar structure as the dry MnO sample. The intense 608 cm^{-1} mode is shifted to 582 cm^{-1} at 1.1 V *vs.* RHE, continuously shifting further to 597 cm^{-1} at increasing E, as revealed by the corresponding deconvolution. In the *operando* spectra a feature arises steadily with higher potentials at *ca.* 500 cm^{-1}. Deconvolution presents this peak at 496 cm^{-1} at 1.1 V *vs.* RHE, slightly shifting to 488 cm^{-1} at 1.7 V *vs.* RHE.

At 1.1 V *vs.* RHE, the $A_g(1)$ mode is located at 582 cm^{-1}, along with a newly arised mode at 627 cm^{-1}, attributed to the $A_g(2)$ mode, indicating MnO_2 type formation. Until *ca.* 1.4 V *vs.* RHE, this mode shifts towards 642 cm^{-1}, as it was reported to occur in δ-MnO_2 type structures, illustrating a charging process of the catalyst, *i.e.* the introduction of point defects [94]. An additional RS feature is present at 868 to 875 cm^{-1}, staying more or less constant over the presented E range. On as deposited MnO and at zero applied potential, ν(O−O) was found at *ca.* 794 cm^{-1}, therefore the structure change towards a MnO_2 type gives rise to higher oxygen bond orders [140]. Consequently, the suspected peroxo species in this range are not influenced by an applied E, indicating no further crystal-like structural change.

Figure 7.20a presents the reduced species after 30 min at 0.8 V *vs.* RHE, revealing a strong mode at 588 cm^{-1}, along with two medium RS features at 500, 627, and 883 cm^{-1}. The overall location of the vibrational bonds suggests MnO_2 type of the catalyst with very weak $A_g(2)$ vibration. The ongoing *operando* spectra at 1.1 to 1.7 V *vs.* RHE are unaffected by the reduction process and are therefore not shown here. Due to this observation, a change of the surface structure towards a hexagonal (1 × ∞) layered structure at potentials above 1.0 V *vs.* RHE is stated, giving rise to the $A_g(2)$ vibration attributed to oxygen perpendicular to the basal plane [83, 94].

Mn_2O_3: The OCP spectrum of Mn_2O_3 in figure 7.19b has very low Raman intensity, observed due to the high BG noise. Deconvolution of the spectrum reveals at least two overlapping features of similar intensity at *ca.* 383 and 458 cm^{-1}, two overlapping bands at *ca.* 663 and 751 cm^{-1}, and a O−O stretching mode at 881 cm^{-1}. The spectrum was probably recorded during a phase transformation from the deposited α-Mn_2O_3 towards a MnO_2 type structure, as a new feature arises at 458 cm^{-1} and above 700 cm^{-1}.

At 1.1 V *vs.* RHE, the main $A_g(1)$ peak is located at 606 cm^{-1}, accompanied by a weaker $A_g(2)$ feature at 654 cm^{-1}, along with three weak signals at 284, 377, and 481 cm^{-1}, as well as a ν(O−O) mode at 882 cm^{-1}. Based on the observed bands, a δ-MnO_2 structure is concluded as main phase [172]. The slightly shifted $A_g(1)$ peak is suspected to rise above 600 cm^{-1} at lower E due to an influence of the as deposited α-Mn_2O_3 structure and their main feature at higher wavenumbers.

With rising E, the $A_g(2)$ mode at $654\,cm^{-1}$ smears out and ends at $657\,cm^{-1}$ at 1.7 V *vs.* RHE. The $A_g(1)$ mode red-shifts slightly to $594\,cm^{-1}$, indicating higher distances between the MnO_6 layers in δ-MnO_2 [175]. The shoulder at $481\,cm^{-1}$ visibly rises and blue-shifts to $494\,cm^{-1}$. Due to the overall peak locations at 1.7 V *vs.* RHE, the catalyst reveals a δ-MnO_2 structure with $A_g(2)$ location well above MnO at all potentials, indicating already charged structure of the catalyst [94]. The introduction of point defects during the charging mechanism creates Mn^{III} species that are already present on the deposited α-Mn_2O_3.

The ν(O−O) band remains constant at $882\,cm^{-1}$ but rises relatively to the other vibrational features, further lying at higher wavenumbers than the δ-MnO_2 formed by MnO at 1.7 V *vs.* RHE ($871\,cm^{-1}$), indicating higher bond order of the peroxo species [140].

The reduced α-Mn_2O_3 at 0.8 V *vs.* RHE in figure 7.20b has similar shape as the MnO sample at the same E. The main peaks is present at $591\,cm^{-1}$, accompanied by smaller bands at 487 and $654\,cm^{-1}$, along with the peroxo feature at $882\,cm^{-1}$. Compared to MnO, the peak locations vary in maximum $13\,cm^{-1}$, and the 487 and $654\,cm^{-1}$ peaks reveal less intensity relative to the main $A_g(1)$ mode. Since the $A_g(2)$ of the δ-MnO_2 formed by α-Mn_2O_3 shifts only $+3\,cm^{-1}$, no additional point defects are expected to be introduced in the structure.

MnO_2: The MnO_2 sample at 1.1 V *vs.* RHE (see figure 7.19c) has a very broad main feature at $610\,cm^{-1}$ that consists out of two overlapping peaks located at 599 and $667\,cm^{-1}$, corresponding to the $A_g(1)$ and $A_g(2)$ modes of δ-MnO_2. At *ca.* 1.25 V *vs.* RHE the $610\,cm^{-1}$ peak splits visibly and a shoulder arises at $681\,cm^{-1}$, while the $A_g(1)$ mode red-shifts towards $568\,cm^{-1}$ at 1.7 V *vs.* RHE. The vibrational mode at $492\,cm^{-1}$ rises at a similar E, creating a distinct feature at $479\,cm^{-1}$ until 1.7 V *vs.* RHE.

Two ν(O−O) stretching modes are visible, first located at 867 and $971\,cm^{-1}$, along with shifting of the higher mode to $1025\,cm^{-1}$ at 1.7 V *vs.* RHE. As a consequence, two types of peroxo species are suspected on the catalyst with differing bond order [140].

By comparison of the deconvoluted spectra, there is no visible structural change in the deposited MnO_2 sample in a potential range of 1.0 to 1.7 V *vs.* RHE, but a charging mechanism due to an estimated peak shift of $+14\,cm^{-1}$. Additionally, the charging cause the peroxo species at higher wavenumebrs to smear out and blue-shift. Additionally, the red-shift of $A_g(1)$ is associated to the weakening of the interaction between MnO_6 octahedra due to expansion of interplanar spacing [175].

7.6 Permanent Structural Changes after EC Investigated by Raman Spectroscopy

After having performed *operando* spectroscopy on the samples, they were rinsed thoroughly with millipore water and investigated once more *ex situ* under the Raman microscope. For each sample, the parameters were set to the exact same settings as the corresponding inspection of the as deposited MnO_x.

The resulting spectra are depicted in figure 7.21. The high fluorescent BG was removed with a cubic spline and the resulting spectra normalized to the highest vibrational mode. Lorentzian curves were used to deconvolute molecular peaks.

The MnO sample after EC (figure 7.21a) reveals four very similar vibrational features, two strong at 595 and $651\,cm^{-1}$, and two weak signals at 331 and $489\,cm^{-1}$, indicating MnO_2 shape. The overall shape with a higher intensity peak at *ca.* $600\,cm^{-1}$, coupled with a lower intense peak at *ca.* $650\,cm^{-1}$, along with a weak feature *ca.* $500\,cm^{-1}$ is characteristic for δ-MnO_2 [83]. The $331\,cm^{-1}$ may arise due to residual lower oxidized MnO_x species (Mn_3O_4/Mn_2O_3) that also contributes to the *ca.* $650\,cm^{-1}$ peak deconvoluted. These features

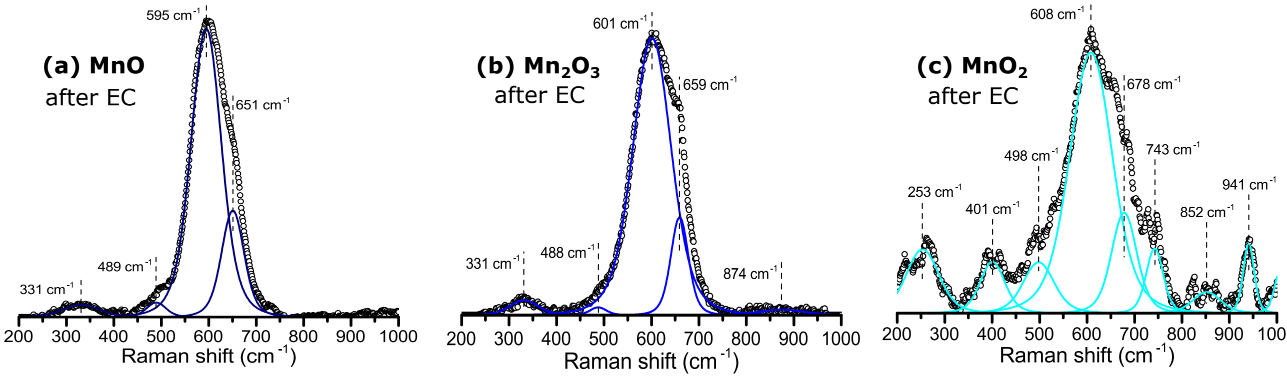

Figure 7.21: SER spectra of MnO_x after EC. The figure displays MnO (a), Mn_2O_3 (b), and MnO_2 from 200 to 1000 cm^{-1}. All spectra were subtarcted with a cubic spline to remove fluorescence, normalized to the highest peak, and fitted with Lorentzian curves. The wavenumbers of the corresponding vibrational features are given.

are residuals of the deposition and not converted towards δ-MnO_2 during EC.

Similar RS pattern is visible in Mn_2O_3 (figure 7.21b) with two strong modes at 601 and 659 cm^{-1}, and weak bands at 331 and 448 cm^{-1}. Additionally, Mn_2O_3 has a O–O stretching mode at 874 cm^{-1} from residual surface or intercalated oxygen. Again, the 331 cm^{-1} is attributed to lower oxidized MnO_x.

As it is observed by the amount of peaks assigned in MnO_2 after EC, the sample classification towards one MnO_2 type is rather difficult. Also, the Raman activity is relatively low compared to the other samples after EC. The main δ-MnO_2 peaks are visible at 498, 608, and 678 cm^{-1}, but the 331 cm^{-1} of the previously discussed MnO_x is missing. Residual species that arise at this wavenumber occur therefore as a consequence of the deposition of Mn^{II} and Mn^{III}. Instead, at 253 cm^{-1}, one weak band arises probably due to the overlap of two vibrations at *ca.* 221 and 265 cm^{-1}, along with a new feature at 401 cm^{-1}, that was already observed in the as deposited MnO_2 in figure 7.18c. The RS spectrum shows indication of additional vibrations at *ca.* 534 and 654 cm^{-1}. Along with the 743 cm^{-1} vibration, a mixture of δ-MnO_2 and β-MnO_2 is concluded for this sample [173, 87].

Peroxide species in MnO_x

In the operando spectra of MnO_2 in figure 7.19c, splitting of the ν(O–O) mode was observed above 1.0 V *vs.* RHE, and is still visible after EC in the two peaks at 852 and 941 cm^{-1}. The O–O species are classified as peroxo due to their occurrence below 1100 cm^{-1} [140].

In transition metal complexes, the ν(O–O) vibration of peroxo complexes lying in the 800 to 900 cm^{-1} region, exhibits side-on structure, describing the coordination of two oxygen and one metal atom in triangular formation. The ν(O–O) vibration in FeO_2 is reported at 946 cm^{-1} and is rather good comparable to MnO_2, since ν(O–O) shifts based on the electron affinity of the metal cation and reveals no designated M–O vibration for this complex [176, 140]. The additional bond is expected to occur based on the two different MnO_2 type structure of the catalyst. Therefore, the ν(O–O) band below 900 cm^{-1} is assigned to the δ-MnO_2 structure and the ν(O–O) vibration above 900 cm^{-1} to surface oxygen of β-MnO_2.

The *operando* spectra of MnO and Mn_2O_3 were classified as δ-MnO_2 type structures, showing the ν(O–O) vibration at wavenumbers from 868 to 882 cm^{-1}. In contrast, the dry samples revealed these peaks at lower wavenumbers of 794 and 835 cm^{-1}, further supporting previous assumption.

Based on the crystal structure, the peroxide in β-MnO_2 may be present due to intercalated H_2O in the (1 × 1) tunnels of the structure [83]. The shrinking of the high region peroxo peak in MnO_2 is attributed to a phase vanishing during OER, such as an unclear manganese dioxide sidephase that was not clearly assigned to in the inspection of the dry sample.

7.7 Structure-Activity Correlation of MnO_x

In a potential range of 1.0 to 1.7 V *vs.* RHE, all investigated MnO_x revealed MnO_2 character, based of the results obtained by *operando* Raman spectroscopy. An overall scheme of the MnO_x processes in alkaline media is illustrated in figure 7.22. The location of the RS features and the nature of aqueous media suggest δ-MnO_2 type for all samples, according to all previously discussed literature references.

With obtained SER spectra of MnO_x under working condition, one can rule out the OER mechanism present in NiO_x, that considers oxidation towards oxyhydroxides at given potentials, since no Mn−OOH or superoxide vibration was observed on the catalysts. Further, the results support the observations of An *et al.* [94], respecting a charging of δ-MnO_2, resulting in a triclinic to hexagonal structure transformation and the formation of point defects, that introduce Mn^{III} in the sample.

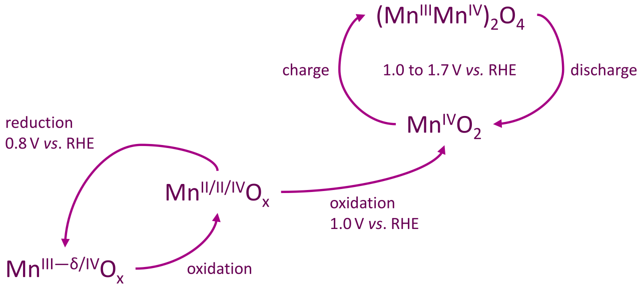

Figure 7.22: Scheme of redox and phase transformation processes of thin film MnO_x in alkaline media.

The layered δ-MnO_2 consists of layers of MnO_6 octahedra with layers of H_2O in between. The structure transformation, *i.e.* charging of δ-MnO_2, is different for all catalysts, based on the shift of the $A_g(2)$ mode to higher wavenumbers at an applied voltage. The shift during rising potential can directly be correlated to the oxidation observed for MnO_x in figure 7.7a (CV of MnO_x). On Mn_2O_3, almost no activation of the catalyst was observed as current response in EC, and during *operando* Raman, the $A_g(2)$ mode only shifts ca. $+3\,cm^{-1}$. A more pronounced oxidation wave is observed for MnO along with a peak shift of $+15\,cm^{-1}$ results in an earlier O_2 evolution onset.

The highest current response is revealed by MnO_2 from 1.0 to 1.5 V *vs.* RHE, giving rise to a peak shift of $+14\,cm^{-1}$ in this potential range. The higher current at lower *E* is correlated to the already present MnO_2 structure, while other catalysts reveal parasitic MnO_x species in the *in situ* Raman spectra at 1.1 V *vs.* RHE. The splitting ν(O−O) in the charging process observed in MnO_2 remains unclear and might occur due to a vanishing side phase such as β-MnO_2 during EC.

At this point it is stated, that stability measurements of the MnO_x have not been successful at a relevant *E* above O_2 evolution. The continuous bubbling of the solution prevented recording of spectra after *ca.* 15 to 20 min, based on the applied voltage. Long time measurements, to address all the structural changes occurring during long-time cycling could not have been achieved in this thesis. In the EC results presented in figure 7.8, the change of activity of MnO_x based on the deposited sample was monitored. While the reduction process was retraced with Raman spectroscopy, the activation and the reactivation up to 1.7 V *vs.* RHE can not be simulated in the *in situ* cell due to bubbling. The sample has to be activated/reactivated in the Zahner-cell and monitored afterwards *operando* to further investigate the OER mechanism and gain insight on the high performance MnO_x that was achieved during reactivation.

With up to date modelling, hausmannite-like Mn_3O_4 intermediates can be used to introduce Mn^{III} that is specifically active towards the OER. It is therefore suspected, that the reduction at 0.8 V *vs.* RHE after partly oxidation of deposited Mn^{II} is most pronounced to form these Mn^{III} species, either due to redox processes during cycling in alkaline media, or due to the present Mn_3O_4 species after deposition. However, these are also present in deposited Mn^{III}, and no improvement of the catalytic performance was observed here. The mechanism remains unclear, and further *operando* studies have to be performed to develop a solid model.

The degree of charging of δ-MnO_2 depends on the deposited MnO_x species. Deposition of Mn^{II} results in moderate charging, based on the $+15\,cm^{-1}$ shift of the $A_g(2)$ band until *ca.* 1.4 V *vs.* RHE. Mn^{III} species reveal charged character already at 1.1 V *vs.* RHE and only blue-shift *ca.* $+3\,cm^{-1}$ until 1.7 V *vs.* RHE. The $A_g(2)$ mode in deposited Mn^{IV} shifts to highest wavenumbers ($+14\,cm^{-1}$), resulting in the lowest η at 0.1 and 5 $mA\,cm^{-2}$. While the charging shift remains present *ex situ*, MnO_x can be discharged at $E = 0.8\,V$ *vs.* RHE reversible.

Further, the XPS and Raman results after EC can be correlated. The amount of lattice bound hydroxide (O_L–H) species was found to differ in XPS. With Raman spectroscopy, the peroxide vibrations were attributed to surface oxygen or intercalated water in the δ-MnO_2 layers. MnO after EC only revealed traces of $Mn(OH)_2$ on the surface (*ca.* 2.2 %), and no peroxide vibration was present in the corresponding Raman spectrum. The amount of $Mn(OH)_2$ in Mn_2O_3 was calculated to *ca.* 26 & with XPS and a small band is detected in the corresponding Raman spectrum, wile MnO_2 had over 58 % of O_L–H present, revealing two clearly observable peaks for peroxides in the Raman spectrum. One has to keep in mind, that the Raman spectra were obtained after an EC(II) type measurement, while XPS was conducted after performing EC(I), addressing the surface changes after longer cycling time. Recording Raman spectra after EC(I) probably will give better insight towards correlation of the spectra.

8 Summary and Outlook

Towards the end of this thesis, key observations are given once more for the transition metal oxide systems NiO_x *and* MnO_x*. Final considerations will provide an outlook towards further research in the exciting field of catalysis operando studies.*

8.1 NiO_x

NiO_x was synthesized by reactive magnetron sputtering and studied in regard to the substrate and the deposition temperature. The species during deposition have found to be independent of the substrate used, in contrast to the sputtering temperature, where higher temperatures of 600 °C resulted in a defect-free NiO surface, proven by *in situ* XPS. During electrochemical measurements in 0.1 M KOH, an activity difference of the substrate was found and an enhancement of the OER activity attributed to Au support due to a charge transfer from Ni cations to highly electronegative Au. Au coated SS with deficient NiO_x exhibited an outstanding η of only 369 mV at $j = 10\,\text{mA}\,\text{cm}^{-2}$. Defect-free surfaces revealed higher η at $10\,\text{mA}\,\text{cm}^{-2}$ compared to deficient NiO_x. In a second XPS after EC, this behavior was attributed to the higher formation of $Ni(OH)_2$ during contact with the electrolyte and cycling duration on defect-free NiO_x surfaces.

The capacitive behaviour of NiO_x in regard to the substrate, deposition temperature, and cycling duration was studied in a potential region without faradaic processes. The capacitance was found to be up to 2 to 3 times higher for deficient NiO_x, decreasing with cycling duration due to the formation of $Ni(OH)_2$. $NiO^{RT}_{SS/Au}$ reached a capacitance of $457\,\mu\text{F}\,\text{cm}^{-2}$, decreasing to $416\,\mu\text{F}\,\text{cm}^{-2}$ after *ca.* 150 min of cycling. The temperature dependence of NiO_x was studied in detail on Au, revealing a steady decrease of capacitance with increasing deposition temperature. The higher the defect states on the surface, the less was the loss in capacitance during cycling.

Operando Raman spectroscopy was used to study the surface intermediates on NiO_x before and during O_2 evolution in alkaline media. With respect to the observations in this work, the former kinetic model of NiO_x electrocatalysts for the OER has been validated and further, the importance of deficient structures towards high activity/low overpotential due to the formation of both Ni^{II}/Ni^{III} and Ni^{III}/Ni^{IV} oxidation steps has been introduced. In contact with the electrolyte, the formation of $Ni(OH)_2$ is visible in the Raman spectra, further at potentials of 1.35 V *vs.* RHE the oxidation towards NiOOH, accompanied by Ni^{IV} species in a deprotonation step at *ca.* 1.5 V *vs.* RHE. The decreasing activity at defect-free surfaces was investigated and with Raman spectroscopy, a 10 times relatively lower deprotonation towards $NiOO^-$ was visible, being attributed as the active species in the OER for NiO_x.

8.2 MnO_x

MnO_x was deposited on Au with reactive magnetron sputtering, assigning the main oxidation state with XPS. EC was performed in 0.1 M KOH in different procedures, revealing the highest activity for Mn^{IV} with respect to the deposited phase. When applying several EC methods and cycling for longer time at higher potentials, the activity of all catalysts is enhanced, with severe improvements for the deposited Mn^{II} from 540 to 430 mV at $j = 5\,\text{mA}\,\text{cm}^{-1}$. The improvement of the catalysts was achieved with a 30 min reduction at 0.8 V *vs.* RHE and following reactivation between 1.0 to 1.7 V *vs.* RHE for 20 cycles.

The EDLC of the catalysts was investigated at a point, where very similar activity was achieved for all MnO_x. The highest intrinsic C_{dl} was revealed by Mn^{II} with 1379 $\mu F\,cm^{-2}$ due to high interaction of the surface species with the K^+ ions of the KOH electrolyte.

After EC, all samples revealed Mn^{IV} as their main species present as detected by XPS and Raman measurements. In the Raman spectra, however, the deposited Mn^{IV} showed not only birnessite, but also β-MnO_2 structure, as characterized by additional bands at 401, 743, and 941 cm^{-1}. This sample was found most active towards intercalation of H_2O, proven by XPS and Raman.

With *operando* Raman spectroscopy, the OER mechanism of MnO_x was investigated to address the difference in activity of the samples. All catalysts revealed δ-MnO_2 structure in a potential range relevant to the O_2 evolution, along with additional species suspected to occur from the deposition. The activity of the catalyst was directly correlated to the shift of the $A_g(2)$ mode, representing a charging process of the δ-MnO_2 structure and a triclinic to hexagonal phase transformation, introducing point defects that give rise to catalytic most active Mn^{III} species. The $A_g(1)$ mode shifted simultaneously to lower wavenumbers, which was associated with an increase in distance of the MnO_6 layers in δ-MnO_2.

8.3 Final Considerations

The literature is already full of studies on NiO_x and the $Ni^{II}/Ni^{III}/Ni^{IV}$ redox system. This thesis gave further insight into the importance of defect structures towards oxidation and the pleasing catalytic activity. However, studies here have not been performed in rigorously iron free KOH as most available literature suggests, so the influence of Fe in the presented mechanism can not be ruled out completely. Further investigation towards *in situ* studies regarding the NiO_x system should be considered in iron free KOH, to extinguish falsified results.

Further experiments towards the substrate dependence of the NiO_x activity are eligible. As presented in this work, the catalytic activity is enhanced with gold-support, but even more with gold-coated stainless steel. The research of present mechanism is desired, such as further conductivity measurements or interface studies.

A brief study on the OER mechanism of MnO_x has been performed. The present activity mechanism of charging and introduction of active Mn^{III} species is supported. In EC, it was possible to dramatically enhance the catalytic activity of MnO_x by a reduction/activation procedure, that was not possible to be retraced *in situ* due to intense bubbling at 1.7 V *vs.* RHE after short time. More studies are desirable towards this phenomenon, such as cycling *ex situ* and perform *operando* measurements thereafter. As given by the overview in figure 8.1 of the overpotential achieved by MnO_x based on the EC procedure, the conditioned samples were investigated by *operando* studies, with activation and reaction being of more interest towards future studies.

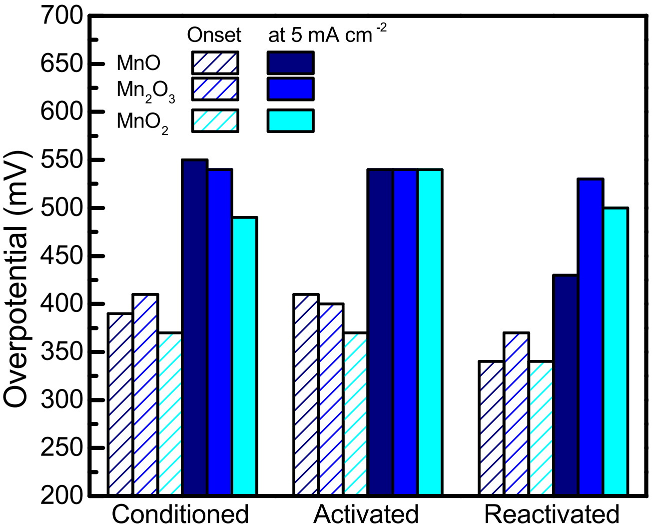

Figure 8.1: Overpotential of MnO_x based on the EC treatment. Conditioning is cycling 50 times from 1.0 to 1.5 V *vs.* RHE with 100 $mV\,s^{-1}$, activation is cycling 20 times from 1.2 to 1.7 V *vs.* RHE with 5 $mV\,s^{-1}$, and reactivation reduction at 0.8 V *vs.* RHE for 30 min, followed by the activation process.

The used procedure for surface enhancement has proven sufficient, and changing to longer wavelengths gave workable results, however, laser light above 700 nm is suspected to present even better results and reduce the high fluorescent background even more. It is also unclear, how the annealing step affects the studied structure of Mn^{III}. Investigation of a depositioning process at RT might be helpful to compare the results more reliable to the other MnO_x species.

References

[1] Mikael Höök and Xu Tang. *Depletion of fossil fuels and anthropogenic climate change—A review*. In: *Energy Policy* 52 (2013), pp. 797–809. ISSN: 03014215. DOI: 10.1016/j.enpol.2012.10.046.

[2] Fatima ezzahra Chakik, Mohammed Kaddami, and Mohammed Mikou. *Effect of operating parameters on hydrogen production by electrolysis of water*. In: *International Journal of Hydrogen Energy* 42.40 (2017), pp. 25550–25557. ISSN: 03603199. DOI: 10.1016/j.ijhydene.2017.07.015.

[3] Jun Chi and Hongmei Yu. *Water electrolysis based on renewable energy for hydrogen production*. In: *Chinese Journal of Catalysis* 39.3 (2018), pp. 390–394. ISSN: 18722067. DOI: 10.1016/S1872-2067(17)62949-8.

[4] A. Zuttel et al. *Hydrogen: the future energy carrier*. In: *Philosophical Transactions of the Royal Society A: Mathematical, Physical and Engineering Sciences* 368.1923 (2010), pp. 3329–3342. ISSN: 1476-4687. DOI: 10.1098/rsta.2010.0113.

[5] Ibrahim Dincer and Canan Acar. *Smart energy solutions with hydrogen options*. In: *International Journal of Hydrogen Energy* 43.18 (2018), pp. 8579–8599. ISSN: 03603199. DOI: 10.1016/j.ijhydene.2018.03.120.

[6] Serhiy Cherevko et al. *Oxygen and hydrogen evolution reactions on Ru, RuO 2 , Ir, and IrO 2 thin film electrodes in acidic and alkaline electrolytes: A comparative study on activity and stability*. In: *Catalysis Today* 262 (2016), pp. 170–180. ISSN: 09205861. DOI: 10.1016/j.cattod.2015.08.014.

[7] Bo Su, Zhi-Chao Cao, and Zhang-Jie Shi. *Exploration of earth-abundant transition metals (Fe, Co, and Ni) as catalysts in unreactive chemical bond activations*. In: *Accounts of chemical research* 48.3 (2015), pp. 886–896. DOI: 10.1021/ar500345f.

[8] Theodore L. Brown, Bruce Edward Bursten, and Harold Eugene LeMay. *Chemie: Studieren kompakt*. 10., aktualisierte Aufl. Always learning. München: Pearson, 2011. ISBN: 9783868941227.

[9] Dunfeng Gao et al. *Nanostructured heterogeneous catalysts for electrochemical reduction of CO 2*. In: *Current Opinion in Green and Sustainable Chemistry* 3 (2017), pp. 39–44. ISSN: 24522236. DOI: 10.1016/j.cogsc.2016.10.004.

[10] Jia Lu et al. *Metal Nickel Foam as an Efficient and Stable Electrode for Hydrogen Evolution Reaction in Acidic Electrolyte under Reasonable Overpotentials*. In: *ACS Applied Materials & Interfaces* 8.8 (2016), pp. 5065–5069. ISSN: 1944-8244. DOI: 10.1021/acsami.6b00233.

[11] Jian Zhang et al. *Efficient hydrogen production on MoNi4 electrocatalysts with fast water dissociation kinetics*. In: *Nature communications* 8 (2017), p. 15437. DOI: 10.1038/ncomms15437.

[12] Tung Ngoc Pham et al. *Robust hierarchical 3D carbon foam electrode for efficient water electrolysis*. In: *Scientific reports* 7.1 (2017), p. 6112. DOI: 10.1038/s41598-017-05215-1.

[13] Bert M. Weckhuysen. *Snapshots of a working catalyst: possibilities and limitations of in situ spectroscopy in the field of heterogeneous catalysis*. In: *Chemical Communications* 2 (2002), pp. 97–110. ISSN: 1359-7345. DOI: 10.1039/B107686H.

[14] Miguel A. Bañares et al. *Raman spectroscopy during catalytic operations with on-line activity measurement (operando spectroscopy): a method for understanding the active centres of cations supported on porous materials*. In: *J. Mater. Chem.* 12.11 (2002), pp. 3337–3342. ISSN: 0959-9428. DOI: 10.1039/b204494c.

[15] Vanesa Calvino-Casilda and Miguel A. Bañares. *Recent advances in imaging and monitoring of heterogeneous catalysts with Raman spectroscopy*. In: *Catalysis*. Ed. by James J. Spivey and Mayank Gupta. Vol. 24. Catalysis. Cambridge: Royal Society of Chemistry, 2012, pp. 1–47. ISBN: 978-1-84973-375-5. DOI: 10.1039/9781849734776-00001.

[16] M. Olga Guerrero-Pérez and Miguel A. Bañares. *From conventional in situ to operando studies in Raman spectroscopy*. In:

Catalysis Today 113.1-2 (2006), pp. 48–57. ISSN: 09205861. DOI: 10.1016/j.cattod.2005.11.009.

[17] S. Damyanova et al. *Thermal Behavior of 12-Molybdophosphoric Acid Supported on Zirconium-Loaded Silica*. In: *Chemistry of Materials* 12.2 (2000), pp. 501–510. ISSN: 0897-4756. DOI: 10.1021/cm9911316.

[18] Israel E. Wachs and Charles A. Roberts. *Monitoring surface metal oxide catalytic active sites with Raman spectroscopy*. In: *Chemical Society reviews* 39.12 (2010), pp. 5002–5017. DOI: 10.1039/C0CS00145G.

[19] Muhammad Tahir et al. *Electrocatalytic oxygen evolution reaction for energy conversion and storage: A comprehensive review*. In: *Nano Energy* 37 (2017), pp. 136–157. ISSN: 22112855. DOI: 10.1016/j.nanoen.2017.05.022.

[20] Jing Qi et al. *Porous Nickel-Iron Oxide as a Highly Efficient Electrocatalyst for Oxygen Evolution Reaction*. In: *Advanced Science* 2.10 (2015), p. 1500199. ISSN: 21983844. DOI: 10.1002/advs.201500199.

[21] Wence Xu and Hongxia Wang. *Earth-abundant amorphous catalysts for electrolysis of water*. In: *Chinese Journal of Catalysis* 38.6 (2017), pp. 991–1005. ISSN: 18722067. DOI: 10.1016/S1872-2067(17)62810-9.

[22] Hai-Yan Su et al. *Identifying active surface phases for metal oxide electrocatalysts: a study of manganese oxide bi-functional catalysts for oxygen reduction and water oxidation catalysis*. In: *Physical Chemistry Chemical Physics* 14.40 (2012), pp. 14010–14022. ISSN: 14639076. DOI: 10.1039/c2cp40841d.

[23] Isabela C. Man et al. *Universality in Oxygen Evolution Electrocatalysis on Oxide Surfaces*. In: *ChemCatChem* 3.7 (2011), pp. 1159–1165. ISSN: 1867-3880. DOI: 10.1002/cctc.201000397.

[24] J. Rossmeisl et al. *Electrolysis of water on oxide surfaces*. In: *Journal of Electroanalytical Chemistry* 607.1-2 (2007), pp. 83–89. ISSN: 15726657. DOI: 10.1016/j.jelechem.2006.11.008.

[25] Haiwei Du et al. *Electric double-layer transistors: a review of recent progress*. In: *Journal of Materials Science* 50.17 (2015), pp. 5641–5673. ISSN: 0022-2461. DOI: 10.1007/s10853-015-9121-y.

[26] Carl H. Hamann and Wolf Vielstich. *Elektrochemie*. 4., vollst. überarb. und aktualisierte Aufl. Weinheim: Wiley-VCH, 2005. ISBN: 978-3-527-31068-5.

[27] Rolando Guidelli et al. *Defining the transfer coefficient in electrochemistry: An assessment (IUPAC Technical Report)*. In: *Pure and Applied Chemistry* 86.2 (2014), pp. 245–258. ISSN: 0033-4545. DOI: 10.1515/pac-2014-5026.

[28] A. Damjanovic, A. Dey, and J.O'M. Bockris. *Kinetics of oxygen evolution and dissolution on platinum electrodes*. In: *Electrochimica Acta* 11.7 (1966), pp. 791–814. ISSN: 00134686. DOI: 10.1016/0013-4686(66)87056-1.

[29] Ya-Hui Fang and Zhi-Pan Liu. *Tafel Kinetics of Electrocatalytic Reactions: From Experiment to First-Principles*. In: *ACS Catalysis* 4.12 (2014), pp. 4364–4376. ISSN: 2155-5435. DOI: 10.1021/cs501312v.

[30] D. Depla and S. Mahieu, eds. *Reactive sputter deposition*. Vol. 109. Springer series in Materials Science. Berlin: Springer, 2008. ISBN: 978-3-540-76662-9.

[31] Brian N. Chapman. *Glow discharge processes: Sputtering and plasma etching / Brian Chapman*. New York and Chichester: Wiley, 1980. ISBN: 0-471-07828-X.

[32] Hem Raj Verma. *Atomic and nuclear analytical methods: XRF, Mössbauer, XPS, NAA and Ion-Beam spectroscopic techniques*. Berlin, Heidelberg: Springer Berlin Heidelberg and Springer e-books, 2007. ISBN: 978-3-540-30279-7.

[33] S. Hofmann, ed. *Auger- and X-ray photoelectron spectroscopy in materials science: A user-oriented guide*. Vol. 49. Springer series in surface sciences. Heidelberg and London: Springer, 2013. ISBN: 978-3-642-27380-3.

[34] Gernot Friedbacher and H. Bubert. *Surface and thin film analysis: A compendium of principles, instrumentation, and applications / edited by Gernot Friedbacher and Henning Bubert*. 2nd completely rev. and enlarged ed. Weinheim: Wiley-VCH, 2011. ISBN: 978-3-527-32047-9.

[35] Michel J. Bertrand. *Handbook of Instrumental Techniques for Analytical Chemistry Edited by Frank A. Settle. Prentice Hall: Upper Saddle River. 1997. xxi + 995 pp. ISBN 0-13-177338-0*. In: *Journal of the American Chemical Society* 120.26 (1998), p. 6633. ISSN: 0002-7863. DOI: `10.1021/ja975671k`.

[36] Howell G. M. Edwards. *Modern Raman spectroscopy—a practical approach.Ewen Smith and Geoffrey Dent. John Wiley and Sons Ltd, Chichester, 2005. Pp. 210. ISBN 0 471 49668 5 (cloth, hb); 0 471 49794 0 (pbk)*. In: *Journal of Raman Spectroscopy* 36.8 (2005), p. 835. ISSN: 03770486. DOI: `10.1002/jrs.1320`.

[37] C. V. RAMAN and K. S. KRISHNAN. *A New Type of Secondary Radiation*. In: *Philosophical Transactions of the Royal Society A: Mathematical, Physical and Engineering Sciences* 121.3048 (1928), pp. 501–502. ISSN: 1476-4687. DOI: `10.1038/121501c0`.

[38] Douglas A. Skoog et al. *Principles of instrumental analysis*. 6th ed. / Douglas A. Skoog, F. James Holler, Stanley R. Crouch. Pacific Grove, Calif.: Brooks/Cole and London : Thomson Learning [distributor], 2007. ISBN: 9780495125709.

[39] Gurvinder Singh Bumbrah and Rakesh Mohan Sharma. *Raman spectroscopy – Basic principle, instrumentation and selected applications for the characterization of drugs of abuse*. In: *Egyptian Journal of Forensic Sciences* 6.3 (2016), pp. 209–215. ISSN: 2090536X. DOI: `10.1016/j.ejfs.2015.06.001`.

[40] Thomas Dieing, Olaf Hollricher, and Jan Toporski. *Confocal Raman Microscopy*. Vol. 158. Berlin, Heidelberg: Springer Berlin Heidelberg, 2011. ISBN: 978-3-642-12521-8. DOI: `10.1007/978-3-642-12522-5`.

[41] M. Fleischmann, P. J. Hendra, and A. J. McQuillan. *Raman spectra of pyridine adsorbed at a silver electrode*. In: *Chemical Physics Letters* 26.2 (1974), pp. 163–166. ISSN: 00092614. DOI: `10.1016/0009-2614(74)85388-1`.

[42] P. C. White. *In situ Surface Enhanced Resonance Raman Scattering (SERRS) spectroscopy of biro inks – long term stability of colloid treated samples*. In: *Science & Justice* 43.3 (2003), pp. 149–152. ISSN: 13550306. DOI: `10.1016/S1355-0306(03)71762-6`.

[43] Miguel A. Bañares. *Preface*. In: *Catalysis Today* 126.1-2 (2007), pp. 1–2. ISSN: 09205861. DOI: `10.1016/j.cattod.2007.07.004`.

[44] R. W. Cairns and Emil Ott. *X-Ray Studies of the System Nickel—Oxygen—Water. I. Nickelous Oxide and Hydroxide 1*. In: *Journal of the American Chemical Society* 55.2 (1933), pp. 527–533. ISSN: 0002-7863. DOI: `10.1021/ja01329a013`.

[45] Nobuo Tsuda et al. *Electronic Conduction in Oxides*. Second, rev. and enlarged edition. Vol. 94. Springer Series in Solid-State Sciences. Berlin, Heidelberg: Springer Berlin Heidelberg, 2000. ISBN: 978-3-662-04011-9.

[46] John R. Rumble, ed. *CRC handbook of chemistry and physics: A ready-reference book of chemical and physical data*. 2017-2018, 98th edition. Boca Raton, London, and New York: CRC Press, Taylor et Francis Group, 2017. ISBN: 978-1-4987-8454-2.

[47] Toshiaki Enoki and Ikuji Tsujikawa. *Magnetic Behaviours of a Random Magnet, Ni p Mg (1- p) (OH 2)*. In: *Journal of the Physical Society of Japan* 39.2 (1975), pp. 317–323. ISSN: 0031-9015. DOI: `10.1143/JPSJ.39.317`.

[48] P. Jeevanandam, Yu. Koltypin, and A. Gedanken. *Synthesis of Nanosized Nickel Hydroxide by a Sonochemical Method*. In: *Nano Letters* 1.5 (2001), pp. 263–266. ISSN: 1530-6984. DOI: `10.1021/nl010003p`.

[49] P. Oliva et al. *Review of the structure and the electrochemistry of nickel hydroxides and oxy-hydroxides*. In: *Journal of Power Sources* 8.2 (1982), pp. 229–255. ISSN: 03787753. DOI: 10.1016/0378-7753(82)80057-8.

[50] A. Livingstone. *On the New Mineral Theophrastite, a Nickel Hydroxide, from Unst, Shetland, Scotland*. In: *Mineralogical Magazine* 46.338 (1982), pp. 1–5. ISSN: 0026-461X. DOI: 10.1180/minmag.1982.046.338.01.

[51] J. L. Bantignies et al. *New Insight into the Vibrational Behavior of Nickel Hydroxide and Oxyhydroxide Using Inelastic Neutron Scattering, Far/Mid-Infrared and Raman Spectroscopies*. In: *The Journal of Physical Chemistry C* 112.6 (2008), pp. 2193–2201. ISSN: 1932-7447. DOI: 10.1021/jp075819e.

[52] R. S. McEwen. *Crystallographic studies on nickel hydroxide and the higher nickel oxides*. In: *The Journal of Physical Chemistry* 75.12 (1971), pp. 1782–1789. ISSN: 0022-3654. DOI: 10.1021/j100681a004.

[53] Richard L. Doyle et al. *Redox and electrochemical water splitting catalytic properties of hydrated metal oxide modified electrodes*. In: *Physical Chemistry Chemical Physics* 15.33 (2013), pp. 13737–13783. ISSN: 14639076. DOI: 10.1039/C3CP51213D.

[54] H. Bode, K. Dehmelt, and J. Witte. *Zur kenntnis der nickelhydroxidelektrode—I.Über das nickel (II)-hydroxidhydrat*. In: *Electrochimica Acta* 11.8 (1966), 1079–IN1. ISSN: 00134686. DOI: 10.1016/0013-4686(66)80045-2.

[55] David S. Hall et al. *Applications of in Situ Raman Spectroscopy for Identifying Nickel Hydroxide Materials and Surface Layers during Chemical Aging*. In: *ACS Applied Materials & Interfaces* 6.5 (2014), pp. 3141–3149. ISSN: 1944-8244. DOI: 10.1021/am405419k.

[56] Kim Kinoshita. *Electrochemical oxygen technology*. New York and Chichester: Wiley, 1992. ISBN: 978-0-471-57043-1.

[57] M. Vuković. *Voltammetry and anodic stability of a hydrous oxide film on a nickel electrode in alkaline solution*. In: *Journal of Applied Electrochemistry* 24.9 (1994), pp. 878–882. ISSN: 1572-8838. DOI: 10.1007/BF00348775.

[58] Sengeni Anantharaj et al. *Recent Trends and Perspectives in Electrochemical Water Splitting with an Emphasis on Sulfide, Selenide, and Phosphide Catalysts of Fe, Co, and Ni: A Review*. In: *ACS Catalysis* 6.12 (2016), pp. 8069–8097. ISSN: 2155-5435. DOI: 10.1021/acscatal.6b02479.

[59] Varun Vij et al. *Nickel-Based Electrocatalysts for Energy-Related Applications: Oxygen Reduction, Oxygen Evolution, and Hydrogen Evolution Reactions*. In: *ACS Catalysis* 7.10 (2017), pp. 7196–7225. ISSN: 2155-5435. DOI: 10.1021/acscatal.7b01800.

[60] Lucas-Alexandre Stern and Xile Hu. *Enhanced oxygen evolution activity by NiO x and Ni(OH) 2 nanoparticles*. In: *Faraday Discuss* 176 (2014), pp. 363–379. ISSN: 1359-6640. DOI: 10.1039/c4fd00120f.

[61] Reza B. Moghaddam et al. *Easily prepared, high activity Ir–Ni oxide catalysts for water oxidation*. In: *Electrochemistry Communications* 60 (2015), pp. 109–112. ISSN: 13882481. DOI: 10.1016/j.elecom.2015.08.015.

[62] Xiaofan Zhang et al. *RGO modified Ni doped FeOOH for enhanced electrochemical and photoelectrochemical water oxidation*. In: *Applied Surface Science* 436 (2018), pp. 974–980. ISSN: 01694332. DOI: 10.1016/j.apsusc.2017.12.078.

[63] Nancy Li et al. *Influence of iron doping on tetravalent nickel content in catalytic oxygen evolving films*. In: *Proceedings of the National Academy of Sciences* 114.7 (2017), pp. 1486–1491. ISSN: 0027-8424. DOI: 10.1073/pnas.1620787114.

[64] Zhanwu Lei et al. *Fabrication of Nanoporous Nickel–Iron Hydroxylphosphate Composite as Bifunctional and Reversible Catalyst for Highly Efficient Intermittent Water Splitting*. In: *ACS Applied Materials & Interfaces* 9.41 (2017), pp. 35837–35846. ISSN: 1944-8244. DOI: 10.1021/acsami.7b10385.

[65] David S. Hall et al. *Raman and infrared spectroscopy of α and β phases of thin nickel hydroxide films electrochemically formed on nickel*. In: *The journal of physical chemistry. A* 116.25 (2012), pp. 6771–6784. DOI: 10.1021/jp303546r.

[66] Fabien Pascale et al. *Vibrational spectrum of brucite, Mg(OH)2: a periodic ab initio quantum mechanical calculation including OH anharmonicity*. In: *Chemical Physics Letters* 396.4-6 (2004), pp. 308–315. ISSN: 00092614. DOI: 10.1016/j.cplett.2004.08.047.

[67] N. Mironova-Ulmane, A. Kuzmin, and M. Grube. *Raman and infrared spectromicroscopy of manganese oxides*. In: *Journal of Alloys and Compounds* 480.1 (2009), pp. 97–99. ISSN: 09258388. DOI: 10.1016/j.jallcom.2008.10.056.

[68] M. C. Bernard et al. *Structural defects and electrochemical reactivity of β-Ni(OH)2*. In: *Journal of Power Sources* 63.2 (1996), pp. 247–254. ISSN: 03787753. DOI: 10.1016/S0378-7753(96)02482-2.

[69] A. Audemer. *Electrochemical and Raman Studies of Beta-Type Nickel Hydroxides Ni[sub 1−x]Co[sub x](OH)[sub 2] Electrode Materials*. In: *Journal of The Electrochemical Society* 144.8 (1997), p. 2614. ISSN: 0013-4651. DOI: 10.1149/1.1837873.

[70] C. Johnston and P. R. Graves. *In situ Raman Spectroscopy Study of the Nickel Oxyhydroxide Electrode (NOE) System*. In: *Applied Spectroscopy* 44.1 (1990), pp. 105–115. ISSN: 0003-7028. DOI: 10.1366/0003702904085769.

[71] Chitra Murli et al. *High-pressure behavior of β-Ni (OH)2—A Raman scattering study*. In: *Physica B: Condensed Matter* 307.1-4 (2001), pp. 111–116. ISSN: 09214526. DOI: 10.1016/S0921-4526(01)00646-9.

[72] Oscar Diaz-Morales, David Ferrus-Suspedra, and Marc T. M. Koper. *The importance of nickel oxyhydroxide deprotonation on its activity towards electrochemical water oxidation*. In: *Chemical science* 7.4 (2016), pp. 2639–2645. ISSN: 2041-6520. DOI: 10.1039/C5SC04486C.

[73] Boon Siang Yeo and Alexis T. Bell. *In Situ Raman Study of Nickel Oxide and Gold-Supported Nickel Oxide Catalysts for the Electrochemical Evolution of Oxygen*. In: *The Journal of Physical Chemistry C* 116.15 (2012), pp. 8394–8400. ISSN: 1932-7447. DOI: 10.1021/jp3007415.

[74] Mohammad Mahdi Najafpour and Suleyman I. Allakhverdiev. *Manganese compounds as water oxidizing catalysts for hydrogen production via water splitting: From manganese complexes to nano-sized manganese oxides*. In: *International Journal of Hydrogen Energy* 37.10 (2012), pp. 8753–8764. ISSN: 03603199. DOI: 10.1016/j.ijhydene.2012.02.075.

[75] Athina Zouni et al. *Crystal structure of photosystem II from Synechococcus elongatus at 3.8 Å resolution*. In: *Nature* 409 (2001), 739 EP -. DOI: 10.1038/35055589. URL: http://dx.doi.org/10.1038/35055589.

[76] Thomas Kuntzleman and Charles F. Yocum. *Reduction-induced inhibition and Mn(II) release from the photosystem II oxygen-evolving complex by hydroquinone or NH2OH are consistent with a Mn(III)/Mn(III)/Mn(IV)/Mn(IV) oxidation state for the dark-adapted enzyme*. In: *Biochemistry* 44.6 (2005), pp. 2129–2142. ISSN: 0006-2960. DOI: 10.1021/bi048460i.

[77] Yasufumi Umena et al. *Crystal structure of oxygen-evolving photosystem II at a resolution of 1.9 Å*. In: *Philosophical Transactions of the Royal Society A: Mathematical, Physical and Engineering Sciences* 473.7345 (2011), pp. 55–60. ISSN: 1476-4687. DOI: 10.1038/nature09913.

[78] Masayuki Yagi and Masao Kaneko. *Molecular Catalysts for Water Oxidation*. In: *Chemical Reviews* 101.1 (2001), pp. 21–36. ISSN: 0009-2665. DOI: 10.1021/cr980108l.

[79] Arno H. Reidies. *Manganese Compounds*. In: *Ullmann's Encyclopedia of Industrial Chemistry*. Vol. 309. Weinheim, Germany: Wiley-VCH Verlag GmbH & Co. KGaA, 2000, p. 1. ISBN: 3527306730. DOI: 10.1002/14356007.a16{\textunderscore}123.

[80] Georg Brauer. *Handbuch der präparativen anorganischen Chemie*. 3. umgearb. Aufl. Stuttgart: Ferdinand Enke, 1975. ISBN: 3-432-87823-0.

[81] S. Geller. *Structure of α-Mn 2 O 3 , (Mn 0.983 Fe 0.017) 2 O 3 and (Mn 0.37 Fe 0.63) 2 O 3 and relation to magnetic ordering*. In: *Acta Crystallographica Section B Structural Crystallography and Crystal Chemistry* 27.4 (1971), pp. 821–828. ISSN: 0567-7408. DOI: 10.1107/S0567740871002966.

[82] N. N. Greenwood and A. Earnshaw. *Chemistry of the elements*. Oxford: Pergamon, 1984. ISBN: 0-08-022057-6.

[83] C.M Julien, M. Massot, and C. Poinsignon. *Lattice vibrations of manganese oxides*. In: *Spectrochimica Acta Part A: Molecular and Biomolecular Spectroscopy* 60.3 (2004), pp. 689–700. ISSN: 13861425. DOI: 10.1016/S1386-1425(03)00279-8.

[84] *Ullmann's Encyclopedia of Industrial Chemistry*. Weinheim, Germany: Wiley-VCH Verlag GmbH & Co. KGaA, 2000. ISBN: 3527306730.

[85] Kiyoshi Terayama and Masao Ikeda. *Study on Thermal Decomposition of MnO2 and Mn2O3 by Thermal Analysis*. In: *Transactions of the Japan Institute of Metals* 24.11 (1983), pp. 754–758. ISSN: 0021-4434. DOI: 10.2320/matertrans1960.24.754.

[86] Florina Buciuman et al. *Vibrational spectroscopy of bulk and supported manganese oxides*. In: *Physical Chemistry Chemical Physics* 1.1 (1999), pp. 185–190. ISSN: 14639076. DOI: 10.1039/A807821A.

[87] Tao Gao, Helmer Fjellvåg, and Poul Norby. *A comparison study on Raman scattering properties of alpha- and beta-MnO2*. In: *Analytica chimica acta* 648.2 (2009), pp. 235–239. DOI: 10.1016/j.aca.2009.06.059.

[88] Rakesh Radhakrishnan and S.Ted Oyama. *Ozone Decomposition over Manganese Oxide Supported on ZrO2 and TiO2: A Kinetic Study Using in Situ Laser Raman Spectroscopy*. In: *Journal of Catalysis* 199.2 (2001), pp. 282–290. ISSN: 00219517. DOI: 10.1006/jcat.2001.3167.

[89] Brian R. Strohmeier and David M. Hercules. *Surface spectroscopic characterization of manganese/aluminum oxide catalysts*. In: *The Journal of Physical Chemistry* 88.21 (1984), pp. 4922–4929. ISSN: 0022-3654. DOI: 10.1021/j150665a026.

[90] Yi-Fan Han et al. *Observation of the Reversible Phase-Transformation of α-Mn 2 O 3 Nanocrystals during the Catalytic Combustion of Methane by in Situ Raman Spectroscopy*. In: *The Journal of Physical Chemistry C* 111.7 (2007), pp. 2830–2833. ISSN: 1932-7447. DOI: 10.1021/jp0686691.

[91] Shuang Cheng et al. *Phase evolution of an alpha MnO 2 -based electrode for pseudo-capacitors probed by in operando Raman spectroscopy*. In: *Nano Energy* 9 (2014), pp. 161–167. ISSN: 22112855. DOI: 10.1016/j.nanoen.2014.07.008.

[92] Bouzid Messaoudi et al. *Anodic behaviour of manganese in alkaline medium*. In: *Electrochimica Acta* 46.16 (2001), pp. 2487–2498. ISSN: 00134686. DOI: 10.1016/S0013-4686(01)00449-2.

[93] Marie-Claude Bernard. *Electrochromic Reactions in Manganese Oxides*. In: *Journal of The Electrochemical Society* 140.11 (1993), p. 3065. ISSN: 0013-4651. DOI: 10.1149/1.2220986.

[94] Hongyu An et al. *An Operando-Raman study on oxygen evolution of manganese oxides: Roles of phase composition and amorphization*. In: *Journal of Catalysis* 367 (2018), pp. 53–61. ISSN: 00219517. DOI: 10.1016/j.jcat.2018.08.007.

[95] David Gosztola and Michael J. Weaver. *Electroinduced structural changes in manganese dioxide + manganese hydroxide films as characterized by real-time surface-enhanced Raman spectroscopy*. In: *Journal of Electroanalytical Chemistry and Interfacial Electrochemistry* 271.1-2 (1989), pp. 141–154. ISSN: 00220728. DOI: 10.1016/0022-0728(89)80070-1.

[96] L. D. Burke and P. F. Nugent. *The electrochemistry of gold: I the redox behaviour of the metal in aqueous media*. In: *Gold Bulletin*

30.2 (1997), pp. 43–53. ISSN: 0017-1557. DOI: 10.1007/BF03214756.

[97] Perrin. Ed Walker and William H. Ed Tarn. *CRC handbook of metal etchants*. 1991. ISBN: 0-8493-3623-6.

[98] Y. M. Lu et al. *Properties of nickel oxide thin films deposited by RF reactive magnetron sputtering*. In: *Thin Solid Films* 420-421 (2002), pp. 54–61. ISSN: 00406090. DOI: 10.1016/S0040-6090(02)00654-5.

[99] Jan Toporski, Thomas Dieing, and Olaf Hollricher. *Confocal Raman microscopy*. Second edition. Vol. Volume 66. Springer series in surface sciences, 0931-5195. Cham, Switzerland: Springer, 2018. ISBN: 978-3-319-75378-2. URL: http://link.springer.com/%20BLDSS.

[100] Zhixun Luo and Yan Fang. *Investigation of the mechanism of influence of colloidal gold/silver substrates in nonaqueous liquids on the surface enhanced Raman spectroscopy (SERS) of fullerenes C60 (C70)*. In: *Journal of colloid and interface science* 301.1 (2006), pp. 184–192. ISSN: 0021-9797. DOI: 10.1016/j.jcis.2006.04.077.

[101] Silvia P. Centeno et al. *Selection rules of the charge transfer mechanism of surface-enhanced Raman scattering: The effect of the adsorption on the relative intensities of pyrimidine bonded to silver nanoclusters*. In: *The Journal of Physical Chemistry B* 110.30 (2006), pp. 14916–14922. ISSN: 1520-6106. DOI: 10.1021/jp0621373.

[102] Gloria M. Herrera, Amira C. Padilla, and Samuel P. Hernandez-Rivera. *Surface Enhanced Raman Scattering (SERS) Studies of Gold and Silver Nanoparticles Prepared by Laser Ablation*. In: *Nanomaterials (Basel, Switzerland)* 3.1 (2013), pp. 158–172. ISSN: 2079-4991. DOI: 10.3390/nano3010158.

[103] Noémie Elgrishi et al. *A Practical Beginner's Guide to Cyclic Voltammetry*. In: *Journal of Chemical Education* 95.2 (2018), pp. 197–206. ISSN: 0021-9584. DOI: 10.1021/acs.jchemed.7b00361.

[104] Anandhakumar Sukeri, Lucas Patricio Hernández Saravia, and Mauro Bertotti. *A facile electrochemical approach to fabricate a nanoporous gold film electrode and its electrocatalytic activity towards dissolved oxygen reduction*. In: *Physical Chemistry Chemical Physics* 17.43 (2015), pp. 28510–28514. ISSN: 14639076. DOI: 10.1039/c5cp05220c.

[105] Falong Jia et al. *Fabrication of Nanoporous Gold Film Electrodes with Ultrahigh Surface Area and Electrochemical Activity*. In: *Chemistry of Materials* 19.15 (2007), pp. 3648–3653. ISSN: 0897-4756. DOI: 10.1021/cm070425l.

[106] Yih Horng Tan et al. *Surface area and pore size characteristics of nanoporous gold subjected to thermal, mechanical, or surface modification studied using gas adsorption isotherms, cyclic voltammetry, thermogravimetric analysis, and scanning electron microscopy*. In: *J. Mater. Chem.* 22.14 (2012), pp. 6733–6745. ISSN: 0959-9428. DOI: 10.1039/c2jm16633j.

[107] S. Trasatti and O. A. Petrii. *Real surface area measurements in electrochemistry*. In: *Journal of Electroanalytical Chemistry* 327.1-2 (1992), pp. 353–376. ISSN: 15726657. DOI: 10.1016/0022-0728(92)80162-W.

[108] John F. Moulder and Jill Chastain. *Handbook of x-ray photoelectron spectroscopy: A reference book of standard spectra for identification and interpretation of XPS data*. Eden Prairie Minnesota: Physical Electronics, 1995. ISBN: 0-9648124-1-X.

[109] Chavis Srichan et al. *Highly-Sensitive Surface-Enhanced Raman Spectroscopy (SERS)-based Chemical Sensor using 3D Graphene Foam Decorated with Silver Nanoparticles as SERS substrate*. In: *Scientific reports* 6 (2016), p. 23733. DOI: 10.1038/srep23733.

[110] Wolfgang Haiss et al. *Determination of size and concentration of gold nanoparticles from UV-vis spectra*. In: *Analytical chemistry* 79.11 (2007), pp. 4215–4221. ISSN: 0003-2700. DOI: 10.1021/ac0702084.

[111] Ngangbam Bedamani Singh and Utpal Sarkar. *Geometry, chemical reactivity and Raman spectra of gold clusters*. In: *Cogent Chemistry* 1.1 (2015), p. 81. DOI: `10.1080/23312009.2015.1076713`.

[112] Furong Tian et al. *Surface enhanced Raman scattering with gold nanoparticles: effect of particle shape*. In: *Anal. Methods* 6.22 (2014), pp. 9116–9123. ISSN: 1759-9660. DOI: `10.1039/c4ay02112f`.

[113] Vincenzo Amendola and Moreno Meneghetti. *Size Evaluation of Gold Nanoparticles by UV—vis Spectroscopy*. In: *The Journal of Physical Chemistry C* 113.11 (2009), pp. 4277–4285. ISSN: 1932-7447. DOI: `10.1021/jp8082425`.

[114] Z. Q. Tian, B. Ren, and B. W. Mao. *Extending Surface Raman Spectroscopy to Transition Metal Surfaces for Practical Applications. 1. Vibrational Properties of Thiocyanate and Carbon Monoxide Adsorbed on Electrochemically Activated Platinum Surfaces*. In: *The Journal of Physical Chemistry B* 101.8 (1997), pp. 1338–1346. ISSN: 1520-6106. DOI: `10.1021/jp962049q`.

[115] Oscar Diaz-Morales et al. *Electrochemical water splitting by gold: evidence for an oxide decomposition mechanism*. In: *Chemical science* 4.6 (2013), p. 2334. ISSN: 2041-6520. DOI: `10.1039/c3sc50301a`.

[116] C. Pettenkofer, I. Pockrand, and A. Otto. *Surface enhanced Raman spectra of oxygen adsorbed on silver*. In: *Surface Science* 135.1-3 (1983), pp. 52–64. ISSN: 00396028. DOI: `10.1016/0039-6028(83)90209-1`.

[117] Zuojun Wei et al. *Graphene-supported Pd catalyst for highly selective hydrogenation of resorcinol to 1, 3-cyclohexanedione through giant π-conjugate interactions*. In: *Scientific reports* 5 (2015), p. 15664. DOI: `10.1038/srep15664`.

[118] Boon Siang Yeo et al. *Identification of hydroperoxy species as reaction intermediates in the electrochemical evolution of oxygen on gold*. In: *Chemphyschem : a European journal of chemical physics and physical chemistry* 11.9 (2010), pp. 1854–1857. DOI: `10.1002/cphc.201000294`.

[119] Thomas A. Baker et al. *Nature of Oxidation of the Au(111) Surface: Experimental and Theoretical Investigation*. In: *The Journal of Physical Chemistry C* 113.38 (2009), pp. 16561–16564. ISSN: 1932-7447. DOI: `10.1021/jp9052192`.

[120] N. P. Finkelstein and R. D. Hancock. *A new approach to the chemistry of gold*. In: *Gold Bulletin* 7.3 (1974), pp. 72–77. ISSN: 0017-1557. DOI: `10.1007/BF03215041`.

[121] Johann Desilvestro and Michael J. Weaver. *Surface structural changes during oxidation of gold electrodes in aqueous media as detected using surface-enhanced Raman spectroscopy*. In: *Journal of Electroanalytical Chemistry and Interfacial Electrochemistry* 209.2 (1986), pp. 377–386. ISSN: 00220728. DOI: `10.1016/0022-0728(86)80562-9`.

[122] St Uhlenbrock et al. *The influence of defects on the Ni 2p and O 1s XPS of NiO*. In: *Journal of Physics: Condensed Matter* 4.40 (1992), pp. 7973–7978. ISSN: 0953-8984. DOI: `10.1088/0953-8984/4/40/009`.

[123] K. S. Kim and Nicholas Winograd. *X-ray photoelectron spectroscopic studies of nickel-oxygen surfaces using oxygen and argon ion-bombardment*. In: *Surface Science* 43.2 (1974), pp. 625–643. ISSN: 00396028. DOI: `10.1016/0039-6028(74)90281-7`.

[124] Sven Tengeler et al. *The Impact of Different Si Surface Terminations in the (001) n-Si/NiOx Heterojunction on the Oxygen Evolution Reaction (OER) by XPS and Electrochemical Methods*. In: *Journal of The Electrochemical Society* 165.4 (2018), H3122–H3130. ISSN: 0013-4651. DOI: `10.1149/2.0151804jes`.

[125] Agustin R. Gonzalez-Elipe et al. *Use of factor analysis and XPS to study defective nickel oxide*. In: *The Journal of Physical Chemistry* 96.7 (1992), pp. 3080–3086. ISSN: 0022-3654. DOI: `10.1021/j100186a056`.

[126] Fan Hai-Bo et al. *Investigation of Oxygen Vacancy and Interstitial Oxygen Defects in ZnO Films by Photoluminescence and X-Ray Photoelectron Spectroscopy*. In: *Chinese Physics Letters* 24.7 (2007), pp. 2108–2111. ISSN:

0256-307X. DOI: 10.1088/0256-307X/24/7/089.

[127] Jean-Charles Dupin et al. *Systematic XPS studies of metal oxides, hydroxides and peroxides*. In: *Physical Chemistry Chemical Physics* 2.6 (2000), pp. 1319–1324. ISSN: 14639076. DOI: 10.1039/A908800H.

[128] Andrew P. Grosvenor et al. *New interpretations of XPS spectra of nickel metal and oxides*. In: *Surface Science* 600.9 (2006), pp. 1771–1779. ISSN: 00396028. DOI: 10.1016/j.susc.2006.01.041.

[129] S. Kac iulis et al. *Influence of surface oxygen on chemoresistance of tin oxide film*. In: *Journal of Vacuum Science & Technology A: Vacuum, Surfaces, and Films* 14.6 (1996), pp. 3164–3168. ISSN: 0734-2101. DOI: 10.1116/1.580207.

[130] Ksenia Fominykh et al. *Ultrasmall Dispersible Crystalline Nickel Oxide Nanoparticles as High-Performance Catalysts for Electrochemical Water Splitting*. In: *Advanced Functional Materials* 24.21 (2014), pp. 3123–3129. ISSN: 1616301X. DOI: 10.1002/adfm.201303600.

[131] Venkat Srinivasan and John W. Weidner. *Studies on the Capacitance of Nickel Oxide Films: Effect of Heating Temperature and Electrolyte Concentration*. In: *Journal of The Electrochemical Society* 147.3 (2000), p. 880. ISSN: 0013-4651. DOI: 10.1149/1.1393286.

[132] T. S. Chou, M. L. Perlman, and R. E. Watson. *Electronegativity and electron binding in gold alloys*. In: *Physical Review B* 14.8 (1976), pp. 3248–3250. ISSN: 0556-2805. DOI: 10.1103/PhysRevB.14.3248.

[133] Dennis A. Corrigan. *The Catalysis of the Oxygen Evolution Reaction by Iron Impurities in Thin Film Nickel Oxide Electrodes*. In: *Journal of The Electrochemical Society* 134.2 (1987), p. 377. ISSN: 0013-4651. DOI: 10.1149/1.2100463.

[134] Shannon Klaus et al. *Effects of Fe Electrolyte Impurities on Ni(OH) 2 /NiOOH Structure and Oxygen Evolution Activity*. In: *The Journal of Physical Chemistry C* 119.13 (2015), pp. 7243–7254. ISSN: 1932-7447. DOI: 10.1021/acs.jpcc.5b00105.

[135] Kyung-Wan Nam, Won-Sub Yoon, and Kwang-Bum Kim. *X-ray absorption spectroscopy studies of nickel oxide thin film electrodes for supercapacitors*. In: *Electrochimica Acta* 47.19 (2002), pp. 3201–3209. ISSN: 00134686. DOI: 10.1016/S0013-4686(02)00240-2.

[136] S. I. Cordoba-Torresi. *Electrochromic Behavior of Nickel Oxide Electrodes*. In: *Journal of The Electrochemical Society* 138.6 (1991), p. 1554. ISSN: 0013-4651. DOI: 10.1149/1.2085831.

[137] Nina Mironova-Ulmane et al. *Polarisation dependent Raman study of single-crystal nickel oxide*. In: *Open Physics* 9.4 (2011), p. 1333. DOI: 10.2478/s11534-010-0130-9.

[138] N. Mironova-Ulmane et al. *Raman scattering in nanosized nickel oxide NiO*. In: *Journal of Physics: Conference Series* 93 (2007), p. 012039. ISSN: 1742-6588. DOI: 10.1088/1742-6596/93/1/012039.

[139] Meng-Lin Lu et al. *Large enhancement of photocurrent gain based on the composite of a single n-type SnO2 nanowire and p-type NiO nanoparticles*. In: *Optics express* 19.17 (2011), pp. 16266–16272. DOI: 10.1364/OE.19.016266.

[140] Kazuo Nakamoto. *Infrared and Raman spectra of inorganic and coordination compounds*. 6th ed. Hoboken, N.J.: Wiley and [Oxford : Wiley-Blackwell, 2009. ISBN: 9780471743392.

[141] H. M. Gager, L. Lewis, and M. J. Ware. *Metal–metal stretching frequencies in Raman spectra*. In: *Chem. Commun. (London)* 0.17 (1966), pp. 616–617. ISSN: 0009-241X. DOI: 10.1039/C19660000616.

[142] Girish S. Gund et al. *Low-cost flexible supercapacitors with high-energy density based on nanostructured MnO2 and Fe2O3 thin films directly fabricated onto stainless steel*. In: *Scientific reports* 5 (2015), p. 12454. DOI: 10.1038/srep12454.

[143] Raul D. Rodriguez et al. *Surface- and tip-enhanced Raman spectroscopy reveals spin-waves in iron oxide nanoparticles*. In: *Nanoscale* 7.21 (2015), pp. 9545–9551. DOI: 10.1039/C5NR01277E.

[144] I. Burmistrov et al. *Performance Optimization of Cermet SOFC Anodes: An Evaluation of Nanostructured NiO*. In: *ECS Transactions* 68.1 (2015), pp. 1265–1274. ISSN: 1938-6737. DOI: 10.1149/06801.1265ecst.

[145] S. Vivek, P. Arunkumar, and K. Suresh Babu. *In situ generated nickel on cerium oxide nanoparticle for efficient catalytic reduction of 4-nitrophenol*. In: *RSC Advances* 6.51 (2016), pp. 45947–45956. DOI: 10.1039/C6RA04120E.

[146] Robert Kostecki. *Electrochemical and In Situ Raman Spectroscopic Characterization of Nickel Hydroxide Electrodes*. In: *Journal of The Electrochemical Society* 144.2 (1997), p. 485. ISSN: 0013-4651. DOI: 10.1149/1.1837437.

[147] H. B. Li et al. *Amorphous nickel hydroxide nanospheres with ultrahigh capacitance and energy density as electrochemical pseudocapacitor materials*. In: *Nature communications* 4 (2013), p. 1894. DOI: 10.1038/ncomms2932.

[148] David S. Hall et al. *Nickel hydroxides and related materials: a review of their structures, synthesis and properties*. In: *Proceedings. Mathematical, physical, and engineering sciences* 471.2174 (2015), p. 20140792. ISSN: 1364-5021. DOI: 10.1098/rspa.2014.0792.

[149] Lyons, Michael EG and Brandon, Michael P. *The oxygen evolution reaction on passive oxide covered transition metal electrodes in aqueous alkaline solution. Part 1-Nickel*. In: *Int. J. Electrochem. Sci* 3.12 (2008), pp. 1386–1424.

[150] K. Juodkazis et al. *Nickel surface anodic oxidation and electrocatalysis of oxygen evolution*. In: *Journal of Solid State Electrochemistry* 12.11 (2008), pp. 1469–1479. ISSN: 1432-8488. DOI: 10.1007/s10008-007-0484-0.

[151] Eugene S. Ilton et al. *XPS determination of Mn oxidation states in Mn (hydr)oxides*. In: *Applied Surface Science* 366 (2016), pp. 475–485. ISSN: 01694332. DOI: 10.1016/j.apsusc.2015.12.159.

[152] Mark C. Biesinger et al. *Resolving surface chemical states in XPS analysis of first row transition metals, oxides and hydroxides: Cr, Mn, Fe, Co and Ni*. In: *Applied Surface Science* 257.7 (2011), pp. 2717–2730. ISSN: 01694332. DOI: 10.1016/j.apsusc.2010.10.051.

[153] Yelena Gorlin and Thomas F. Jaramillo. *A bifunctional nonprecious metal catalyst for oxygen reduction and water oxidation*. In: *Journal of the American Chemical Society* 132.39 (2010), pp. 13612–13614. DOI: 10.1021/ja104587v.

[154] V. Di Castro and G. Polzonetti. *XPS study of MnO oxidation*. In: *Journal of Electron Spectroscopy and Related Phenomena* 48.1 (1989), pp. 117–123. ISSN: 03682048. DOI: 10.1016/0368-2048(89)80009-X.

[155] Y. Matsumoto and E. Sato. *Electrocatalytic properties of transition metal oxides for oxygen evolution reaction*. In: *Materials Chemistry and Physics* 14.5 (1986), pp. 397–426. ISSN: 02540584. DOI: 10.1016/0254-0584(86)90045-3.

[156] Michael A. Stranick. *MnO 2 by XPS*. In: *Surface Science Spectra* 6.1 (1999), pp. 31–38. ISSN: 1055-5269. DOI: 10.1116/1.1247888.

[157] Michael A. Stranick. *Mn 2 O 3 by XPS*. In: *Surface Science Spectra* 6.1 (1999), pp. 39–46. ISSN: 1055-5269. DOI: 10.1116/1.1247889.

[158] M. P. Casaletto et al. *XPS study of supported gold catalysts: the role of Au0 and Au+δ species as active sites*. In: *Surface and Interface Analysis* 38.4 (2006), pp. 215–218. ISSN: 0142-2421. DOI: 10.1002/sia.2180.

[159] J. J. Pireaux et al. *Electron spectroscopic characterization of oxygen adsorption on gold surfaces*. In: *Surface Science* 141.1 (1984), pp. 221–232. ISSN: 00396028. DOI: 10.1016/0039-6028(84)90207-3.

[160] Zunxian Yang et al. *Facile Synthesis of Coaxial CNTs/MnOx-Carbon Hybrid Nanofibers and Their Greatly Enhanced Lithium Storage Performance*. In: *Scientific reports* 5 (2015), p. 17473. DOI: 10.1038/srep17473.

[161] Konstantin Iakoubovskii et al. *Mean free path of inelastic electron scattering in elemental solids and oxides using transmission electron microscopy: Atomic number dependent oscillatory behavior*. In: *Physical Review B* 77.10 (2008), p. 325. ISSN: 0556-2805. DOI: 10.1103/PhysRevB.77.104102.

[162] C. J. Powell and A. Jablonski. *NIST Electron Inelastic-Mean-Free-Path Database - Version 1.2*. Gaithersburg, MD: National Institute of Standards and Technology, 2010.

[163] Monika Fekete et al. *Highly active screen-printed electrocatalysts for water oxidation based on β-manganese oxide*. In: *Energy & Environmental Science* 6.7 (2013), p. 2222. ISSN: 1754-5692. DOI: 10.1039/C3EE40429C.

[164] Yelena Gorlin et al. *Understanding interactions between manganese oxide and gold that lead to enhanced activity for electrocatalytic water oxidation*. In: *Journal of the American Chemical Society* 136.13 (2014), pp. 4920–4926. ISSN: 0002-7863. DOI: 10.1021/ja407581w.

[165] Mohamed S. El-Deab et al. *Enhanced water electrolysis: Electrocatalytic generation of oxygen gas at manganese oxide nanorods modified electrodes*. In: *Electrochemistry Communications* 9.8 (2007), pp. 2082–2087. ISSN: 13882481. DOI: 10.1016/j.elecom.2007.06.011.

[166] Rasmus Frydendal et al. *Enhancing Activity for the Oxygen Evolution Reaction: The Beneficial Interaction of Gold with Manganese and Cobalt Oxides*. In: *ChemCatChem* 7.1 (2015), pp. 149–154. ISSN: 1867-3880. DOI: 10.1002/cctc.201402756.

[167] Alejandra Ramírez et al. *Evaluation of MnO x , Mn 2 O 3 , and Mn 3 O 4 Electrodeposited Films for the Oxygen Evolution Reaction of Water*. In: *The Journal of Physical Chemistry C* 118.26 (2014), pp. 14073–14081. ISSN: 1932-7447. DOI: 10.1021/jp500939d.

[168] Lufeng Yang et al. *Investigations into the origin of pseudocapacitive behavior of Mn 3 O 4 electrodes using in operando Raman spectroscopy*. In: *Journal of Materials Chemistry A* 3.14 (2015), pp. 7338–7344. ISSN: 2050-7488. DOI: 10.1039/C5TA00223K.

[169] C. Hu. *Ideal capacitive behavior of hydrous manganese oxide prepared by anodic deposition*. In: *Electrochemistry Communications* 4.2 (2002), pp. 105–109. ISSN: 13882481. DOI: 10.1016/S1388-2481(01)00285-5.

[170] Mathieu Toupin, Thierry Brousse, and Daniel Bélanger. *Charge Storage Mechanism of MnO 2 Electrode Used in Aqueous Electrochemical Capacitor*. In: *Chemistry of Materials* 16.16 (2004), pp. 3184–3190. ISSN: 0897-4756. DOI: 10.1021/cm049649j.

[171] Suh-Cem Pang, Marc A. Anderson, and Thomas W. Chapman. *Novel Electrode Materials for Thin-Film Ultracapacitors: Comparison of Electrochemical Properties of Sol-Gel-Derived and Electrodeposited Manganese Dioxide*. In: *Journal of The Electrochemical Society* 147.2 (2000), p. 444. ISSN: 0013-4651. DOI: 10.1149/1.1393216.

[172] Chan et al. *Electrochemical trapping of metastable Mn3+ ions for activation of MnO2 oxygen evolution catalysts*. In: *Proceedings of the National Academy of Sciences of the United States of America* 115.23 (2018), E5261–E5268. DOI: 10.1073/pnas.1722235115.

[173] C. Julien. *Raman spectra of birnessite manganese dioxides*. In: *Solid State Ionics* 159.3-4 (2003), pp. 345–356. ISSN: 01672738. DOI: 10.1016/S0167-2738(03)00035-3.

[174] Toshihiro Takashima, Kazuhito Hashimoto, and Ryuhei Nakamura. *Inhibition of charge disproportionation of MnO2 electrocatalysts for efficient water oxidation under neutral conditions*. In: *Journal of the American Chemical Society* 134.44 (2012), pp. 18153–18156. ISSN: 0002-7863. DOI: 10.1021/ja306499n.

[175] Lufeng Yang et al. *Investigation into the origin of high stability of δ-MnO 2 pseudo-capacitive electrode using operando Raman spectroscopy*. In: *Nano Energy* 30 (2016),

pp. 293–302. ISSN: 22112855. DOI: `10.1016/j.nanoen.2016.10.018`.

[176] Seihun. Chang, G. Blyholder, and Juan. Fernandez. *Iron-oxygen interactions in an argon matrix*. In: *Inorganic Chemistry* 20.9 (1981), pp. 2813–2817. ISSN: 0020-1669. DOI: `10.1021/ic50223a015`.

List of Figures

List of Tables